UNIVERSITY COLLEGE LONDON

DOCTORAL THESIS

Multi-electron ionisation in driven atoms and molecules

Author:
Hugh Lloyd PRICE

Supervisor:
Dr. Agapi EMMANOUILIDOU

A thesis submitted in fulfilment of the requirements
for the degree of Doctor of Philosophy

in the

Department of Physics and Astronomy
University College London

September 2014

Declaration of Authorship

I, Hugh Lloyd Price, confirm that the work presented in this thesis is my own. Where information has been derived from other sources, I confirm that this has been indicated in the thesis.

Signed: ____

Date: ____

Abstract

In this thesis we formulate sophisticated quasiclassical techniques to describe correlated electron dynamics in atoms and diatomic molecules that are either absorbing a single photon or are driven by strong infrared laser fields. The first part of this thesis concerns the multi-electron ionisation in atoms following single-photon absorption. For excess photon energies close to threshold, the Wannier threshold law predicts that the electrons escape in the most symmetric way. We describe the single-photon quadruple ionisation from the ground state of beryllium. Surprisingly, we find that close to threshold the four electrons escape on the apexes of a triangular pyramid, while Wannier threshold law predicts a regular tetrahedron. We explain this unexpected breakup pattern using non-linear analysis for the fixed points of the Coulomb four-body system. We then focus on time-resolving the attosecond collision sequences that underlie single-photon multi-electron ionisation. We formulate how to time resolve intra-atomic correlated electron dynamics during the escape of two electrons. Specifically, we show how to compute the "collision" time, using the inter-electronic angle as a function of the phase between the triggering and the streaking laser fields. We also demonstrate how this two-electron streak camera captures the different ionisation dynamics for different electron energy sharings. We then proceed to generalise the two electron streak camera to account for realistic experimental conditions. In the final part of this thesis, we address correlated electron dynamics during the breakup of diatomic molecules driven by intense infrared laser fields. We concentrate on the two pathways leading to the formation of highly excited neutral atoms. In particular, we show how for high ellipticites of the infrared laser field two-electron effects are "switched" off. Moreover, we find that the two dimensional momentum distribution of the escaping electron, in the formation of highly excited neutral atoms, carries the imprint of one-electron effects with increasing ellipticity of the infrared laser field.

Acknowledgements

I would like to thank my supervisor Dr. Agapi Emmanouilidou for her continual support, guidance and advice, without which this work would not have been possible. I would like to thank Dr. Constantinos Lazarou for his instructions on how to use the numerical packages Mathematica and Matlab. I would like to thank Dr. Andre Staudte from the National Research Council in Ottawa, Canada for the helpful discussions concerning part of this work. I would like to thank UCL's Research Computing Department for access to the computational resources of Legion running the equivalent of approximately 1000 CPU years needed for this PhD thesis. I acknowledge funding from EPSRC. I would like to thank my parents for their support during this PhD and throughout my education even though I still have a lot to learn.

Contents

List of Figures

List of Tables

Abbreviations

HHG	High-order harmonic generation
FROG	Frequency-resolved optical gating
CRAB	Complete reconstruction of attosecond bursts
IR	Infrared
Be	Beryllium
QI	Quadruple ionisation
Li	Lithium
He	Helium
FWHM	Full width at half maximum
DPI	Double photo-ionisation
XUV	Extreme ultraviolet
RESI	Re-collision-induced excitation with subsequent field ionisation
NSDI	Non-sequential double ionisation

Chapter 1

Introduction

Ever since the invention of the camera humans have been trying to use light to measure and time-resolve events that occur faster than the naked eye can observe. Electronic motion in atoms and molecules takes place on the attosecond time scale. For example in the Bohr model of the hydrogen atom it takes an electron in the ground state approximately 150 as (1as = 10^{-18} seconds) to orbit the proton [1]. If we wish to time-resolve electron dynamics within atomic and molecular systems we need laser pulses whose duration is also on the attosecond time scale. The development of mode-locking in 1964 [2, 3] resulted in a large reduction of the duration of laser pulses, which then reached a plateau from the mid-eighties to early 2000, see Fig. 1.1. However, just over the last decade, utilising the principle of high-order harmonic generation (HHG) [4, 5] has resulted in producing ultrashort laser pulses with duration of hundreds to tens of attoseconds [6]. The field of Attosecond science was born. Attosecond science encompasses the production and the characterisation of attosecond pulses as well as their theoretical and experimental applications [1, 7–9].

1.1 High-order harmonic generation

Using the principle of high-order harmonic generation, the first attosecond pulses were produced in 2001 including a single attosecond pulse [10] and a train of identical attosecond pulses [11]. HHG involves exposing an atom or a molecule to an intense infrared (IR) pulse normally with femtosecond (1 fs = 10^{-15} seconds) duration. The principle

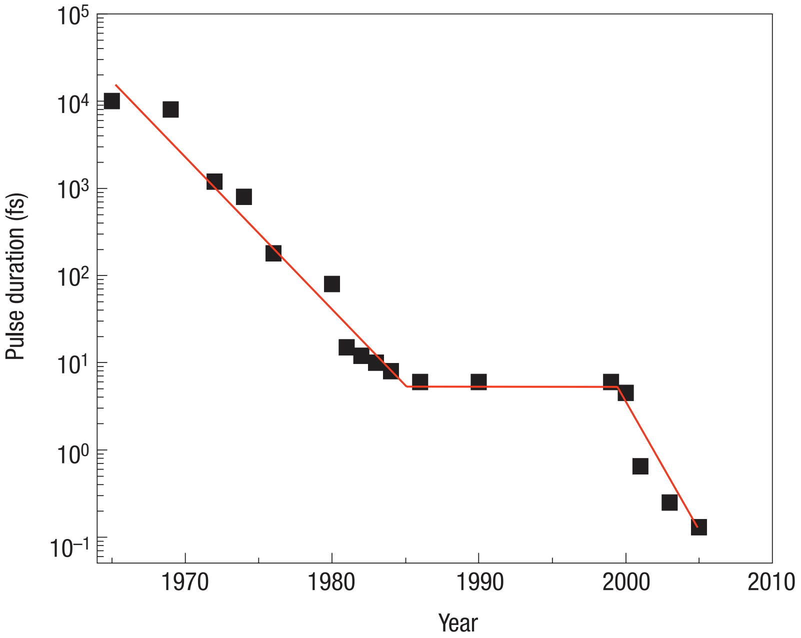

FIGURE 1.1: The minimum duration of laser pulses over the past few decades [9].

of HHG can be described by the three-step model formulated by Paul Corkum in 1993 [12]. In Fig. 1.2 we illustrate the three-step model: first, an electron tunnels out of the field-lowered Coulomb potential; then, the released electron is accelerated by the IR laser pulse; finally, the electron can return to its parent ion and recombine with the core emitting photons which are odd harmonics of the IR pulse frequency. A question naturally arises as to what is the maximum energy an emitted photon can have. This maximum energy is called the cuff-off energy and for an IR laser with field strength F and angular frequency ω is given by,

$$E_{max} = I_p + 3.17\mathrm{U_p}, \tag{1.1}$$

where I_p is the ionisation potential of the electron that tunnel ionises and $\mathrm{U_p} = F^2/4\omega^2$ in atomic units is the ponderomotive energy of the laser field [12]. The second term in Eq. (1.1) is the maximum kinetic energy the electron that tunnel-ionises can return to the core with. Electrons with the maximum kinetic energy tunnel ionise roughly when the phase of the electric field of the laser pulse is 17° past the field extremum [12]. These electrons return and recombine with the ion core about 2/3 of an optical cycle later [9]. Since there are two field extrema in each laser cycle, emission of photons with the maximum kinetic energy occurs in attosecond bursts half a period apart. A train of identical attosecond pulses can therefore be produced by selecting only photons with the cut-off energy [9]. For time resolution experiments a single attosecond pulse, also referred to as an isolated attosecond pulse, would be most useful. In order to produce a single attosecond pulse it is necessary to use an IR pulse short enough such that only one field extremum contributes to the release of the highest energy photons. The shortest attosecond pulse to date is only 67 as long [13]. The frequencies of the attosecond pulses produced using HHG are in the extreme ultraviolet (XUV) to the soft X-ray regime [13–15]. This implies that attosecond pulses are ideal for triggering ionisation events involving inner-shell electrons.

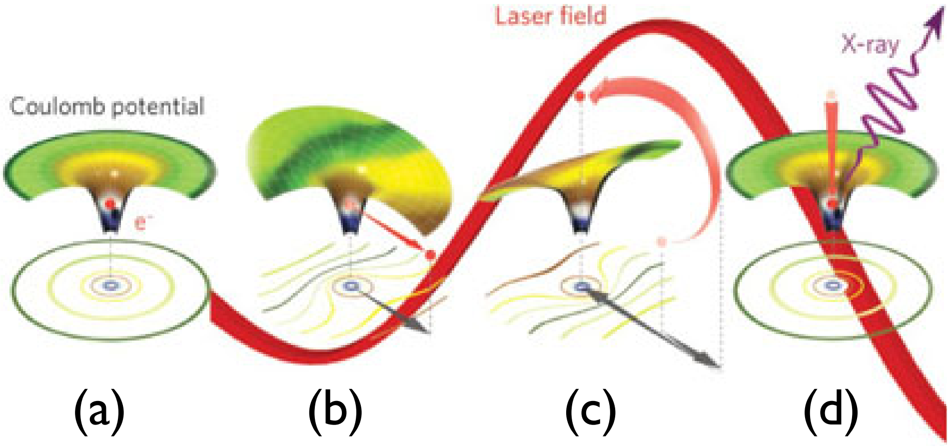

FIGURE 1.2: Illustration of the three-step model [16]. (a) An electron in the atomic Coulomb potential; (b) the electron tunnel ionises near the maximum of the laser field and then accelerates in the laser field; (c) the electron accelerates back towards the parent ion; (d) the electron re-combines with the parent ion roughly 2/3 of an optical period of the field after the tunnel ionisation and a high energy photon is emitted.

1.2 Attosecond streaking

The principle used for probing electron dynamics involving one electron escaping to the continuum is called the attosecond streak camera [17]. The underlying idea of the attosecond streak camera is that the attosecond pulse causes an atom to ionise by single photon absorption; in addition, this ionisation process occurs in the presence of an IR field. This IR field is usually the IR femtosecond pulse used to produce the XUV or X-ray attosecond pulse by HHG. The IR laser field acts as an “attosecond clock” mapping the asymptotic spectra of the escaping electron to the escaping electron dynamics. This pump-probe technique, with the XUV or X-ray attosecond pulse being the pump and the IR laser field being the probe is often referred to as attosecond streaking. The IR laser field can be a linearly polarised electric field of the form $\bar{F}(t) = F(t)\hat{\varepsilon}\cos(\omega t + \phi)$, where $F(t)$ is the pulse envelope, ϕ is the carrier-envelope phase and $\hat{\varepsilon}$ is the polarisation vector of the IR laser field. In the adiabatic limit [18] the pulse envelope varies slowly in time compared to the oscillation of the pulse, that is, $dF/dt << F\omega$ and the change in momentum of the electron escaping to the continuum is given by

$$\Delta\bar{p} = -\int_{t_r}^{\infty} F(t)\hat{\varepsilon}\cos(\omega t + \phi)dt \approx \frac{F(t_r)}{\omega}\hat{\varepsilon}\sin(\omega t_r + \phi), \tag{1.2}$$

where t_r is the time the electron is released into the continuum and "feels" the electric field. Thus, the change in momentum depends on the time the electron enters the continuum making it an ideal observable for "timing" the ionisation event.

The principle of the attosecond streak camera has been used in many experiments. Attosecond pulses were first used to measure the lifetime of inner-shell vacancies in krypton [19]. Other examples of attosecond pulse experiments include: measuring the delay of photoemission between $4f$ and valence conduction electrons in a crystal of tungsten [20]; measuring the delay of photoemission of 2p electrons relative to 2s electrons in the ionisation of neon [21]; the observation of electron tunnelling in the ionisation of neon [22]. Attosecond pulses have also been used to completely characterise laser pulses of femtosecond duration[23]. They have also been used to measure the frequency of the oscillations of an electron between two states of krypton [24]. Each of these experiments shows just how much information regarding intra-atomic electron dynamics can now be accessed using attosecond pulses. Finally the concept of the attosecond streak camera also underlies methods used in measuring the duration and chirp of attosecond pulses such as the frequency-resolved optical gating for complete reconstruction of attosecond bursts (FROG CRAB) [25].

To illustrate the concept of the one-electron streak camera we consider next a specific example, the measurement of delay between the time of photoemission of inner-shell $4f$ electrons compared to the time of photoemission of valence conduction electrons ($6s$ and $5d$ orbitals) in a tungsten crystal [20]. A 300 as pulse, with a 91 eV central frequency, triggers the photoemission. As the binding energies of the $4f$ and conduction electrons are significantly different, one can infer the type of electron by its final kinetic energy in the continuum. The photoemission caused by the attosecond pulse occurs while dressed in a IR pulse of 5 fs duration. This is repeated multiple times, each time varying the arrival of the IR pulse relative to the arrival of the attosecond pulse. This produces different photoelectron spectra. The photoelectron spectra as a function of the relative delay between the IR pulse and the attosecond pulse can be seen in Fig. 1.3(a). Varying the relative arrival time is effectively the same as varying ϕ in Eq. (1.2). Plotting the photoelectron spectra as a function of the relative arrival time shows clear oscillations in the energy of the electrons. As stated before, the momentum changes as a function of the time of release into the continuum and thus so does the energy. Therefore a difference in the time of photoemission of the $4f$ electrons relative to the conduction electrons translates into oscillations in the energy of the electrons that are slightly out of phase with each other, this can be seen in Fig. 1.3(b). Measuring the phase difference gives the delay time between the photoemission of conduction and the $4f$ electrons, which is found to be 110±70 as in agreement with theory [26].

1.3 Correlated electron dynamics

In this thesis we address multi-electron correlation in ionisation processes triggered by single-photon and XUV attosecond pulses in atoms and by IR laser pulses in molecules. These are highly complicated processes involving many degrees of freedom. Given the current computational capabilities most of these processes are out of reach of quantum mechanical ab-initio techniques. We thus employ novel quasi-classical and semi-classical techniques in order to elucidate the physical mechanisms that underly these processes. We will justify the use of classical techniques separately for each of these two processes later in this thesis.

The first part of this thesis concerns multi-electron ionisation by single-photon absorption in atoms. The correlated electron dynamics in single-photon ionisation processes is imprinted on the breakup pattern of the electrons escaping to the continuum. For excess photon energies close to the breakup fragmentation threshold, the celebrated Wannier threshold law [27] predicts that the electrons escape in the most symmetric way. That is, the breakup pattern is back-to-back for two-electron escape, an equilateral triangle for three-electron escape, a regular tetrahedron for four-electron escape and so on. However, for triple ionisation by single-photon absorption from the ground state of Li it was predicted that the breakup pattern is a T-shape and not an equilateral triangle [28].

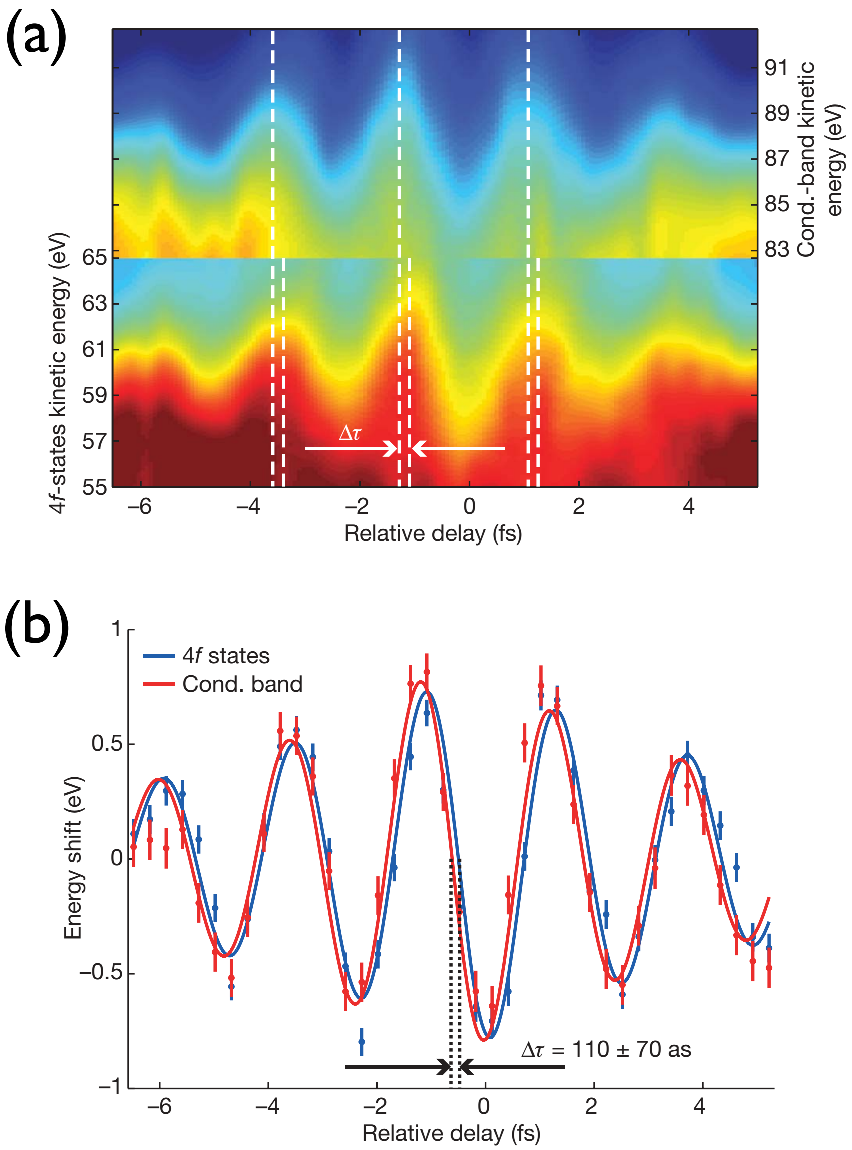

Figure 1.3: (a) The photoelectron spectra for the $4f$ (bottom) and conduction (top) electrons of tungsten as a function of the relative delay between the IR pulse and the attosecond pulse. (b) The energy shift of the $4f$ and conduction electrons as a function of the relative delay. [20].

It was later shown [29] that the breakup pattern for three-electron ionisation, close to threshold, depends on the initial state; this is contrary to what one would expect from Wannier's threshold law. This breakup pattern was shown to be consistent with the three electrons escaping in a sequence of momentum transferring attosecond three-body collisions involving the nucleus and two electrons at a time. This T-shape prediction, the result of work performed in a quasi-classical framework, was confirmed seven years later using quantum mechanical ab-initio techniques for single-photon absorption from the ground state of Li for 5 eV excess energy [30]. In Chapter 2, we extend our classical formulation to the description of quadruple ionisation by single-photon absorption from the ground state of Be. We show that close to threshold the four electrons escape on the apexes of a triangular pyramid [31]; this breakup pattern is again different than what would be expected from the Wannier threshold law. Using non-linear analysis [32], we explain why this is the case. Moreover, we show that the four-electron escape is consistent with the electrons escaping in a sequence of three-body collisions as is the case for Li. In Chapter 3, we focus on time-resolving the attosecond collision sequences that underly multi-electron escape in single-photon ionisation processes. We note that most of the current research focuses on time-resolving processes involving a single electron escape to the continuum using the one-electron attosecond streak camera. Since multi-electron ionisation is quite complex we focus on time-resolving the correlated electron dynamics during the escape of two electrons. To do so we formulate the two-electron attosecond streak camera [33] using a model system of the He(1s2s) atom.

First, we only consider a single photon energy. We show that for two-electron escape the inter-electronic angle of escape as a function of the phase lag between the attosecond pulse (single-photon) and the IR laser field carries the imprint of the correlated electron dynamics. That is, we show that the two-electron attosecond camera measures the time delay between the time of photo-absorption and the time the electron “feels” the IR laser field. We show that different energy sharings of the two electrons correspond to different physical processes which the two-electron streak camera successfully captures [34]. For equal energy sharing the delay time measured by the two-electron streak camera is the collision time (time of minimum approach) of the two electrons. We then proceed to formulate the two electron streak camera under realistic experimental conditions. That is, fully accounting for the broad spread of photon energies of an attosecond pulse, we propose a method to successfully retrieve the delay time for a given photon energy [35].

As discussed earlier attosecond pulses are generated by intense IR laser fields, thus, attosecond and strong-field science are inherently intertwined. In Chapter 4 we address multi-electron effects during the breakup of diatomic molecules by intense IR laser fields. Non-sequential double ionisation [36] and enhanced ionisation [37] are some of the pathways during the breakup of diatomic molecules by IR laser fields that have been extensively studied over the last two decades. However, this is not the case for the formation of highly excited neutral fragments during the breakup of diatomic molecules by IR laser fields. This important phenomenon, widely known as “frustrated” ionisation, was only recently observed experimentally [38] and described theoretically for linearly polarised laser fields [39]. In this thesis, we describe the semiclassical framework used to describe the breakup process in strongly driven molecules accounting simultaneously for both nuclear and electron motion at the same time. We focus on the main mechanisms leading to formation of highly excited fragments during the breakup of strongly driven H_2 in linearly and elliptically polarised laser fields. "Frustrated" ionisation during the breakup of strongly driven H_2 roughly accounts for 10% of all possible fragmentation events. Thus, our description of the mechanisms underlying this important phenomenon offer a more complete picture of the breakup of H_2 in strong IR laser fields.

Chapter 2

Quadruple ionisation of beryllium in a quasiclassical framework

In this chapter we will investigate multi-ionisation of atoms by single-photon absorption for photon energies close to threshold, i.e. photon energies just above the fragmentation threshold of an atom; multi-ionisation close to threshold is reviewed in [40]. Using only classical arguments Wannier derived a threshold law for multi-ionisation stating that $\sigma \propto (\mathrm{E}^{\mathrm{xs}})^{\beta}$ for $\mathrm{E}^{\mathrm{xs}} \to 0$, where E^{xs} is the excess energy, σ is the cross section of the ionisation process and β is the Wannier exponent [27, 41]. For a single-photon ionisation process the excess energy is defined as $\mathrm{E}^{\mathrm{xs}} = \omega - I$, where ω is the energy of the photon and I is the total energy needed to fragment the atom (ionisation energy). For two electrons, Wannier showed that close to threshold the electrons escape in the most symmetric way which is back to back [27]. For more than two electrons Wannier conjectured that electrons escape following the most symmetric break-up geometry [41], that is, three electrons escape on the apexes of an equilateral triangle and four electrons escape on the apexes of a regular tetrahedron.

In what follows we address the correlated electron dynamics in single-photon quadruple ionisation from the ground state of beryllium (Be). The correlated electron dynamics in ionisation processes is imprinted on the breakup patterns of the escaping electrons for photon energies close to the fragmentation threshold. The general expectation from Wannier's threshold law is that the breakup pattern for single-photon quadruple ionisation (QI) is a regular tetrahedron [27, 42, 43] independent of the initial state. We will show that the prevailing breakup pattern from the ground state of Be is instead a triangular pyramid [31]. The triangular pyramid breakup pattern involves three electrons escaping on the corners of an equilateral triangle with the nucleus at the centre and the fourth electron escaping perpendicular to the plane defined by the other three electrons. For three-electron escape from the ground state of Li it was recently found that the T-shape, which is also not predicted by Wannier's law, is by far the prevailing breakup pattern [28]. However, we find that this is not the case for four-electron escape. In particular, for four ionising electrons from the ground state of Be, in addition to the prevailing triangular pyramid, we find that a regular tetrahedron and a square also contribute significantly to the escape geometries; the square planar pattern involves four electrons escaping along the apexes of a square. We will investigate why the higher symmetry—compared to the triangular pyramid—tetrahedron and square planar breakup patterns of the five-body Coulomb problem do not prevail while the triangular pyramid does. Note that the tetrahedron is the breakup pattern predicted by Wannier's law to prevail close to threshold. To explore the single-photon four-electron escape from the ground state of Be, first, in Section 2.1, we use the classical trajectory Monte Carlo method (CTMC) [44, 45] to obtain the probability for QI as well as the distribution of inter-electronic angles of escape [31]. Next, to elucidate the multi-electron escape dynamics we build a model that describes QI in terms of momentum transferring attosecond collision sequences. This model is consistent with the distribution of inter-electronic angles of escape. Finally in Section 2.3 we analyse the non-linear properties of the two fixed points associated with the Coulomb singularity of a four-electron atom [29, 32].

2.1 Theory and model

The multi-ionisation of atoms is often viewed in terms of two mechanisms, "knock-out" and "shake-off" [46, 47]. The "shake-off" mechanism is purely quantum mechanical [48] and relies on the sudden approximation [49, 50]. In the sudden approximation one electron is suddenly removed from the atom. Then, the probability of a remaining electron to ionise is given by the overlap of the wave function of this electron in its initial state with that of the continuum wave function of the Hamiltonian after the sudden removal of the first electron [50]. On the other hand, the "knock-out" mechanism (sometimes called "two-step-one" [51]) can be viewed as half a (e,2e)-like collision [46, 52]. It has been shown that "knock-out" can be modelled classically [48]. The "knock-out" mechanism prevails for photon energies just above the threshold ionisation while the "shake-off" prevails for large photon energies [48, 50]. In what follows we only consider photon energies close to threshold ionisation, therefore, we only compute the "knock-out" mechanism.

We model "knock out" using CTMC, which was first introduced by Abrines *et al.* [44]. In what follows we investigate the QI of Be. The steps involved in this classical technique are selecting initial conditions from a phase space distribution and then propagating these initial conditions using the classical equations of motion [53–56]. CTMC has been extensively used in atomic physics to investigate phenomena such as charge transfer and ionisation [45] as well as electron capture [57].

2.1.1 Justification for the use of classical mechanics

Wannier justified the use of classical mechanics for the description of ionisation processes in atoms [27] as follows: in order for an electron to ionise, assuming we ignore electron-electron interactions, the kinetic energy must be greater than the potential energy, that is,

$$\frac{1}{2}p^2 \geq \frac{Z}{r}, \tag{2.1}$$

where p is the momentum of the electron, Z is the charge of the nucleus and r is the distance between the electron and the nucleus. Substituting the de Broglie wavelength $\lambda = \frac{2\pi}{p}$ in Eq. (2.1) and following some rearrangement we obtain

$$\left(\frac{2\pi^2}{Zr}\right)^{1/2} \geq \frac{\lambda}{r}. \tag{2.2}$$

Inspecting Eq. (2.2) it is clear that as the electron escapes the nucleus the term on the left becomes very small and therefore the right hand term is also very small. This then implies that the de Broglie wavelength of the electron is small compared to the distance of the electron from nucleus. We can thus claim that the motion of the electron during ionisation is essentially classical.

Previous quasi-classical studies of single-photon double ionisation from the ground and excited states of He [48, 50] and triple ionisation from the ground state of Li [58] yielded results in very good agreement with experiments and previous theories. Specifically, using the quasiclassical technique also employed in this chapter, it was found that for single-photon triple ionisation from the ground state of Li (i) the triple ionisation cross section [28] is in good agreement with experiment [59]; (ii) the computed value of 2.15 for the Wannier exponent [58] is in good agreement with the theoretical value of 2.16 [60]; (iii) the differential cross sections in energy [61] agree well with those calculated quantum mechanically [62]. Therefore, it is fully justified to extend this classical formulation to four electrons.

2.1.2 The two step model

We formulate the single-photon quadruple ionisation of Be as a two step process [52, 63]: first the single photon is absorbed by one of the electrons and then the photo-electron redistributes the acquired energy to the remaining electrons

$$\sigma^{4+} = \sigma_{abs} P^{4+}, \tag{2.3}$$

with σ^{4+} the cross section for quadruple ionisation, σ_{abs} the single-photon absorption cross section and P^{4+} the probability for quadruple ionisation. For σ_{abs} we use experimental data [64]. The results presented in this chapter do not involve cross sections so no more details are given for σ_{abs}.

We now outline the formalism we use to calculate P^{4+}. To set up our initial phase space distribution we assume that the photon is absorbed at time zero, $t = t_{abs} = 0$ by a 1s electron. That is, we assume that the photo-electron is a 1s electron and ignore absorption from a 2s orbital. This is justified since for photo-absorption at energies just above the ground-state Be threshold, the cross section from the 1s orbital is roughly 22 time larger than from the 2s orbital [65]. We label the photoelectron (from the 1s orbital) as electron 1, the other 1s electron as electron 2, and the two 2s electrons as electrons 3 and 4. The photo-electron starts at the nucleus. This is an approximation which is exact in the high energy limit [66]. We treat the remaining electrons independently, restricting them to an energy shell. Therefore the initial momentum and position of each electron is selected from the micro-canonical distribution [44, 67]. Having thus selected the initial conditions, we weight each trajectory by the Wigner distribution [68] which for the ith electron is given by

$$f_i(\bar{r}_i, \bar{p}_i) = \frac{1}{\pi^3} \int_{-\infty}^{\infty} \psi_i^*(|\bar{r}_i - \bar{z}|)\psi_i(|\bar{r}_i + \bar{z}|) \exp(2i\bar{p}_i \cdot \bar{z}) \mathrm{d}\bar{z}, \tag{2.4}$$

where $\psi_i(\bar{r}_i)$ is the hydrogen orbital for the ith electron experiencing an effective charge Z_i. Since the initial conditions for each electron are assigned independently of the other electrons the Wigner distribution is a product of Wigner distributions of the one 1s and two 2s orbitals. The reason we use the Wigner distribution is that it is the closest phase space distribution to a quantum mechanical wave function (For more details on the Wigner distribution and how we calculate the values of the Wigner distribution please see Appendix A). The effective charges are chosen to reproduce the known ionisation potential, i.e. $I_i = \frac{Z_i^2}{2n_i^2}$ where n_i is the principal quantum number of the ith electron. Therefore the effective charges are given by $Z_2 = 3.363$ ($I_2 = 5.656$ a.u.) for the 1s electron and $Z_3 = 2.314$ ($I_3 = 0.669$ a.u.), $Z_4 = 1.656$ ($I_4 = 0.343$ a.u.) for the 2s electrons [65]. Given the above considerations, the initial phase space density is therefore given by,

$$\rho(\gamma) = N\delta\bar{r}_i\delta(E_1 + I_1 - \omega) \prod_{i=2,3,4} f_i(\bar{r}_i, \bar{p}_i)\delta(E_i + I_i) \tag{2.5}$$

2.1.3 Propagation

We then propagate the five-body Coulomb Hamiltonian by integrating the classical equations of motion. We do so using regularised coordinates [69, 70] which involve coordinate and time transformations such that the Coulomb singularities in the Hamiltonian due to the electron-nucleus interactions are pairwise eliminated. In what follows we briefly describe the steps involved.

The five-body Coulomb Hamiltonian is given by

$$H = \sum_{i=1}^{4} \frac{p_i^2}{2} - \sum_{i=1}^{4} \frac{Z}{r_i} + \sum_{i>j=1}^{i=4} \frac{1}{|\bar{r}_i - \bar{r}_j|}. \tag{2.6}$$

We introduce a new coordinate system where the new position $\bar{R}_i$ and momentum $\bar{P}_i$ of the ith electron are 4-component vectors [70]. They are related to the 3-dimensional coordinates by

$$(\bar{r}_i, 0)^T = \bar{M}_i \bar{R}_i \tag{2.7}$$

and

$$(\bar{p}_i, 0)^T = \bar{M}_i \bar{P}_i / 2R_i^2 \tag{2.8}$$

with

$$M_i = \begin{pmatrix} R_{i1} & -R_{i2} & -R_{i3} & R_{i4} \\ R_{i2} & R_{i1} & -R_{i4} & -R_{i3} \\ R_{i3} & R_{i4} & R_{i1} & R_{i2} \\ R_{i4} & -R_{i3} & R_{i2} & -R_{i1} \end{pmatrix}. \tag{2.9}$$

This leads to $r_i = R_i^2$ and $p_i^2 = \frac{P_i^2}{4R_i^2}$ [70]. Substituting these new coordinates into Eq. (2.6) we obtain

$$\tilde{H} = \sum_{i=1}^{4} \frac{P_i^2}{8R_i^2} - \sum_{i=1}^{4} \frac{Z}{R_i^2} + \sum_{i>j=1}^{i=4} \frac{1}{|\bar{M}_i \bar{R}_i - \bar{M}_j \bar{R}_j|}. \tag{2.10}$$

Next, we extend the phase space to include two new canonical variables, time t, and energy of the system $E(t)$. The new Hamiltonian is given by $\Gamma = \tilde{H} - E(t)$. We introduce the time transform $dt = g d\tau$, where τ is the new time variable and g is a function of R_i's. The new Hamiltonian is $\Gamma^* = g\Gamma$ and the equations of motion are given by

$$\begin{aligned} \frac{d\bar{R}_i}{d\tau} &= \frac{\partial \Gamma^*}{\partial \bar{P}_i} & \qquad \frac{d\bar{P}_i}{d\tau} &= -\frac{\partial \Gamma^*}{\partial \bar{R}_i} \\ \frac{dt}{d\tau} &= \frac{\partial \Gamma^*}{\partial(-E(t))} & \qquad \frac{d(-E(t))}{d\tau} &= -\frac{\partial \Gamma^*}{\partial t} \end{aligned} \tag{2.11}$$

It is important that g is chosen so that the new Hamilton, Γ^*, does not contain singularities. In the simple case of two-body problem $g = R_1^2$ and the new Hamiltonian takes the form

$$\Gamma^* = \frac{P_1^2}{8} - Z, \tag{2.12}$$

which is no longer singular. The equations of motions in the regularised coordinate system in Eq. (2.11) are integrated using the 5th order Runge-Kutta method with adaptive step size [71].

2.2 Results

We compute P^{4+} for excess energies ranging from 3 to 10 eV. The threshold for QI of Be is 399 eV so 3 eV excess energy is close to threshold and the time taken to obtain good statistics using modern day computational power is not prohibitive. 10 eV is an upper bound estimate of the excess energies where the Wannier exponent β can still be retrieved. Using our data for P^{4+} from 3 to 10 eV in steps of 1 eV we find β to be 94% of the theoretically predicted value of 3.288 [43]. In the frame work of Wannier's theory, in what follows we discuss our results for 3 and 10 eV.

2.2.1 The inter-electronic angle distribution

To identify the four-electron escape pattern we use the probability for two electrons to escape with an inter-electronic angle θ - we refer to it as angular correlation probability $C(\theta)$. We use this observable as it naturally encompasses electronic correlation. We calculate the $C(\theta)$ distribution for 3 and 10 eV excess energies, see Fig. 2.1. Given that P^{4+} is 1.8×10^{-10} for 3 eV and 7.3×10^{-9} for 10 eV the computational task involved is immense. Nevertheless, to provide good accuracy, for each excess energy we consider, our results involve roughly 10^4 quadruple ionisation events. In Fig. 2.1, we see that for 10 eV $C(\theta)$ has two peaks: one around 74° and a second one around $100° - 125°$. However, for 3 eV it is not clear whether there is only one or two less pronounced peaks-compared to 10 eV-are present in the range $80° - 112°$. In Fig. 2.1, $C(\theta)$ is plotted using 28 bins for θ. We choose the bin size so that the double peak structure in $C(\theta)$ is best resolved given the limitations imposed by our statistics.

We now ask the question to what four-electron escape geometry does the shape of $C(\theta)$ correspond to? A regular tetrahedron pattern would involve all electrons escaping at 109.5° from each other. This would result in a single peak in $C(\theta)$. If it was a square pattern, with two inter-electronic angles being 180° and four inter-electronic angles being 90°, we would see two peaks in $C(\theta)$ with the peak at 90° twice as high as the peak at 180°. On the other hand a triangular pyramid pattern with three electrons escaping at 120° from each other and the other electron escaping at 90° from the three electrons would result in two peaks in $C(\theta)$ of equal height. This is because there are three inter-electronic angles at 120°, from the equilateral triangle and three at 90° from the fourth

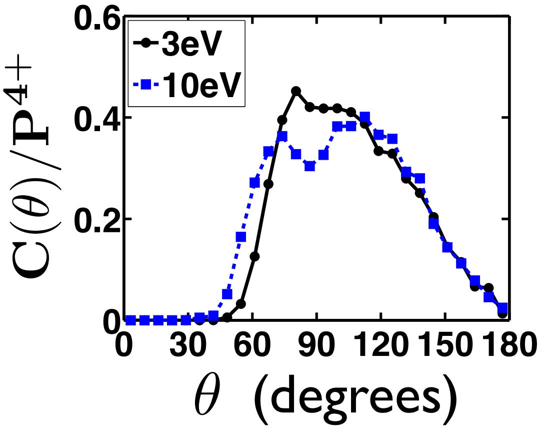

FIGURE 2.1: Probability for two electrons to escape with an inter-electronic angle θ for excess energies of 3 eV (black dots with solid line) and 10 eV (blue squares with dashed line). To guide the eye, for each excess energy, we connect the symbols representing our data with a line.

electron escaping perpendicular to the plane of the equilateral triangle. Hence, the double peak in $C(\theta)$ (Fig. 2.1) for 10 eV is consistent with a triangular pyramid shape. For 3 eV the shape of $C(\theta)$ does not provide conclusive evidence for the prevailing escape geometry.

2.2.2 Attosecond collision sequences

To better understand the angular correlation probability in Fig. 2.1 and elucidate the physical mechanisms of QI we ask the question: how does the photo-electron transfer the energy it gains from the photon to the other three electrons? This is a natural question in the framework of classical mechanics where the electrons undergo soft collisions mediated by Coulomb forces. Does redistribution of energy take place through one simultaneous collision between all 4 electrons or through a sequence of collisions? To answer this question we use a classification scheme similar to the one we first introduced in the context of three-electron escape following single-photon absorption from the ground state of Li [28]. We define a collision between electrons i and j—labelling it as $\widehat{ij}$—through the momentum transfer

$$\mathbf{D}_{\mathrm{ij}} = \int_{\mathrm{t_1}}^{\mathrm{t_2}} \nabla \mathrm{V}(\mathrm{r_{ij}})\mathrm{dt} \tag{2.13}$$

under the condition that $\mathrm{V}(\mathrm{r_{ij}}(\mathrm{t_k}))$ are local minima in time with $\mathrm{t_2} > \mathrm{t_1}$ while $\mathrm{r_{ij}} = |\mathbf{r_i} - \mathbf{r_j}|$ and $\mathrm{V}(\mathrm{r_{ij}}) = 1/|\mathbf{r_i} - \mathbf{r_j}|$. During the time interval $\mathrm{t_1} < \mathrm{t} < \mathrm{t_2}$ all five particles interact with each other. Hence, the above definition is meaningful if the collision redistributes energy primarily within the three-body subsystem that includes the nucleus and the electrons i and j. For automated identification of the collisions, we need sensitivity thresholds to register only the important collisions for the quadruple events. Due to the significantly higher complexity of the four-electron problem we introduce two sensitivity thresholds instead of one for three-electrons [28, 72]. We do so for each individual quadruply ionising trajectory by forming the maximum $\mathrm{D} = \max_{\mathrm{i}\neq \mathrm{j}}|\mathbf{D}_{\mathrm{ij}}|$ and registering only collisions with $|\mathbf{D}_{\mathrm{ij}}|/\mathrm{D} > \delta$ where $\mathrm{i}, \mathrm{j} = 1, 2, 3, 4$. We introduce another sensitivity threshold for how "sharp" a collision is. Namely, if electron i gains energy through more than one collisions, we find the maximum $\Delta \mathrm{V}_{\mathrm{i}} = \max_{\mathrm{i}\neq \mathrm{j}}(\mathrm{V}(\mathrm{r}_{\mathrm{ij}})^{\mathrm{max}} - \mathrm{V}(\mathrm{r}_{\mathrm{ij}})^{\mathrm{min}})$, with $\mathrm{V}(\mathrm{r}_{\mathrm{ij}})^{\mathrm{max/min}}$ the max/min value of $\mathrm{V}(\mathrm{r}_{\mathrm{ij}}(\mathrm{t}))$ for $\mathrm{t}_1 < \mathrm{t} < \mathrm{t}_2$, and register only collisions satisfying $(\mathrm{V}(\mathrm{r}_{\mathrm{ij}})^{\mathrm{max}} - \mathrm{V}(\mathrm{r}_{\mathrm{ij}})^{\mathrm{min}})/\Delta \mathrm{V}_{\mathrm{i}} > \delta_1$. We have checked that our results and conclusions do not change for different values of δ and δ_1; we choose $\delta = 1/12$ and $\delta_1 = 1/8$.

According to this classification scheme we find that electrons 2, 3, and 4 gain sufficient energy to leave the atom through two prevailing ionisation routes; an ionisation route is a sequence of momentum transferring collisions. In the first route the photoelectron 1 knocks out first electron 2 and then proceeds to knock out electrons 3 and 4. That is, first a collision $\widehat{12}$ takes place very early in time and roughly 24 as later collisions $\widehat{13}$ and $\widehat{14}$ occur. With collisions $\widehat{13}$ and $\widehat{14}$ taking place close in time we find that a fourth collision, $\widehat{34}$, can occur in addition to the previous three collisions. We refer to this ionisation route where the photoelectron transfers energy to both electrons 3 and 4 as $s_1 = \{\widehat{12}, \widehat{13}, \widehat{14}\}$. In the second route, the photoelectron 1 first knocks out electron 2 through the collision $\widehat{12}$. Then, electron 2 becomes the new impacting electron knocking out, roughly 24 as later, electrons 3 and 4 through the collisions $\widehat{23}$ and $\widehat{24}$. With collisions $\widehat{23}$ and $\widehat{24}$ taking place close in time a fourth collision, $\widehat{34}$, can occur in addition to the previous three collisions. We refer to this ionisation route where electron 2 transfers energy to both electrons 3 and 4 as $s_2 = \{\widehat{12}, \widehat{23}, \widehat{24}\}$. s_1 accounts for 41%,both for 3 eV and 10 eV, and s_2 for 24% for 3 eV and 26% for 10 eV of all QI events. Using this scheme of momentum transferring attosecond collision sequences we have thus obtained a physical picture of the correlated electronic motion in an intra-atomic ionisation process. Further, this scheme offers insight in choosing the appropriate asymptotic observables for inferring the temporal profile of electron-electron collision dynamics [33]. This is important since developing pump-probe schemes to time-resolve correlated multi-electron escape is one of the current challenges facing attoscience [73].

Using our classification scheme we find that two more ionisation routes are present which are less prominent compared to s_1 and s_2; we refer to them as s_3 and s_4. The s_3 ionisation route involves at least four distinct collisions: one collision is $\widehat{12}$ while two of them involve electron 3 and/or 4 each gaining energy by both electrons 1 and 2. We find that the most prominent s_3 collision sequences are $\{\widehat{12}, \widehat{13}, \widehat{14}, \widehat{23}\}$, $\{\widehat{12}, \widehat{13}, \widehat{14}, \widehat{24}\}$, $\{\widehat{12}, \widehat{13}, \widehat{23}, \widehat{24}\}$, $\{\widehat{12}, \widehat{14}, \widehat{23}, \widehat{24}\}$ each one of them contributing less than 2%. The % contribution of s_3 to all quadruply ionising events increases with decreasing excess energy from 7% for 10 eV to 11% for 3 eV. Regarding the s_4 ionisation route, it involves mainly three distinct collisions. One collision is $\widehat{12}$ while the other two collisions involve electron 3 and 4 each gaining energy by different electrons, i.e., if electron 3 gains energy from electron 1 then electron 4 gains energy from electron 2. We find that the most prominent s_4 collision sequences are $\{\widehat{12}, \widehat{13}, \widehat{24}\}$, $\{\widehat{12}, \widehat{23}, \widehat{14}\}$, with the former accounting for roughly 5.9 % and the latter for 4.1 % for 3 eV excess energy. The s_4 ionisation route accounts for roughly 10 % of all QI events for 3 eV and 10 eV excess energies.

We have now established the presence of four collision sequences each corresponding to a different ionisation route. We illustrate the collision sequences by plotting in Fig. 2.2 the probability density [72] for all inter-electronic angles as a function of time for 3 eV excess energy for the s_1 and the $\mathrm{s}_4 = \{\widehat{12}, \widehat{13}, \widehat{24}\}$ ionisation routes. We do not plot s_3 since each one of the main four s_3 collisions sequences contributes less than 2% rendering insufficient statistics. We do not plot s_2 as it provides the same insight as the s_1 pathway. To identify the collisions in the probability density we use the same two principles as for triple photo-ionisation of Li [72]. That is (i) a collision between two electrons i and j leads to a "sharp" minimum of the inter-electronic angle as a function of time, $\theta_{\mathrm{ij}} \approx 0$ (if the collision takes place almost as soon as the photo-electron is launched then the inter-electronic angle has to start with a zero value, as is the case for the $\widehat{12}$ collision) and (ii) after the collision, electrons tend to move away from each other minimising their mutual repulsive interaction; this leads to $\theta_{\mathrm{ij}} = 180^\circ$ unless either electron i or j suffers another collision through any of the other two electrons.

Using these two principles, Fig. 2.2 (left column) shows that indeed in the s_1 ionisation route electron 1 knocks-out first electron 2 very early in time while roughly 24

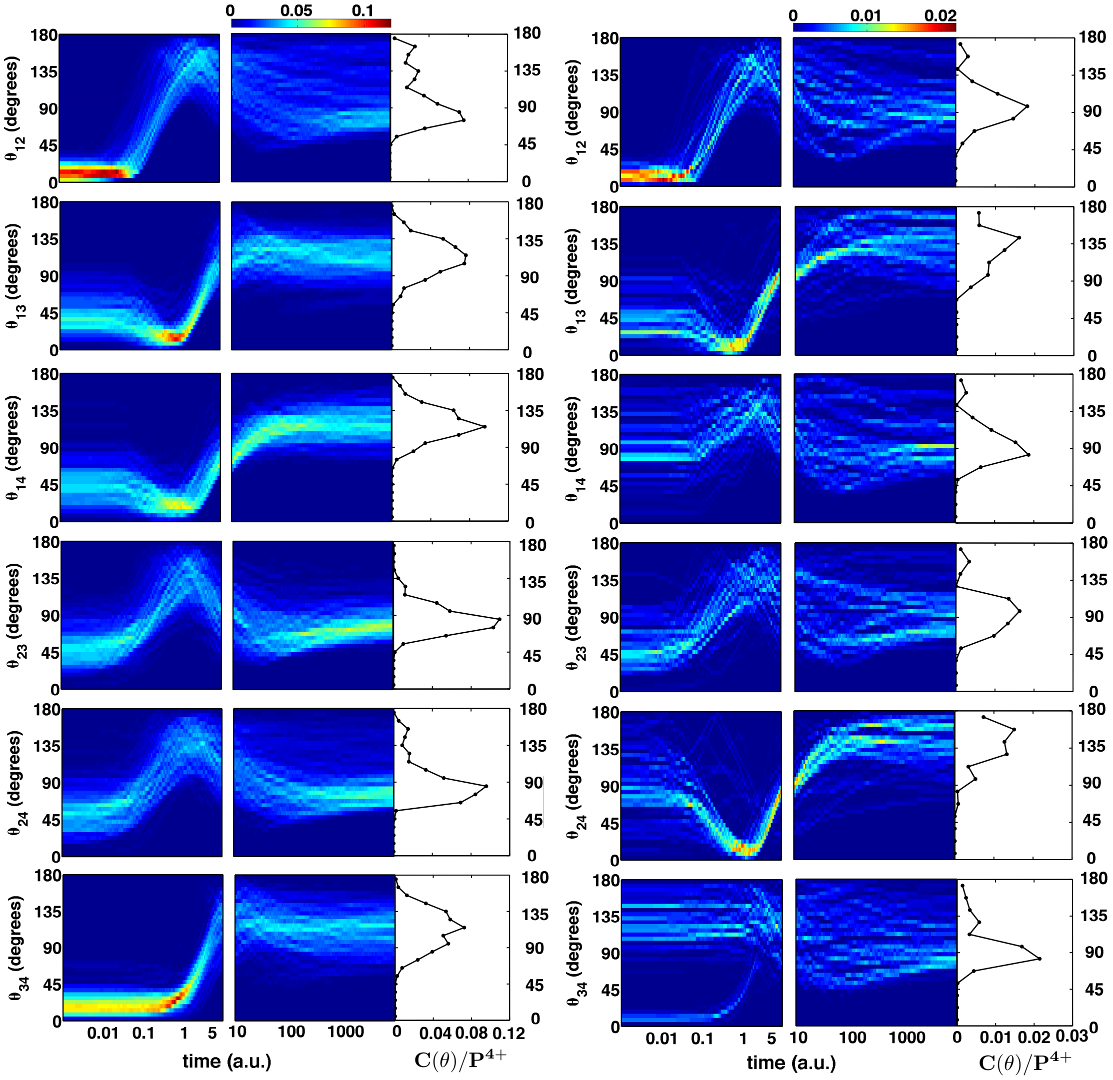

FIGURE 2.2: Probability density of the inter-electronic angles θ_{ij} for the collision sequences $\mathrm{s}_1 = \{\widehat{12}, \widehat{13}, \widehat{14}\}$ (left column) and for $\mathrm{s}_4 = \{\widehat{12}, \widehat{13}, \widehat{24}\}$ (right column).

attoseconds latter the same electron proceeds to knock-out electrons 3 and 4. Electrons 3 and 4 gain energy from electron 1 very close in time giving rise, immediately after the last collision, to the spatial distribution $r_1 \approx r_3 \approx r_4$. As a result the three electrons 1, 3, and 4 interact strongly and finally escape on a plane at 120° from each other. To minimise the potential energy, electron 2 escapes perpendicular to the plane of electrons 1,3 and 4 giving rise to a triangular pyramid [31]. Similarly, the s_2 collision sequence also gives rise to a triangular pyramid. The probability density of the θ_{34} in the s_1 collision sequence indicates that the quadruple trajectories labeled as s_1 are such that initially electrons 3 and 4 are situated close to each other thus maximising the interaction of electrons 1, 3, and 4 after electrons 3 and 4 are knocked-out by electron 1.

Although not shown here, in the s_3 collision sequence the collisions where electrons 3 and 4 each gain energy both from electrons 1 and 2 are all close in time resulting in the spatial distribution $r_1 \approx r_2 \approx r_3 \approx r_4$ immediately after the last collision. Enhancing this spatial distribution we find, but not shown here, that for the quadruply ionising trajectories labeled as s_3 electrons 3 and 4 are initially situated close to each other (as for s_1). This spatial distribution immediately after the last collision results in all four electrons escaping symmetrically on the apexes of a regular tetrahedron.

Focusing next on the $s_4 = \{\widehat{12}, \widehat{13}, \widehat{24}\}$ ionisation route we indeed see from Fig. 2.2 (right column) that electron 1 knocks-out first electron 2 very early in time and then proceeds to knock out electron 3 roughly 24 attoseconds later. This is the last collision that electrons 1 and 3 undergo and thus escape at 180° from each other. Similarly, electron 2 knocks-out, roughly at 48 attoseconds, electron 4; this being the last collision for electrons 2 and 4 they escape at 180° from each other. Minimising the potential energy the 1-3 subsystem with $\theta_{13} = 180^\circ$ and the 2-4 subsystem with $\theta_{24} = 180^\circ$ finally escape perpendicular to each other giving rise to $\theta_{12} = \theta_{14} = \theta_{23} = \theta_{34} = 90^\circ$ which is consistent with a square planar geometry. Note that the probability density of the inter-electronic angle between electrons 3 and 4, θ_{34}, in the s_4 collision sequence in Fig. 2.2 (right column) shows that electrons 3 and 4 are initially situated far from each other, in contrast to the s_1 and s_3 pathways. This initial configuration minimizes the interaction of electrons 3 and 4 thus enhancing two separate 180°-escape geometries: one corresponds to the electrons in the colliding pair $\widehat{13}$ and the other one corresponds to the colliding pair $\widehat{14}$. From the above, as already discussed in [29] for three-electron escape, we infer that what determines the final breakup geometry is the spatial distribution of all escaping electrons at the moment in time when all electrons have received enough energy (through collisions) to leave the atom, i.e., the time immediately after the last collision.

2.2.3 Prevailing breakup pattern: triangular pyramid

As discussed above, Fig. 2.2 shows that the s_1 collision sequence is consistent with a triangular pyramid breakup pattern. This is illustrated even more clearly by plotting in Fig. 2.3 the angular correlation probabilities for s_1 and s_2 at 3 eV and 10 eV. For s_1, at the time when all electrons to be ionised have received enough energy to leave the

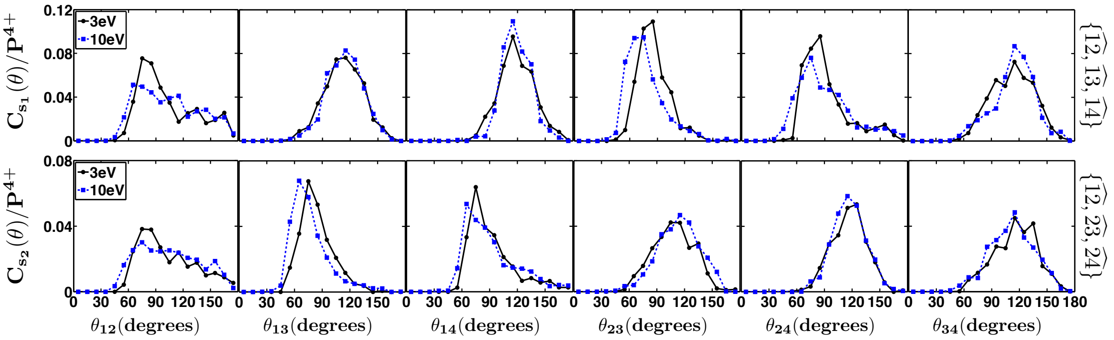

FIGURE 2.3: Same as Fig. 2.1 but for each interelectronic pair θ_{ij} for the ionisation routes s_1 (top row) and s_2 (bottom row).

atom, the spatial electron distribution, we refer to it as transient threshold configuration (TTC) [29], is $r_1 \approx r_3 \approx r_4 \neq r_2$. That is, the last colliding electrons 1, 3, and 4 have $r_1 \approx r_3 \approx r_4$, which is close to the fixed point [29] of the four-body Coulomb problem - three electrons and the nucleus. Thus, one expects that electrons 1, 3, and 4 will escape symmetrically on a plane at 120° from each other. In Fig. 2.3 (top row) we plot $C(\theta)$ for each of the six inter-electronic angles of escape using only the QI events that correspond to the s1 pathway; i.e, we plot $C_{s_1}(\theta)$. Indeed, we see that $C_{s_1}(\theta)$ for θ_{13}, θ_{14}, and θ_{34} peaks around 115°, for both 3 and 10 eV, corresponding to electrons 1, 3, and 4 escaping on the vertices of a triangle. (We note that the distributions in Fig. 2.1 and Fig. 2.3 are convoluted by the polar angle volume element sinθ resulting in a peak at 120° being shifted to slightly smaller angles while a peak at 90° is not affected). In addition, we see that $C_{s_1}(\theta)$, for θ_{12}, θ_{23} and θ_{24} peaks around $65° - 75°$ and $75° - 85°$ for 10 and 3 eV, respectively. Note that the shifting of the peak at smaller angles from $65° - 75°$ for 10 eV to $75° - 85°$ for 3 eV shows a tendency towards the triangular-pyramid-consistent angle of 90°. Thus, the distributions in Fig. 2.3 (top row) for the s_1 ionisation route are consistent with the triangular pyramid shape shown in Fig. 2.4(a). Similarly for the ionisation route s_2 , $C_{s_2}(\theta)$ for θ_{23} , θ_{24} , and θ_{34} peaks around 115° while $C_{s_2}(\theta)$ for θ_{12} , θ_{13} and θ_{14} peaks around $65° - 75°$ and 85° for 10 and 3 eV, respectively (Fig. 2.3 bottom row). Each of these distributions are consistent with the triangular pyramid shape shown in Fig. 2.4(b). Therefore, for the majority (65%) of QI events the four electrons escape on the vertices of a triangular pyramid.

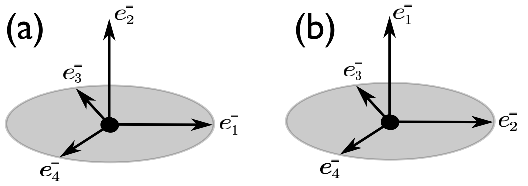

FIGURE 2.4: The triangular pyramid escape geometry for four electrons corresponding to collision sequences s_1 (a) and s_2 (b).

2.2.4 Additional breakup patterns: tetrahedron and square planar

For s_3 the TTC is $r_1 \approx r_3 \approx r_4 \approx r_2$. This spatial distribution is close to the fixed point of the five-body Coulomb problem, see Section 2.3. This fixed point corresponds to all four electrons escaping on the vertices of a regular tetrahedron at 109.5° from each other. Indeed, in Fig. 2.5(a) we find that $C_{s_3}(\theta)$ has a single peak consistent with a regular tetrahedron geometry. As expected this single peak becomes sharper with decreasing excess energy; compare $C_{s_3}(\theta)$ for 10 and 3 eV in Fig. 2.5(a). So even though the regular tetrahedron is not the prevailing breakup geometry, as generally expected, it is nevertheless present.

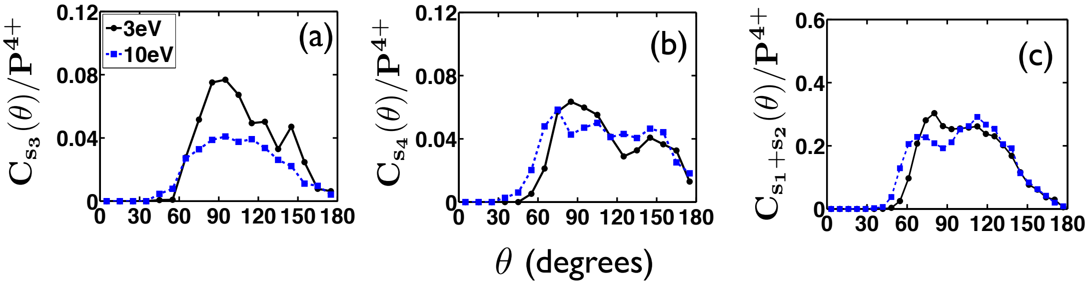

FIGURE 2.5: $C(\theta)$ for the ionisation routes s_3 (a), s_4 (b), and $s_1 + s_2$ (c). The lower statistics in panels (a) and (b) compared to those in panel (c) dictate using 18 bins [(a) and (b)] instead of 28 bins (c).

In Fig. 2.5(b) we see that there are two peaks in $C_{s_4}(\theta)$ for 3eV. One at 90° and one at 150°, the peak at 90° being twice as high as that at 150°. This is consistent with each of the four electrons escaping along the apexes of a square, with four inter-electronic angles equal to 90° and two equal to 180°. The peak at 180° is shifted to 150° in Fig. 2.5(b) due to convolution with $\sin\theta$.

We are now in a position to explain why in Fig. 2.1 the double peak in $C(\theta)$ for 10 eV is more pronounced than the one for 3 eV. Focusing on how the individual inter-electronic angles of $C_{s_1}(\theta)$ and $C_{s_2}(\theta)$ (Fig. 2.3) contribute to $C_{s_1+s_2}(\theta)$ (Fig. 2.5(c)) we find that the two peaks are closer for 3 eV (at 85° and 115°) than for 10 eV (at 65° -75° and 115°). This results in a stronger overlap and a less pronounced double peak for 3 eV in $C_{s_1+s_2}(\theta)$ which, since s_1+s_2 contribute 65% of all QI events, is also seen in the total angular correlation probability $C(\theta)$ in Fig. 2.1. Another reason for the less pronounced double peak for 3 eV compared to 10 eV is that the contribution of s_3, which has only one peak in $C_{s_3}(\theta)$ at 109.5°, is smaller for 10 eV (7%) than for 3 eV (11%).

2.3 Non-linear analysis with normal modes

We now focus on the higher symmetry—compared to the triangular pyramid—breakup patterns of the five-body Coulomb problem, namely, the regular tetrahedron and the square planar and analyse the non-linear properties of the fixed points corresponding to these two breakup geometries. The fixed points are associated with the Coulomb singularity of the five-body problem. In [29] it was shown how for three-electron escape the unstable modes of the fixed point at $\mathrm{E}^{\mathrm{xs}} \to 0$ account for the breakup patterns being initial state dependent. We next show that for four-electron escape the normal modes of the two fixed points at $\mathrm{E}^{\mathrm{xs}} \to 0$ have properties similar to the three-electron case.

2.3.1 Five-body Coulomb Hamiltonian

We start by expressing the five-body Coulomb Hamiltonian of a four-electron atom in hyperspherical coordinates, using the radial variable w instead of the hyperradius $R = w^2$

$$h = \frac{P_w^2}{8w^2} + \frac{\mathbf{\Lambda^2}}{2w^4} + \frac{C(\mathbf{\Omega})}{w^2}, \tag{2.14}$$

where $\mathbf{\Omega} = (\boldsymbol{\alpha_1}, \boldsymbol{\alpha_2}, \boldsymbol{\alpha_3}, \boldsymbol{\xi_1}, \boldsymbol{\xi_2}, \boldsymbol{\xi_3}, \boldsymbol{\xi_4}, \boldsymbol{\chi_1}, \boldsymbol{\chi_2}, \boldsymbol{\chi_3}, \boldsymbol{\chi_4})^\dagger$ contains all angular variables describing the positions of the electrons on the hypersphere of radius R. The hyperspherical coordinates are given by

$$\begin{array}{ll} R = \sqrt{r_1^2 + r_2^2 + r_3^2 + r_4^2} & \alpha_1 = Arctan(\frac{r_1}{r_3}) \\ \alpha_2 = Arctan(\frac{\sqrt{r_1^2+r_3^2}}{r_4}) & \alpha_3 = Arctan(\frac{\sqrt{r_1^2+r_3^2+r_4^2}}{r_2}) \end{array}, \tag{2.15}$$

while the relative azimuthal angles are given

$$\begin{array}{ll} \chi_1 = \phi_3 - \phi_1 & \chi_2 = \phi_4 - \phi_1 \\ \chi_3 = \phi_2 - \phi_1 & \chi_4 = \phi_1 + \phi_2 + \phi_3 + \phi_4 \end{array}, \tag{2.16}$$

with ϕ_{i}, ξ_{i} the azimuthal and polar angles of the ith electron. $\mathbf{\Lambda}$ is the so-called grand angular momentum operator [74], is a function of $\mathbf{\Omega}$ and all conjugate momenta given by

$$\begin{aligned} \mathbf{\Lambda}^2 \;=\;& P_{\alpha_3}^2 + \frac{P_{\alpha_2}^2}{\sin^2\alpha_3} + \frac{P_{\alpha_1}^2}{\sin^2\alpha_3\sin^2\alpha_2} + \frac{P_{\xi_1}^2}{\sin^2\alpha_3\sin^2\alpha_2\sin^2\alpha_1} \\ &+ \frac{P_{\xi_2}^2}{\cos^2\alpha_3} + \frac{P_{\xi_3}^2}{\sin^2\alpha_3\sin^2\alpha_2\cos^2\alpha_1} + \frac{P_{\xi_4}^2}{\sin^2\alpha_3\cos^2\alpha_2} + \frac{(P_{\chi_4}-P_{\chi_1}-P_{\chi_2}-P_{\chi_3})^2}{\sin^2\alpha_3\sin^2\alpha_2\sin^2\alpha_1\sin^2\xi_1} \;. \\ &+ \frac{(P_{\chi_4}+P_{\chi_3})^2}{\cos^2\alpha_3\sin^2\xi_2} + \frac{(P_{\chi_4}+P_{\chi_1})^2}{\sin^2\alpha_3\sin^2\alpha_2\cos^2\alpha_1\sin^2\xi_3} + \frac{(P_{\chi_4}+P_{\chi_2})^2}{\sin^2\alpha3\cos^2\alpha_2\sin^2\xi_4}. \end{aligned} \tag{2.17}$$

The total Coulomb interaction $\mathrm{V} = \mathrm{C}(\mathbf{\Omega})/\mathrm{R}$ acquires in this form simply an angular dependent charge $\mathrm{C}(\mathbf{\Omega})$ given by

$$\begin{aligned} C(\mathbf{\Omega}) =& -\frac{Z}{\sin\alpha_3\sin\alpha_2\sin\alpha_1} - \frac{Z}{\cos\alpha_3} - \frac{Z}{\sin\alpha_3\sin\alpha_2\cos\alpha_1} - \frac{Z}{\sin\alpha_3\cos\alpha_2} \\ &+\frac{1}{\sqrt{\sin^2\alpha_3\sin^2\alpha_2\sin^2\alpha_1+\cos^2\alpha_3-\sin2\alpha_3\sin\alpha_2\sin\alpha_1(\sin\xi_1\sin\xi_2\cos(\chi_3)+\cos\xi_1\cos\xi_2)}} \\ &+\frac{1}{\sin\alpha_3\sin\alpha_2\sqrt{1-\sin2\alpha_1(\sin\xi_1\sin\xi_3\cos(\chi_1)+\cos\xi_1\cos\xi_3)}} \\ &+\frac{1}{\sin\alpha_3\sqrt{\sin^2\alpha_2\sin^2\alpha_1+\cos^2\alpha_2-\sin2\alpha_2\sin\alpha_1(\sin\xi_1\sin\xi_4\cos(\chi_2)+\cos\xi_1\cos\xi_4)}} \\ &+\frac{1}{\sqrt{\cos^2\alpha_3+\sin^2\alpha_3\sin^2\alpha_2\cos^2\alpha_1-\sin2\alpha_3\sin\alpha_2\cos\alpha_1(\sin\xi_2\sin\xi_3\cos(\chi_3-\chi_1)+\cos\xi_2\cos\xi_3)}} \\ &+\frac{1}{\sqrt{\cos^2\alpha_3+\sin^2\alpha_3\cos^2\alpha_2-\sin2\alpha_3\cos\alpha_2(\sin\xi_2\sin\xi_4\cos(\chi_3-\chi_2)+\cos\xi_2\cos\xi_4)}} \\ &+\frac{1}{\sin\alpha_3\sqrt{\sin^2\alpha_2\cos^2\alpha_1+\cos^2\alpha_2-\sin2\alpha_2\cos\alpha_1(\sin\xi_3\sin\xi_4\cos(\chi_2-\chi_1)+\cos\xi_3\cos\xi_4)}} \end{aligned} \tag{2.18}$$

where the nuclear charge $Z = 4$ for Be. For details to obtain the Hamiltonian in Eq. (2.14) see Appendix B.

2.3.2 Normal modes

We next write the Hamiltonian as

$$\mathrm{H} = (h - E)w^2 \tag{2.19}$$

to ensure that the equations of motion remain regular while approaching the fixed point radially, i.e. $w \to w^* = 0$, where * denotes the fixed point value of a variable for the rest of this chapter. It was shown in [75] that the threshold dynamics is governed by motion along the normal modes of the Hamiltonian given in Eq. (2.19). To find the fixed point $\mathbf{\Omega}^*$ we solve the equations

$$\nabla_{\mathbf{\Omega}} C(\mathbf{\Omega})|_{\mathbf{\Omega}=\mathbf{\Omega}^*} = \mathbf{0}. \tag{2.20}$$

Doing so results in two sets of fixed point solutions: one set corresponds to a regular tetrahedron (T) and the other one to a square planar (SP) escape geometry. Invariance under rotation renders the values of the χ^*'s and ξ^*'s not unique and therefore we only show the values of the α^*'s in Table 2.1 which are the same for both fixed points. Next,

$\alpha_1^* = \pi/4$	$\alpha_2^* = \arctan(\sqrt{2})$	$\alpha_3^* = \arctan(\sqrt{3})$

TABLE 2.1: The values of the α hyperangles corresponding to the two fixed points.

we find the eigenvalues and eigenvectors (normal modes) corresponding to the fixed points. We do so, by expressing the equations of motion as a system of first order differential equations $\dot{\mathbf{\Gamma}} = G\nabla_{\mathbf{\Gamma}}\mathrm{H}$ for the phase space vector $\mathbf{\Gamma} = (P_w, \mathbf{P}_{\mathbf{\Omega}}, w, \mathbf{\Omega})^\dagger$, where

$$G = \begin{pmatrix} 0 & -\mathbf{1}_f \\ \mathbf{1}_f & 0 \end{pmatrix} \tag{2.21}$$

is a block matrix composed of zeroes and unity matrices of dimension $f \times f$, where f is the appropriate number of degrees of freedom; f is 12 for the regular tetrahedron (in 3-d space) fixed point and 8 for the square planar (restricted on a plane) fixed point. Since the differential equations are still singular at the fixed point $w^* = 0$ a change of the momentum variables $\mathbf{P}_{\mathbf{\Omega}}$ conjugate to $\mathbf{\Omega}$ is needed

$$p_{\Omega_j} = P_{\Omega_j}/w \tag{2.22}$$

as well as a new time variable τ related to the original time t through $dt = w^3 d\tau$; t is conjugate to the Hamiltonian given in Eq. (2.14). We thus arrive at the final equations of motion $d\boldsymbol{\gamma}/d\tau = G\nabla_{\boldsymbol{\gamma}}\tilde{\mathrm{H}}$ where $\boldsymbol{\gamma}$ refers to the new phase space variables with the (noncanonical) momenta given by Eq. (2.22). Diagonalizing the stability matrix $\partial^2 G\tilde{\mathrm{H}}/(\partial\boldsymbol{\gamma}\partial\boldsymbol{\gamma})|_{\boldsymbol{\gamma}=\boldsymbol{\gamma}^*}$ we obtain the eigenvalues and eigenvectors for the fixed points. The eigenvalues are the Liapunov exponents λ_j while the eigenvectors are the normal modes

$\delta\mathbf{u_j}(0)$, with the unit vector $\mathbf{u_j}$ defined as

$$\mathbf{u_j} = \delta\mathbf{u_j}(0)/|\delta\mathbf{u_j}(0)|. \tag{2.23}$$

We find that the regular tetrahedron fixed point has a triply degenerate eigenvalue $\lambda_1^T = \lambda_2^T = \lambda_3^T = 7.6952645$ and each eigenvalue corresponds to an unstable mode, see Table 2.2. We find that the fixed point has one more unstable mode which spans only the δw subspace and has an eigenvalue equal to $\lambda_w^T = 3.5108069$; we refer to this mode as radial. The square planar fixed point has one doubly degenerate eigenvalue $\lambda_2^{SP} = \lambda_3^{SP} = 7.6705391$ with each eigenvalue corresponding to an unstable mode and one more unstable mode with an eigenvalue $\lambda_1^{SP} = 7.9014853$, see Table 2.3. The eigenvalue corresponding to the radial (unstable) mode is $\lambda_w^{SP} = 3.4887781$. It was shown in [76] that the Wannier exponent β can be obtained from the non-linear properties of the fixed points associated with the Coulomb singularity. More specifically it was shown in [76] that $\beta = \frac{\Lambda}{2\lambda_w}$ where Λ is the sum of the eigenvalues corresponding to the unstable modes and λ_w is the eigenvalue corresponding to the w radial unstable mode. Using $\beta = (\lambda_1^{T/SP} + \lambda_2^{T/SP} + \lambda_3^{T/SP})/(2\lambda_w^{T/SP})$ from [76] we find that the Wannier exponent is equal to 3.287819 and 3.331046 for the regular tetrahedron and square planar escape geometries, respectively, in agreement with previous results [43].

The excursion from the fixed point $\delta\boldsymbol{\gamma}(\tau) = \boldsymbol{\gamma} - \boldsymbol{\gamma}^*$ is given by a linear combination of the normal modes

$$\delta\boldsymbol{\gamma}(\tau) = \sum_j c_j \exp(\lambda_j \tau)\mathbf{u_j}. \tag{2.24}$$

From Eq. (2.24) we see that the components of the phase space vector $\boldsymbol{\gamma}(\tau)$ whose excursion from the fixed point is expressed as a linear combination of only stable modes (negative Lyapunov exponents) preserve their initial ($\tau = 0$) value; these initial values determine the fixed point escape geometry; however, the components whose excursion from the fixed point is expressed in terms of unstable modes (positive Lyapunov exponents) do not necessarily preserve their initial value. From Table 2.2 and Table 2.3 we notice that for both the regular tetrahedron and the square planar the excursion of the α's, ξ's and χ's from the fixed point are expressed as a linear combination of unstable modes:

$$\delta\boldsymbol{\gamma}^T(\tau) = \exp(\lambda_1^T\tau)(c_1^T\mathbf{u_1^T} + c_2^T\mathbf{u_2^T} + c_3^T\mathbf{u_3^T}), \tag{2.25}$$

Basis	u_1^T	u_2^T	u_3^T
$\delta\alpha_1$	9.55×10^{-2}	-1.09×10^{-1}	-1.60×10^{-1}
δp_{α_1}	3.67×10^{-1}	-4.19×10^{-1}	-6.17×10^{-1}
$\delta\alpha_2$	6.60×10^{-2}	1.54×10^{-1}	-5.98×10^{-3}
δp_{α_2}	3.81×10^{-1}	8.88×10^{-1}	-3.45×10^{-2}
$\delta\alpha_3$	-1.08×10^{-1}	0	-9.92×10^{-2}
δp_{α_3}	-8.33×10^{-1}	0	-7.63×10^{-1}
$\delta\xi_1$	-2.93×10^{-3}	0	-1.34×10^{-3}
δp_{ξ_1}	-5.64×10^{-3}	0	-2.58×10^{-3}
$\delta\xi_2$	-1.95×10^{-3}	0	2.25×10^{-3}
δp_{ξ_2}	-3.75×10^{-3}	0	4.34×10^{-3}
$\delta\xi_3$	-2.64×10^{-3}	-1.99×10^{-3}	-2.18×10^{-4}
δp_{ξ_3}	-5.09×10^{-3}	-3.82×10^{-3}	-4.19×10^{-4}
$\delta\xi_4$	-2.24×10^{-3}	1.99×10^{-3}	1.13×10^{-3}
δp_{ξ_4}	-4.30×10^{-3}	3.82×10^{-3}	2.18×10^{-3}
$\delta\chi_1$	-6.14×10^{-4}	4.22×10^{-3}	-2.38×10^{-3}
δp_{χ_1}	-1.34×10^{-3}	0	-4.89×10^{-3}
$\delta\chi_2$	1.47×10^{-3}	4.22×10^{-3}	5.24×10^{-3}
δp_{χ_2}	1.34×10^{-3}	0	4.89×10^{-3}
$\delta\chi_3$	8.64×10^{-4}	8.44×10^{-3}	2.86×10^{-3}
δp_{χ_3}	5.54×10^{-4}	5.41×10^{-3}	1.83×10^{-3}
$\delta\chi_4$	0	0	0
δp_{χ_4}	0	0	0

Table 2.2: The unstable modes for the regular tetrahedron escape geometry for $\xi_1^* = \Delta/2$, $\xi_2^* = \Delta/2$, $\xi_3^* = \pi - \Delta/2$, $\xi_4^* = \pi - \Delta/2$, $\chi_1^* = 3\pi/2$, $\chi_2^* = \pi/2$, $\chi_3^* = \pi$ which is one possible solution of Eq. (2.20). Here $\Delta \approx 109.5^\circ$.

Basis	u_1^{SP}	u_2^{SP}	u_3^{SP}
$\delta\alpha_1$	1.48×10^{-1}	4.88×10^{-2}	-1.52×10^{-1}
δp_{α_1}	5.84×10^{-1}	1.87×10^{-1}	-5.83×10^{-1}
$\delta\alpha_2$	-6.97×10^{-2}	1.53×10^{-1}	-7.17×10^{-2}
δp_{α_2}	-4.13×10^{-1}	8.82×10^{-1}	-4.12×10^{-1}
$\delta\alpha_3$	8.53×10^{-2}	5.17×10^{-2}	8.78×10^{-2}
δp_{α_3}	6.74×10^{-1}	3.97×10^{-1}	6.73×10^{-1}
$\delta\chi_1$	0	-8.14×10^{-3}	0
δp_{χ_1}	0	-1.05×10^{-2}	8.58×10^{-3}
$\delta\chi_2$	0	-5.27×10^{-3}	-8.95×10^{-3}
δp_{χ_2}	0	-5.06×10^{-3}	-8.58×10^{-3}
$\delta\chi_3$	0	2.87×10^{-3}	-8.95×10^{-3}
δp_{χ_3}	0	1.06×10^{-3}	-8.58×10^{-3}
$\delta\chi_4$	0	0	0
δp_{χ_4}	0	0	0

Table 2.3: The unstable modes for the square planar escape geometry for $\chi_1^* = \pi/2$, $\chi_2^* = \pi$, $\chi_3^* = 3\pi/2$ which is one possible solution of Eq. (2.20).

and

$$\delta\boldsymbol{\gamma}^{SP}(\tau) \;=\; \exp(\lambda_1^{SP}\tau)c_1^{SP}\mathbf{u_1^{SP}} + \exp(\lambda_2^{SP}\tau)(c_2^{SP}\mathbf{u_2^{SP}} + c_3^{SP}\mathbf{u_3^{SP}}). \tag{2.26}$$

The ξ's and the χ's determine the inter-electornic angles and thus the escape geometry. As a result, the final value of the hyperangles is not necessarily equal to their initial value and therefore the final escape geometry is not necessarily the highest symmetry fixed point geometry (with the latter geometry corresponding to $\tau = 0$).

2.3.3 Fixed points and normal modes for a two-electron system

The behaviour of the four-electron fixed points is in contrast to the two-electron case where the inter-electronic angle preserves its initial value. To illustrate this we make a quick digression to the stability analysis of the two-electron ionisation in the three-body Coulomb problem. For the two-electron case only three degrees of freedom are involved, namely, the hyperradius of the two electrons R^{2e}, the hyperangle α_1 and the inter-electronic angle θ_1. The angular dependent charge $\mathrm{C}(\mathbf{\Omega})^{2\mathrm{e}}$ is given by

$$C(\mathbf{\Omega})^{2e} = -\frac{Z_{2e}}{\sin\alpha_1} - \frac{Z_{2e}}{\cos\alpha_1} + \frac{1}{\sqrt{1-\sin 2\alpha_1\cos(\theta_1)}}. \tag{2.27}$$

The fixed point corresponding to the two-electron case is $R^{2e*} = 0$, $\alpha_1^* = \pi/4$ and $\theta_1^* = \pi$. The corresponding normal modes and Liapunov exponents are listed in Table 2.4. The eigenvectors $\mathbf{u_j}$ reveal orthogonal motion along θ_1 and α_1, that is, the phase space vector $\delta\boldsymbol{\gamma}_{\alpha_1}(\tau)$ is expressed as $\delta\boldsymbol{\gamma}_{\alpha_1}(\tau) = a_{\alpha_1}e^{\lambda_1\tau}\mathbf{u_1} + b_{\alpha_1}e^{\lambda_2\tau}\mathbf{u_2}$, with $\mathbf{u_1}$ and $\mathbf{u_2}$ (Table 2.4) spanning the subspace of p_{α_1}, α_1. We also find that $\delta\boldsymbol{\gamma}_{\theta_1}(\tau) = a_{\theta_1}e^{\lambda_3\tau}\mathbf{u_3} + b_{\theta_1}e^{\lambda_4\tau}\mathbf{u_4}$, with $\mathbf{u_3}$ and $\mathbf{u_4}$ spanning the subspace of p_{θ_1}, θ_1. Thus $\delta\boldsymbol{\gamma}_{\alpha_1}(\tau)\cdot\delta\boldsymbol{\gamma}_{\theta_1}(\tau) = 0$ for all times τ. The fact that $\delta\theta_1$ is expressed in terms of two stable modes $\mathbf{u_3}$ and $\mathbf{u_4}$ implies that the value of $\theta_1 = \pi$ at $\tau = 0$, which corresponds to the highest symmetry escape geometry, is preserved for all times τ.

We have thus shown that the excursion from the fixed point of the hyperangles associated with the breakup pattern are expressed in terms of stable modes for a two-electron atom but in terms of unstable modes for a four-electron atom.

Exponent	-4.895	3.322	-0.7866 + 0.2973 i	-0.7866 - 0.2973i
Basis	$\mathbf{u_1}$	$\mathbf{u_2}$	$\mathbf{u_3}$	$\mathbf{u_4}$
$\delta\alpha_1$	-0.2	0.29	0	0
δp_{α_1}	0.98	0.96	0	0
$\delta\theta_1$	0	0	0.98	0.98
δp_{θ_1}	0	0	-0.19 + 0.073i	-0.19 - 0.073i

Table 2.4: The Liapunov exponents and corresponding eigenvectors for the fixed point of a two electron system with $Z_{2e} = 2$. The Liapunov exponent corresponding to the radial eigenvector (not shown) is 1.57317.

2.3.4 Minimization of the potential energy

We now show how the triangular pyramid is obtained from symmetry considerations in the Hamiltonian. In 2.2.2 we provided evidence that what determines the breakup pattern of the four escaping electrons is the spacial distribution (TTC) of the electrons immediately after the last collision. For the case of s_1 the TTC is $r_1 \approx r_3 \approx r_4 \neq r_2$, we assume $r_1 \approx r_3 \approx r_4 \ll r_2$, leading to $\alpha_3 \approx 0$, (the opposite case would lead to the same result). We then expand $C(\mathbf{\Omega})$ in powers of α_3:

$$C(\mathbf{\Omega}) \approx \alpha_{\mathbf{3}}^{\mathbf{-1}} \sum_{\mathbf{n=0}}^{\mathbf{3}} \mathbf{c_n} \alpha_{\mathbf{3}}^{\mathbf{n}}. \tag{2.28}$$

The lowest-order term in α_3 is

$$\begin{aligned} c_0 \;=\; & -\frac{Z}{\sin\alpha_2 \sin\alpha_1} - \frac{Z}{\sin\alpha_2 \cos\alpha_1} - \frac{Z}{\cos\alpha_2} \\ & + \frac{1}{\sin\alpha_2 \sqrt{1 - \sin 2\alpha_1 (\sin\xi_1 \sin\xi_3 \cos(\chi_1) + \cos\xi_1 \cos\xi_3)}} \\ & + \frac{1}{\sqrt{\sin^2\alpha_2 \sin^2\alpha_1 + \cos^2\alpha_2 - \sin 2\alpha_2 \sin\alpha_1 (\sin\xi_1 \sin\xi_4 \cos(\chi_2) + \cos\xi_1 \cos\xi_4)}} \\ & + \frac{1}{\sqrt{\sin^2\alpha_2 \cos^2\alpha_1 + \cos^2\alpha_2 - \sin 2\alpha_2 \cos\alpha_1 (\sin\xi_3 \sin\xi_4 \cos(\chi_2 - \chi_1) + \cos\xi_3 \cos\xi_4)}} \end{aligned} \; . \tag{2.29}$$

But c_0 is the potential term of the four-body Coulomb problem with $Z = 4$. Thus, the problem of finding a stable configuration is that of the three-electron problem with the solution $\alpha_1^* = \pi/4$, $\alpha_2^* = arctan\left(\sqrt{(}2)\right)$, $\chi_1^* = 2\pi/3$, $\chi_2^* = 4\pi/3$, and $\xi_1 = \xi_3 = \xi_4 = 90°$ [29]. These values minimise c_2 for any value of ξ_2. Minimising c_3 with respect to ξ_2, we find two solutions. One is $\xi_2 = 0°$ and the other $\xi_2 = 90°$. However only $\xi_2 = 0°$ is stable, which indeed corresponds to a triangular pyramid breakup geometry, which is of lower order symmetry than a regular tetrahedron.

From the above, it follows that if the excursion from the fixed point of the phase space variables that determine the breakup geometry is expressed in terms of unstable modes then their initial value at $\tau = 0$ is not preserved at all times. As a consequence the observable (final) breakup geometry can be different than the highest symmetry breakup geometry that corresponds to the fixed point (initial value of the relevant phase space variables). This was shown to be the case for three-electron escape in [29] and in this work for four-electron escape. We have already shown that the three-electron escape geometry is initial state dependent [29], that is, it can be an equilateral triangle (the highest symmetry breakup geometry corresponding to the fixed point of the four-body Coulomb problem) or a T-shape. We can thus safely conjecture that the four-electron escape geometry is also initial state dependent. We have shown that the prevailing breakup geometry for single-photon quadruple ionisation from the ground state of Be is a triangular pyramid and not the highest symmetry regular tetrahedron. Thus, for three or more escaping electrons the time during ionisation that determines the final breakup geometry is not the initial one that corresponds to the fixed-point highest symmetry break–up geometry but the time immediately after the last collision.

2.4 Summary

In this chapter, we have shown that a triangular pyramid is the prevailing breakup pattern for quadruple ionisation by single-photon absorption from the ground state of Be for excess energies as low as 3 eV above threshold. Employing the non-linear analysis of the fixed points of the five-body Coulomb problem we have shown why it can be the case that the highest-symmetry breakup patterns are not the prevailing ones. Our analysis of the collision sequences in four-electron ionisation re-enforces our finding in [29] that the final breakup geometry is determined by the spatial distribution of all escaping electrons at the instance in time when these electrons have received enough energy to ionise through collisions. These momentum transferring attosecond collisions are the cornerstone of our understanding of the breakup patterns for the ionisation of multi-electron atoms. In the following chapter we investigate how these collisions, that is, how the correlated electron dynamics expressed in terms of collisions can be time-resolved using the technique of atto-second streaking.

Chapter 3

Streaking of the single-photon double ionisation of metastable helium

Time-resolving correlated electron processes is a driving force behind the efforts to push the frontiers of attosecond science. Double ionisation in atoms via absorption of a single photon—photon energy above the double ionisation threshold— is an ideal process for studying correlated electron dynamics. Experimental studies of such single photoabsorption processes are traditionally performed with synchrotron radiation. While such sources offer access to the initial and final states of the fragments, they do not allow access to the intermediate states. Thus, traditional light sources leave the underlying attosecond dynamics obscure. Attosecond science fills this gap, offering time resolution through extreme ultraviolet (XUV) pulses which are temporally confined. However, pump-probe experiments using attosecond pulses are technically very challenging. Therefore, streaking of photo-electrons with an infrared (IR) laser field has become a widely used technique for bringing time resolution to photo-ionisation. The paradigmatic attosecond streak camera [17, 18], originally developed to characterize attosecond XUV pulses, has been successfully applied to resolve time-delayed emission from atoms [21, 22, 77] and solids [20]. Recently, to address electron correlation in single-photon double ionisation [33, 34], the concept of the one-electron streak camera has been extended to two electrons.

As we have seen in the previous chapter multi-electron ionisation processes in atoms can be understood in terms of momentum transferring attosecond collisions. So it is desirable to develop an experimental method that measures the timings of these collisions. Individual collisions concern two electrons and the nucleus—three-body Coulomb problem [72]. Therefore, the complete ionisation of a two-electron atom is the ideal starting point for working out how to time-resolve these attosecond collisions. We choose the single-photon absorption of He (1s2s) as a prototype system to clearly formulate the concept of streaking two-electron dynamics while avoiding the unnecessary complexity of many-electron systems. However, the scheme is not system specific. The same scheme could time-resolve, for instance, the collision between 1s and 2s electrons in the ground state of Li.

3.1 Theory and model

Using, again, the Classical Trajectory Monte Carlo method [44], we model the "knock-out" mechanism [48, 50, 63] of the double photo-ionisation (DPI) process in He (1s2s). This "knock-out" process, where the photo-electron (1s) transfers energy to the 2s electron, is depicted in Fig. 3.1. Note that, as a first step, we model the absorption of the attosecond XUV-pulse as a single-photon absorption at time $t = 0$. Later, in Section 3.4, we discuss how we account for a realistic XUV-pulse. In order to time-resolve the correlated electron dynamics in He(1s2s) following single-photon absorption we apply an infrared (IR) laser field. We model the IR laser field as an electric field polarised in

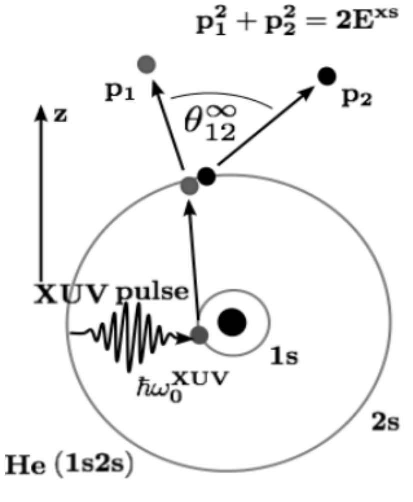

FIGURE 3.1: Sketch of the intra-atomic knock-out mechanism to be time-resolved with the two-electron streak camera [33].

the ẑ direction, which is of the form

$$\bar{F}^{IR}(t) = F_0^{IR} f(t) \cos(\omega_{IR} t + \phi)\hat{z}, \tag{3.1}$$

where F_0^{IR} is the electric field strength, ω_{IR} is the angular frequency and ϕ is the phase of the IR laser field relative to the XUV pulse. When the maximum of the streaking laser field coincides with the time when the single photon is absorbed, which is $t = 0$, the steaking phase ϕ is defined to be $\phi = 0°$ or $180°$. The function $f(t)$ is given by

$$f(t) = \begin{cases} 2T > t > 0 & 1 \\ 4T > t > 2T & \cos^2((t - 2T)\omega_{IR}/8)), \\ t > 4T & 0 \end{cases} \tag{3.2}$$

where T is the period of the IR laser field. In what follows we focus on time-resolving the correlated electron dynamics for two discrete excess energies, 10 eV and 60 eV. We define the excess energy for this system as $\mathrm{E}^{\mathrm{xs}} = \omega - I_{\mathrm{1s2s}}$. Where ω is the energy of the photon and I_{1s2s} is the potential for double ionisation of He(1s2s), 2.175 a.u./59 eV [78]. The value of F_0^{IR} is equal to 0.007 a.u. and 0.009 a.u. for 10 eV and 60 eV, respectively. These strengths are chosen so that the field is weak enough to not significantly disturb the correlated electron dynamics we wish to time-resolve but is strong enough to have an affect on the asymptotic observables. The value of ω_{IR} is equal to 0.028475 a.u. (1600 nm). The extended-phase-space Hamiltonian in regularised coordinates [69, 70], Γ^*, which was first discribed in Section 2.1.3 for conservative systems, now has an additional term due to the IR laser field

$$\begin{array}{rcl} \Gamma^* & = & \frac{1}{R_1^2+R_2^2}\left(\frac{R_2^2P_1^2}{8} + \frac{R_1^2P_2^2}{8}\right) - Z + \frac{R_1^2R_2^2}{R_1^2+R_2^2}\frac{1}{|\bar{M}_1\bar{R}_1 - \bar{M}_2\bar{R}_2|} \\ & & + \frac{R_1^2R_2^2}{R_1^2+R_2^2}(\bar{M}_1\bar{R}_1 + \bar{M}_2\bar{R}_2)\cdot\bar{F}^{IR}(t) - \frac{R_1^2R_2^2}{R_1^2+R_2^2}E(t) \end{array}, \tag{3.3}$$

where $\bar{R}_i$ and $\bar{P}_i$ are the 4-component position and momentum vectors of the ith electron, $\bar{M}_i$ is the transform matrix of the ith electron defined in Section 2.1.3, Z is the nuclear charge and $E(t)$ is the energy of the system. The time-transform g, first described in Section 2.1.3, is given by

$$g = \frac{R_1^2 R_2^2}{R_1^2 + R_2^2}. \tag{3.4}$$

In the single-photon absorption of this He(1s2s) model system, the initial conditions are very similar to those in the previous chapter. The difference is that we currently treat two instead of four electrons. Specifically, the 1s electron absorbs the photon at the nucleus [66]. The initial state of the 2s electron is modeled by the Wigner distribution of a hydrogenic orbital on a fixed energy shell. We take the ionisation potential for the 2s electron to be

$$I_{2\mathrm{s}} = I_{1\mathrm{s}2\mathrm{s}} - I_{1\mathrm{s}}, \tag{3.5}$$

where $I_{1\mathrm{s}}$ is the ionisation potential of the 1s electron in He^+, 2 a.u.. Thus, the effective charge for the 2s hydrogenic orbital is $Z_{2\mathrm{s}}$=1.184. Unlike our studies for beryllium where the initial distribution of each electron has spherical symmetry, in the current case, this symmetry is broken by the presence of the IR laser field. We account for this by weighting each trajectory with the factor $\cos^2(\theta_{p_{1s}})$ in addition to the Wigner distribution; $\theta_{p_{1s}}$ is the angle between the polarisation of the XUV pulse (the $\hat{z}$ direction) and the initial momentum vector of the 1s electron [79].

3.2 The two-electron streak camera

We briefly describe the idea underlying the two-electron streak camera, first formulated by Emmanouilidou *et al.* [33]. In Fig. 3.2 we illustrate the correlated electron dynamics that we aim to time-resolve. In particular, Fig. 3.2 shows how the excess energy is transferred from the 1s photo-electron to the 2s electron. The collision that takes place (in the three-body system) is identified by the rapid change in the inter-electronic angle, θ_{12}, for both 10 eV and 60 eV excess energies. Here, the inter-electronic angle is defined as the angle between the momentum vectors of the electrons. This rapid change occurs between 3-6 a.u. for 10 eV excess energy and 2-3 a.u. for 60 eV excess energy. We

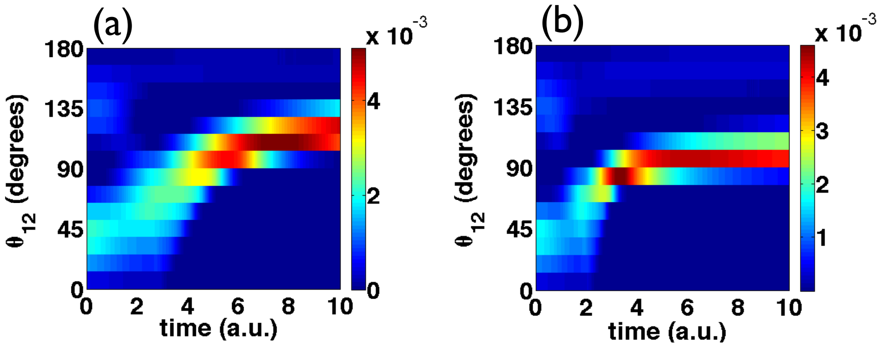

FIGURE 3.2: The probability density for the inter-electronic angle as a function of time in the field-free case at (a) 10 eV excess energy and (b) 60 eV excess energy.

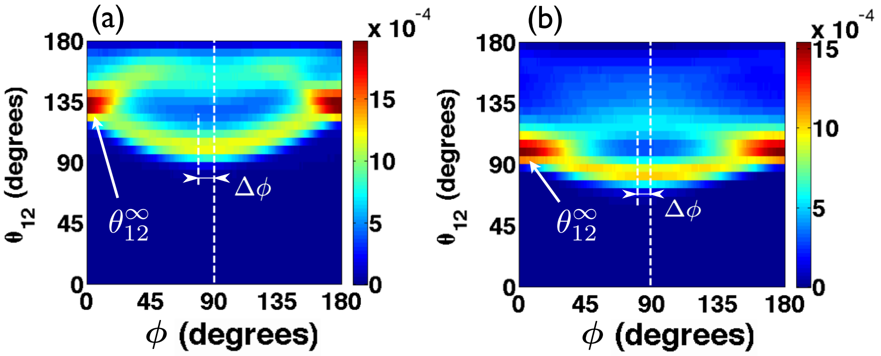

FIGURE 3.3: The probability distribution for the inter-electronic angle as a function of ϕ at (a) 10 eV excess energy and (b) 60 eV excess energy.

find that the time of minimum approach—maximum in the inter-electronic potential energy—is 2.7 a.u. for 10 eV excess energy and 1.9 a.u. for 60 eV excess energy. Thus, the time when the inter-electronic angle starts to rapidly change coincides with the time of minimum approach. Attosecond science gives us the means to monitor these collisions in real time. The aim of the two-electron streak camera is to infer the collision time from asymptotic spectra. Since, the inter-electronic angle θ_{12} is a natural measure of electronic correlation, we use the asymptotic inter-electronic angular distribution in the formulation of the two-electron streak camera.

In Fig. 3.3 we calculate the inter-electronic angle as a function of ϕ for 10 eV and 60 eV excess energy. It is clear that the distribution of the inter-electronic angle as a function of ϕ, $\theta_{12}(\phi)$, splits into two branches: one branch corresponds to values of $\theta_{12}(\phi)$ larger than θ_{12}^{∞}, while the other branch to values smaller than θ_{12}^{∞}; θ_{12}^{∞} is the asymptotic inter-electronic angle in the field-free case ($F_0^{IR} = 0$), see Fig. 3.1.

To understand the reason for the splitting seen in Fig. 3.3 we introduce a simple

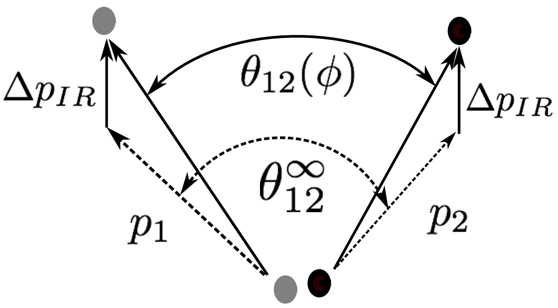

FIGURE 3.4: The streaking laser field causes a decrease in θ_{12}^{∞} when the photo-electron is launched along the $+\hat{z}$ direction, since adding Δp_{IR} to each of the electron momenta results in $\theta_{12}(\phi) < \theta_{12}^{\infty}$

model. The momentum vectors of the two electrons, both in the absence and the presence of the IR laser field, can be seen in Fig. 3.4. The asymptotic momentum vector of each electron in the presence of the IR laser field is the sum of the asymptotic momentum vector in the field-free case plus the change in momentum due to the IR laser field. In the following, the momentum and energy of each electron when the IR laser field is also present is referred to as streaked. We assume that the transfer of energy between the two electrons is sudden and that the electron motion is not affected by the IR laser field before a time t_{delay}. The change in momentum due the IR laser field given by Eq. (3.1) and Eq. (3.2) is

$$\Delta\bar{p}_{IR}(t_{delay},\phi) = -\int_{t_{delay}}^{\infty} \bar{F}^{IR}(t)\,\mathrm{d}t \;\approx \frac{F_0^{IR}}{\omega_{IR}}\sin(\omega_{IR}t_{delay}+\phi)\hat{\mathrm{z}} \tag{3.6}$$

For the rest of this thesis we refer to t_{delay} as the delay time.

From Fig. 3.4 and Eq. (3.6) the splitting of the inter-electronic angle can be understood as follows: if the momentum of the centre-of-mass of the two electrons in the field-free case points in the same direction as the IR laser field then the streaked inter-electronic angle is smaller than θ_{12}^{∞}. Note, that in the field-free case, for the majority of DPI events the direction of the momentum of the centre-of-mass of the two electrons coincides with the direction the photo-electron is initially ejected. Similarly, if the momentum of the centre-of-mass of the two electrons in the field-free case points in a direction opposite to the IR laser field then the streaked inter-electronic angle is larger than θ_{12}^{∞}. In the absence of a collision, the maximum splitting occurs at ϕ_0 corresponding to the maximum change in momentum due to the IR laser field; for the IR laser field currently under consideration, $\phi_0 = 90°$. However, the collision shifts the maximum splitting to $\omega_{IR}t_{delay}+\phi_0 = 90°$. Therefore $t_{delay} = \Delta\phi/\omega_{IR}$, where $\Delta\phi = 90° - \phi_0$. We, now, describe how to obtain ϕ_0. We restrict the analysis of the angular correlation to the smaller angles - the lower branch, see Fig. 3.5. First, the most probable value of $\theta_{12}(\phi)$ is determined for each value of the streaking phase ϕ. This yields a singly differential distribution $\theta_{12}^{max}(\phi)$, see Fig. 3.5, which is used to determine the phase ϕ_0. We find that the value of ϕ_0 is sensitive to our choice of the bin size for θ_{12} in Fig. 3.5. In order to increase the robustness of this retrieval algorithm we determine ϕ_0 for a range of bin sizes $d\theta_{12} = 4° - 9°$. We define the average of $\Delta\phi(d\theta_{12})$ as the delay time. We find that t_{delay} is equal to 4 a.u. and 2.1 a.u. for 10 eV and 60 eV, respectively. These values are in very good agreement with our predicted collision times of 3-6 a.u. and 2-3 a.u. for 10 eV and 60 eV excess energy, respectively.

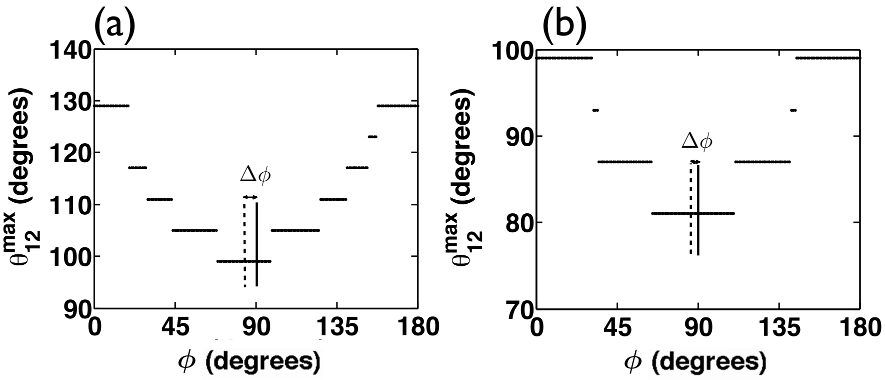

FIGURE 3.5: The inter-electronic angle with maximum probability as a function of ϕ at (a) 10 eV excess energy and (b) 60 eV excess energy for bin size in θ_{12} equal to 6°. Also shown is $\Delta\phi = 90° - \phi_0$.

3.3 Energy sharings

We, next, expand the concept of the two-electron streak camera in order to see the effect of the energy sharing between the two escaping electrons on the measured delay time. We define the energy sharing $\epsilon = |\epsilon_1 - \epsilon_2|/(\epsilon_1 + \epsilon_2)$ as the dimensionless asymmetry between the observable kinetic energies ϵ_1 and ϵ_2 of the two electrons. Using the same parameters as in the previous section, we first show that different energy sharings correspond to different double ionisation dynamics.

Our aim is to time-resolve the field-free, single-photon double ionisation process with the two-electron streak camera. We thus need to first establish a correspondence between the field-free observables and the ones modified by the streaking laser field. In Fig. 3.6, we plot the final kinetic energy sharing, KES, for every trajectory in the field-free case against its KES when subjected to the streaking laser field at (a) 10 eV and (b) 60 eV excess energy. The figure shows that the streaked energy sharing correlates with the field-free KES. Further, in agreement with experimental observations [80], the distribution of the KES shifts to more asymmetric values for higher excess energy.

After establishing a correspondence between the energy sharing in the presence and the absence of the streaking laser field, we now show that for the problem of interest, the field-free case, different energy sharings correspond to different ionisation dynamics.

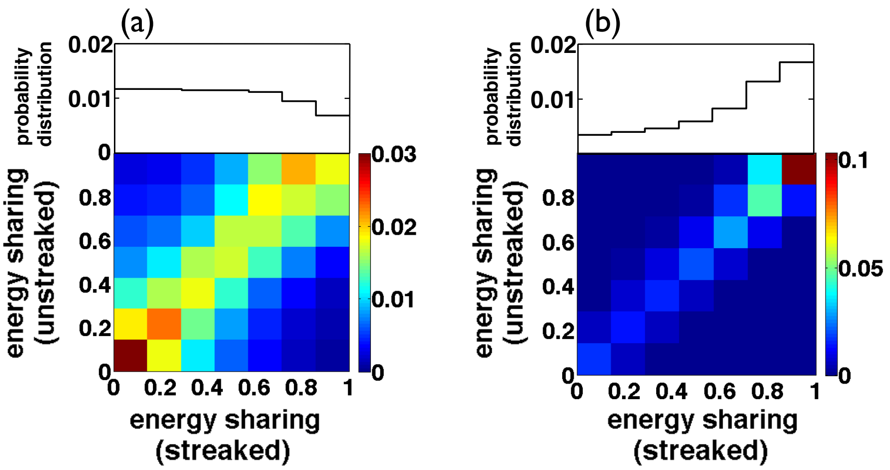

FIGURE 3.6: Correlation map of the kinetic energy sharing (KES) $|\epsilon_1 - \epsilon_2|/(\epsilon_1 + \epsilon_2)$ for two electrons produced by the absorption of a single photon with excess energy (a) $\mathrm{E}^{\mathrm{xs}} = \epsilon_1 + \epsilon_2 = 10$ eV and (b) $\mathrm{E}^{\mathrm{xs}} = 60$ eV with and without the streaking IR laser field. Also shown is the integrated energy sharing in the presence of a streaking laser field.

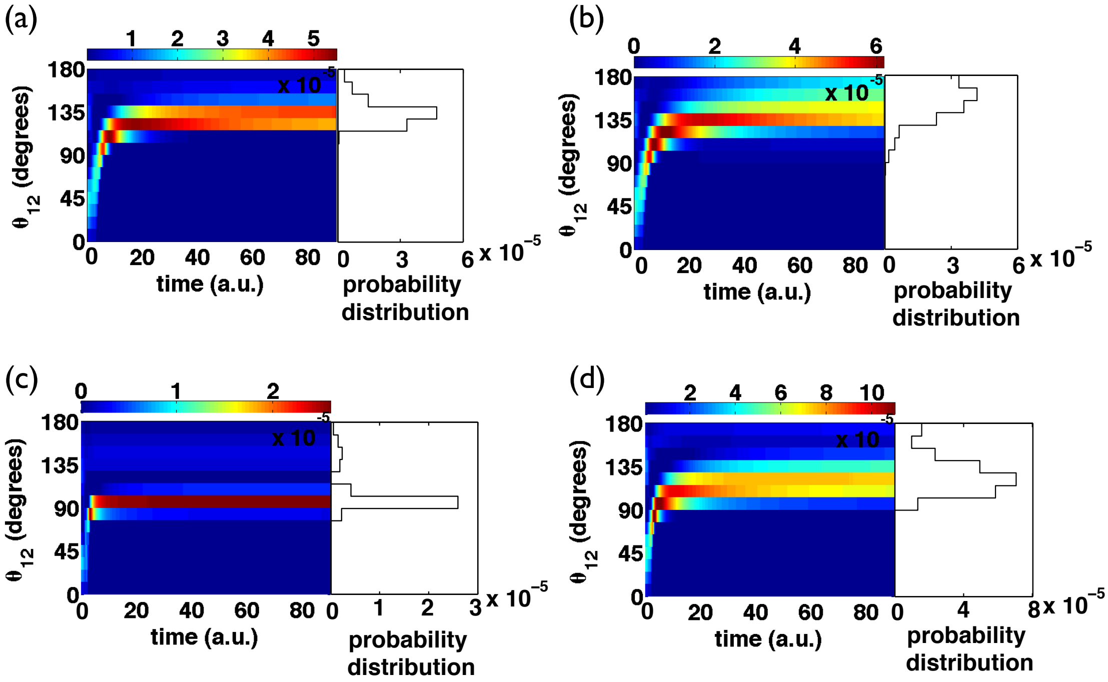

FIGURE 3.7: Time-dependent probability density of the inter-electronic angle θ_{12} of double ionisation without a streaking IR laser field. Shown are the trajectories with the most symmetric energy sharing ((a), (c)) and the most asymmetric energy sharing ((b), (d)) at 10 eV ((a), (b)) and 60 eV ((c), (d)) excess energy.

Indeed, in Fig. 3.7 we show that the temporal evolution of the correlation parameter θ_{12} for symmetric ($\epsilon < 0.14$) and asymmetric ($\epsilon > 0.86$) energy sharings is different. In Fig. 3.7, panels (a), (c) and (b), (d) correspond to the most symmetric and asymmetric energy sharings, respectively, whereas panels (a), (b) and (c), (d) correspond to an excess energy of 10 and 60 eV, respectively. In the case of symmetric energy sharing, the inter-electronic angle has only one temporal region of rapid and large change, which will, henceforth, be referred to as the "collision" time; the asymptotic value for the inter-electronic angle θ_{12} is attained rapidly within 6 and 3 a.u., for 10 and 60 eV excess energy, respectively. On the other hand, for the most asymmetric energy sharing the inter-electronic angle has two regions: a temporal region of rapid and large change, the same as that for the symmetric energy sharing, and a region of gradual change and spread into the observable asymptotic distribution. The latter region is absent in the symmetric energy sharing. These two temporal regions can be clearly seen in Fig. 3.8 for 10 eV excess energy.

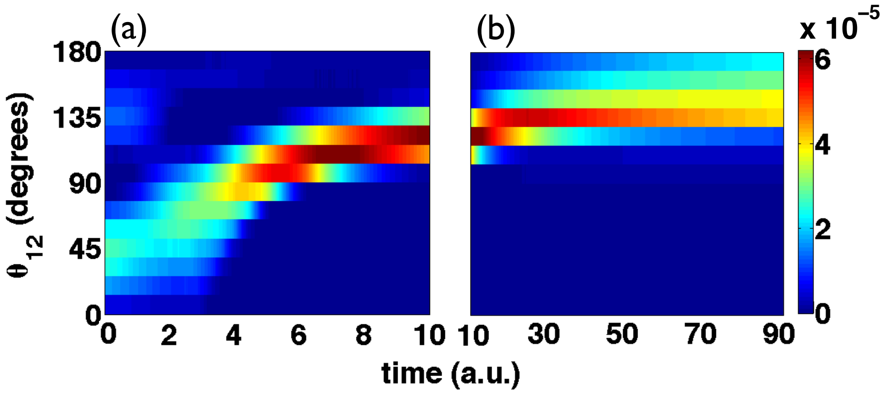

FIGURE 3.8: Enlargement of figure Fig. 3.7(b) with (a) showing the first temporal region and (b) the second one.

3.3.1 Ionisation times for different energy sharings

Besides the above shown difference in the asymptotic θ_{12}, we further quantify the difference in the two-electron ionisation dynamics for symmetric and asymmetric energy sharings. To do so, we examine the time delay between the instant of photon absorption and the time of ionisation of the slowest electron as a function of energy sharing; see Fig. 3.9. (Note that for the majority of double ionising trajectories the 2s electron is the slowest one). In Fig. 3.9(a), we plot the data for 10 eV, and in (b) for 60 eV excess energy, in the absence of a streaking laser field. The time of ionisation of the slowest electron is determined when the potential plus kinetic energy of the electron becomes permanently positive. For 10 eV excess energy (Fig. 3.9(a)), the ionisation time varies strongly with energy sharing. The delay increases roughly from 5 to 24 a.u. when the asymmetry in the final energy changes from 0-0.14 to 0.86-1. For 60 eV excess energy (Fig. 3.9(b)), the ionisation time changes roughly from 1.9 to 4.6 a.u. We also find, common to all energy sharings, that the time of minimum approach of the two electrons—maximum in the inter-electronic potential energy—is 2.7 au for 10 eV and 1.9 au for 60 eV excess energy.

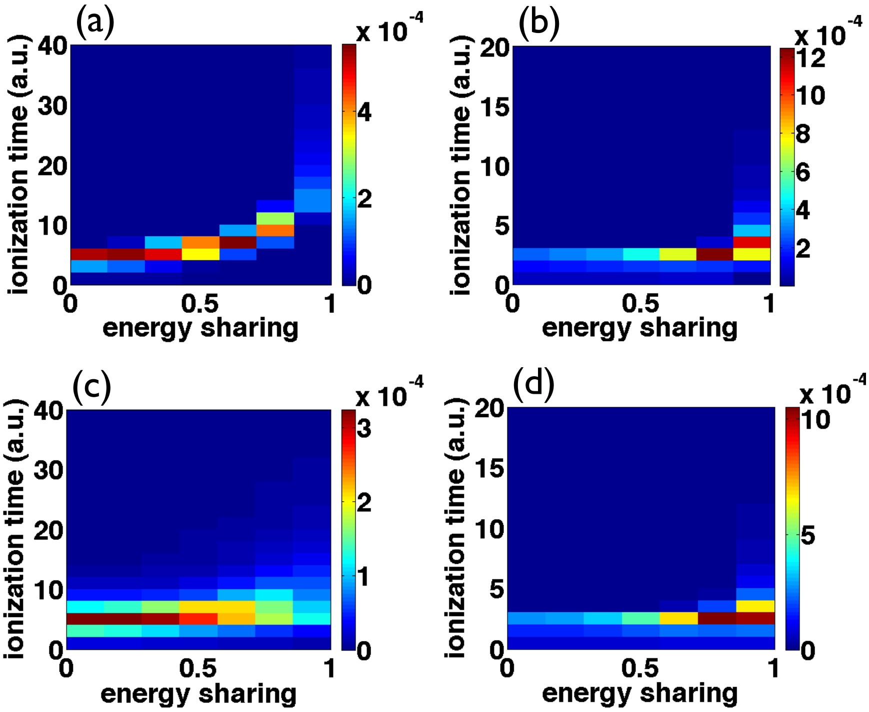

Figure 3.9: Time of ionisation of the slowest electron versus the asymptotic KES in the absence of a streaking IR laser field for (a) E^{xs} = 10 eV and (b) E^{xs} = 60 eV and in the presence of a streaking IR laser field for (c) E^{xs} = 10 eV and (d) E^{xs} =60 eV.

The above findings suggest that the first temporal region of rapid change, common to all energy sharings, corresponds to the photo-electron fast approaching the bound electron transferring part of its energy. In the symmetric energy sharing, the photo-electron transfers a large amount of energy to the other electron. As a result both electrons ionise soon after their time of minimum approach. Thus, the time delay for equal energy sharing (see Fig. 3.9) is very similar to the time of minimum approach or “collision time”, more so for 60 eV excess energy. Note that the ionisation of both electrons soon after the “collision” time is consistent with our finding of θ_{12} quickly reaching its asymptotic distribution for equal energy sharing.

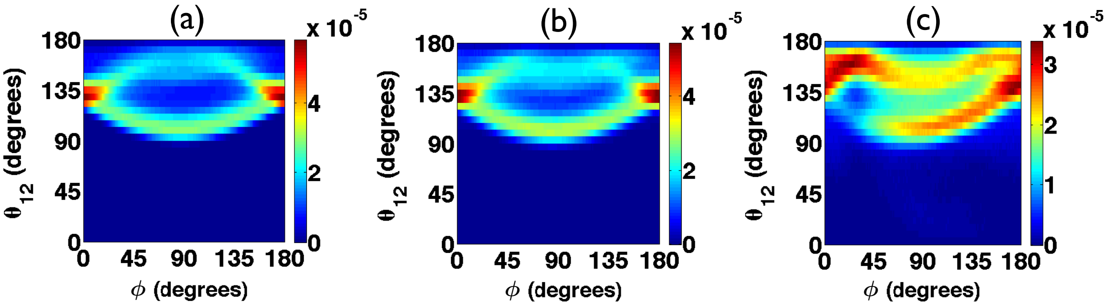

FIGURE 3.10: Streak camera plots for different energy sharings: observable interelectronic angle θ_{12} versus the streaking phase ϕ. Shown are scans for $E^{xs} = 10$ eV and an energy sharing (a) 0.0-0.14, (b) 0.43-0.57 and (c) 0.86-1.0.

For unequal energy sharing, the photo-electron first rapidly approaches the 2s electron; this is consistent with the first temporal region being common to all energy sharings. Unlike the equal energy sharing case, the photo-electron transfers only a very small amount of energy to the other electron and escapes soon after the "collision" time. In contrast, the slowest electron (mostly the 2s electron) continues its bound motion in the ion's Coulomb potential, almost independently of the photo-electron. It finally ionises with a wide spread in time delay, see Fig. 3.9(a) and (b) for asymmetric energy sharing, reflecting the strong influence of the ion's Coulomb potential. This wide spread in time delay is consistent with the second temporal region of gradual change and spread in the asymptotic θ_{12}, which is discussed above.

In summary, for equal energy sharing the time of ionisation is roughly the "collision" time corresponding to minimum approach of the two electrons, more so for 60 eV. For asymmetric energy sharing, after the "collision" time the slow electron moves roughly independently of the fast escaping photo-electron and almost solely under the influence of the ion's Coulomb potential. The large ionic Coulomb influence for asymmetric energy sharing causes a large spread in the time delay and consequently in the asymptotic θ_{12}; see Fig. 3.7(b) and (d). This spread is much larger for 10 eV compared to 60 eV since the slowest electron has much larger kinetic energy for 60 eV, making it less susceptible to the ion's Coulomb potential.

3.3.2 Attosecond streak camera for different energy sharings

We next show that the two-electron streak camera time-resolves the above-discussed time delays that correspond to different energy sharings. To compute these delay times, we follow the process described in Section 3.2 where we computed the delay time for all trajectories independent of energy sharing. In Fig. 3.10, we show the correlation plot for three different energy sharings for 10 eV excess energy.

We obtain the time delay corresponding to different energy sharings from the angular correlation plots in Fig. 3.10, in a fashion similar to the one discussed in Section 3.2. We extract the phase shift $\Delta\phi$ systematically in Fig. 3.11 for different energy sharings. For 10 eV excess energy, for an energy sharing of 0-0.14, the shift in the streaking phase $\Delta\phi$ is determined to be 4.5°; see figure Fig. 3.11(a). At a wavelength of 1600 nm a phase shift 4.5° corresponds to a delay in ionisation of 68 as or 2.8 au. At an energy sharing of 0.43-0.57, a similar lag between photo-absorption and double electron emission is found. It is only for the most asymmetric energy sharing of 0.86-1.0, (see figure Fig. 3.11(b)), that a considerably larger shift is found. The shift is about 17°, corresponding to 251 as or 10.4 au. Similarly, for 60 eV we find that the phase shift $\Delta\phi$ corresponds to a delay time of 0.3 and 4.3 au for the most symmetric and asymmetric energy sharings, respectively.

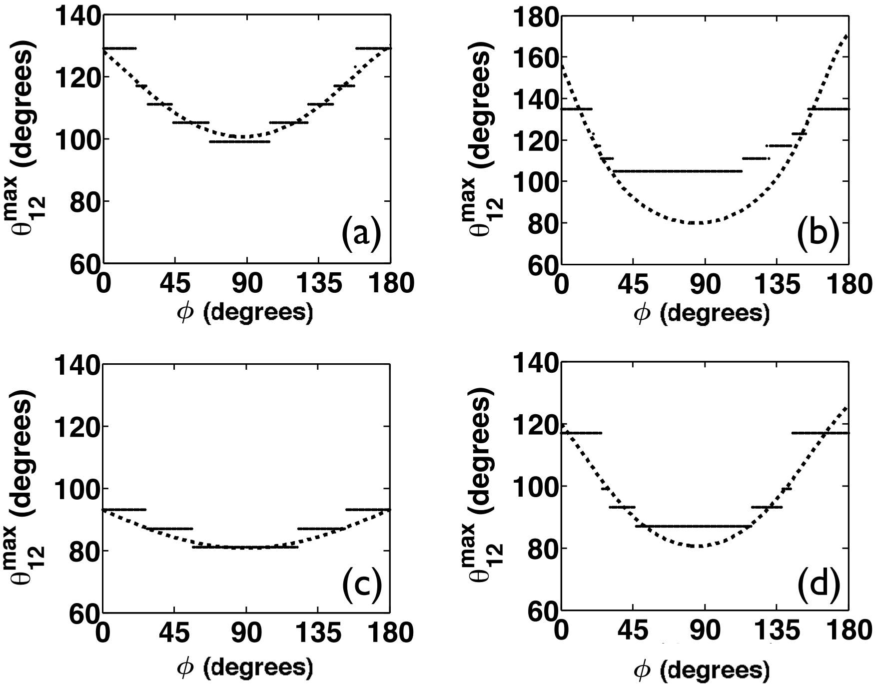

FIGURE 3.11: Fit (depicted as a dashed line) of the analytical model to the results of simulation in Fig. 3.10 (depicted as segments) for the most symmetric ((a), (c)) and most asymmetric ((b), (d)) energy sharing for 10 eV (top row) and 60 eV (bottom row) for bin size in θ_{12} equal to 6°.

We next show that we can reproduce the $\theta_{12}(\phi)$ in Fig. 3.11, by building on the simple analytical model introduced in Eq. (3.6). This way, we further confirm our interpretation of the different electron ionisation dynamics for the two extreme energy sharings. We take the x-axis on the plane defined by the z-axis and the momentum vector of one of the two electrons (due to cylindrical symmetry); let us call it electron 1. The streaked momentum vector of electron 1 is given by $\vec{P}_1(\phi) = (p_1 \sin\theta_1, 0, p_1 \cos\theta_1 + \Delta p_{IR}(t_{delay}, \phi))$. Then, the streaked momentum vector of the second electron is given by $\vec{P}_2(\phi) = (p_2 \sin\theta_2 \cos\gamma, p_2 \sin\theta_2 \sin\gamma, p_2 \cos\theta_2 + \Delta p_{IR}(t_{delay}, \phi))$, where θ_1/θ_2 is the angle between the momentum vector of the first/second electron and the z-axis, p_1/p_2 is the magnitude of the first/second electron and θ_{12} is the inter-electronic angle, with all variables defined in the field-free case; γ is given by

$$\gamma = \cos^{-1}\left(\frac{\cos\theta_{12} - \cos\theta_1 \cos\theta_2}{\sin\theta_1 \sin\theta_2}\right), \tag{3.7}$$

see Fig. 3.12. Then, the inter-electronic angle as a function of ϕ is given by

$$\theta_{12}(\phi) = \cos^{-1}\left(\frac{\vec{P}_1(\phi) \cdot \vec{P}_2(\phi)}{|\vec{P}_1(\phi)||\vec{P}_2(\phi)|}\right). \tag{3.8}$$

Apart from t_{delay} the values of the other variables, namely θ_1, θ_2 and θ_{12}, are known and chosen to be equal to their most probable values, in the field-free case, for trajectories corresponding to the lower branch. We now fit Eq. (3.8) to our results for the inter-electronic angle as a function of ϕ shown in Fig. 3.11 with t_{delay} being the only fitting parameter. We find that the analytical model fits the results better for the most symmetric energy sharing than the most asymmetric one. Indeed, not included in our model, the ion's Coulomb potential significantly influences the two-electron dynamics for asymmetric energy sharing. Moreover, our simple analytical model fits the asymmetric energy sharing for 60 eV better than for 10 eV; see Fig. 3.11(b) and (d). This is consistent with the influence of the ion's potential being less for asymmetric energy sharing for 60 eV compared with 10 eV due to the slow electron's larger final momentum for 60 eV.

Next, we discuss the time delay between the photo-absorption and the emission of both electrons as predicted by the two-electron streak camera and how it compares with the ionisation time in the field-free case, see Fig. 3.9(a) and (b). We find that there is good agreement for the symmetric energy sharing for 10 eV and the asymmetric one for

60 eV, while there is a difference of roughly 10 a.u. for the asymmetric energy sharing for 10 eV. (Note that the difference observed for the symmetric energy sharing for 60 eV is most probably due to our lower statistics for this case-for 60 eV most of the double ionisation events share the energy unequally; see Fig. 3.6.) Namely, for asymmetric energy sharing for 10 eV the streaking phase corresponds to a time delay of 10.4 a.u., while the ionisation time in the field-free case is 24 a.u. This difference can be easily understood if we also compute the ionisation times for different energy sharings in the presence of the streaking laser field; see Fig. 3.9(c) and (d) for 10 and 60 eV, respectively. Using the compensated energy as detailed in [81], we find the IR-field-present ionisation times to be very similar to the field-free ones except for asymmetric energy sharing at 10 eV excess energy. In the latter case, the ionisation time reduces from 24 a.u. in the field-free case to 13 a.u. in the presence of the IR field. The two-electron streak camera predicts a time delay of 10.4 a.u. close to the IR-field-present ionisation time of 13 a.u. This suggests that the two-electron streak camera predicts time delays similar to the ionisation time of both electrons in the presence of the IR laser field. Thus, our choice of the magnitude of the streaking laser field has to be such that the IR laser field does not significantly influence the ionisation times, as is indeed the case for 60 eV excess energy with Fig. 3.9(b) and (d) being almost identical.

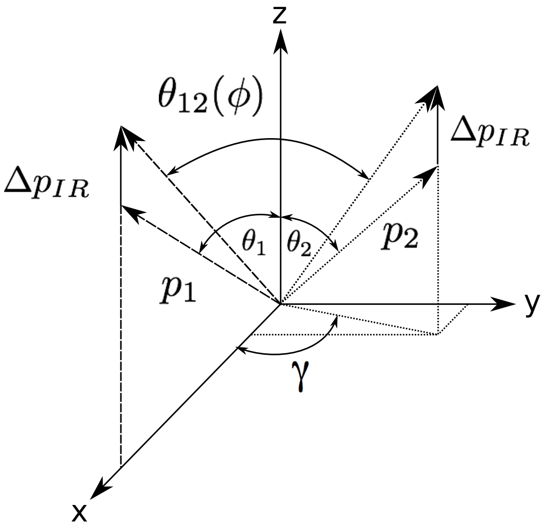

FIGURE 3.12: A three-dimensional model of the DPI of helium showing the asymptotic momentum vectors of the electron in the field-free case, p_1, p_2, the change in momentum due to the IR laser field, $\Delta p_{IR}(t_{delay}, \phi)$, and the asymptotic inter-electronic angle as a function of ϕ, $\theta_{12}(\phi)$.

3.4 The two-electron streak camera with a realistic attosecond pulse

We have seen that the two-electron attosecond streak camera is capable of time resolving the attosecond collisions involved in the double ionisation of helium. The work presented in the previous section considered only discrete photon energies and instantaneous photon absorption [33, 34]. However, an attosecond pulse would in fact have a broad spread of photon energies. This spread could be a few eV to hundred eV— shorter pulses in time have a broader minimum spread in photon energies [82]. For single-photon double ionisation, in the absence of the IR laser field and for this case of He(1s2s), the photon energy can be simply retrieved from the asymptotic energies of the two electrons by the relation $\epsilon_1 + \epsilon_2 = \omega - I_{1s2s} = \mathrm{E}^{\mathrm{xs}}$. However if the IR laser field is present, then the energy of the two electrons is not conserved. This means there is no longer a trivial relationship between the asymptotic energies of the electrons and the energy of the triggering photon.

Here, we remove this limitation and extend the two-electron streak camera technique to realistic attosecond pulses [35]. By resolving the bandwidth of an XUV-pulse in the sum energy of two emitted electrons we construct the two-electron equivalent of the frequency-resolved optical gating technique (FROG) to obtain a complete picture of the single-photon double ionisation process. Specifically, in FROG [83] one extracts from a two-dimensional data set (FROG-trace) the complete characteristics of an optical pulse. In a similar manner in FROG CRAB [25] one retrieves the spectral phases and amplitudes of an attosecond pulse. Here, we assume a transform limited XUV attosecond pulse, to obtain information about the delay of two-electron emission after absorption of a photon from the attosecond pulse. We use the inter-electronic angle of escape as a function of the phase of the IR laser field as FROG-like trace for double ionisation. In what follows, we discuss a simple algorithm we have devised for extracting the two-electron delays for different excess energies.

We use the same IR laser field given in Eq. (3.1) and Eq. (3.2) with $\omega_{\mathrm{IR}} = 0.0285$ au (1600 nm) and $\mathrm{F}_0^{\mathrm{IR}} = 0.007$ a.u. ($< 1.8 \times 10^{12}$ W/cm^2) so that the streaking laser field does not alter the attosecond collision significantly, but still has an observable effect on θ_{12}. Here, $\mathrm{F}_0^{\mathrm{IR}} = 0.007$ a.u. is chosen to efficiently streak excess energies from 10 eV to 60 eV.

3.4.1 Modelling a realistic attosecond pulse

Now we describe how we model the XUV attosecond pulse and how its spectral intensity needs to be reflected in the initial distribution of classical trajectories corresponding to different excess energies. We model the electric field of the XUV-pulse by

$$\bar{\mathrm{F}}^{\mathrm{XUV}}(\mathrm{t}) = \mathrm{F}_0^{\mathrm{XUV}} \mathrm{e}^{-\mathrm{t}^2/4\sigma^2} \cos(\omega_0^{\mathrm{XUV}} \mathrm{t})\hat{\mathrm{z}}, \tag{3.9}$$

with σ the standard deviation of the temporal intensity envelope I(t). The temporal intensity envelope I(t) of the transform limited pulse has a full width at half maximum (FWHM) of 1 a.u., see inset Fig. 3.13. For the current calculations, the spectral intensity $\tilde{\mathrm{I}}(\omega)$ of the XUV-pulse has a FWHM of 75 eV, centred at $\omega_0^{XUV} = 120$ eV, see Fig. 3.13. In what follows, we focus on the effect the large energy bandwidth of the XUV-pulse has on the streaking process and we neglect the effect of the finite FWHM of I(t). The uncertainty of the time of photo-absorption will be taken into account after the application of the streak camera algorithm as an uncertainty in the retrieved delay-times.

Using first order perturbation theory, in Appendix C, we compute the photo-absorption probability to transition from the initial ground state of He(1s2s) to the final state of double electron escape [84]

$$\mathrm{W}_{\mathrm{i}\to\mathrm{f}} \propto \frac{1}{\omega}\sigma^{++}(\omega)\tilde{\mathrm{I}}(\omega) \tag{3.10}$$

with the cross section for double ionisation, $\sigma^{++}(\omega)$, being equal to $\sigma_{\mathrm{abs}}(\omega)\mathrm{P}^{++}(\omega)$. $\sigma_{\mathrm{abs}}(\omega)$ is the cross section for photo-absorption which we calculate in the single electron approximation assuming that the 1s electron absorbs the photon [85]. $\mathrm{P}^{++}(\omega)$ is the probability for double ionisation obtained through our classical simulation described in Section 3.1. Finally, we weight each classical trajectory for a given photon energy ω by the additional factor $\sigma_{\mathrm{abs}}(\omega)\tilde{\mathrm{I}}(\omega)/\omega$ compared to the weighting factor discussed in Section 3.1.

3.4.2 “Modified” energy

Our goal is to retrieve the delay time between photo-absorption and ionisation of both electrons. Since the delay depends on the sharing of the final energy among the two

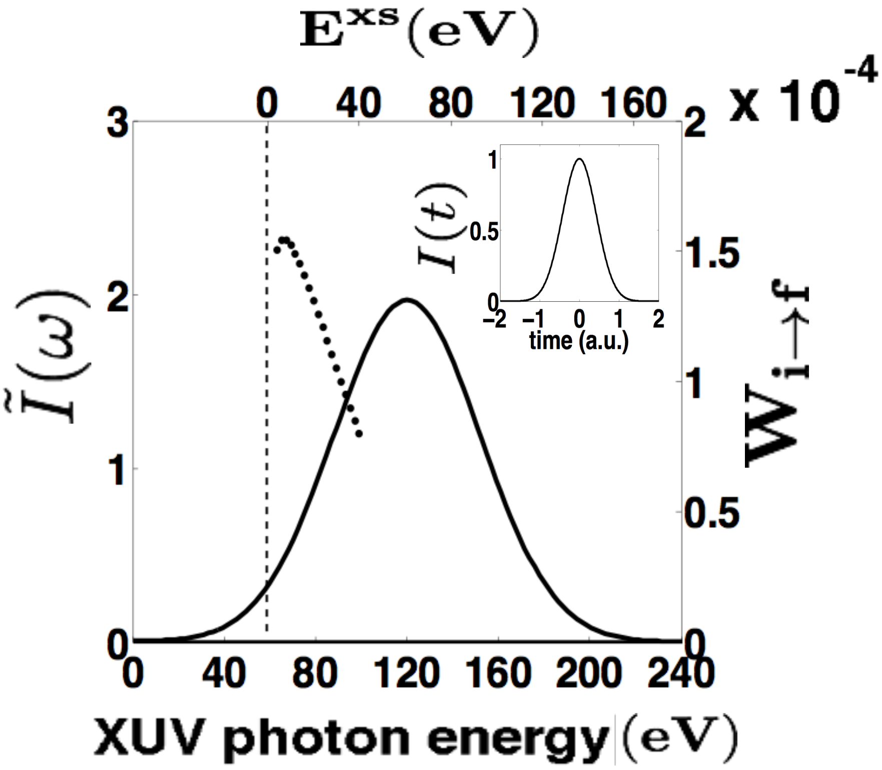

FIGURE 3.13: Spectral intensity of the XUV-pulse scaled by $(F_0^{XUV})^2$. Dotted curve: $W_{i\rightarrow f}$ in the presence of the XUV and IR laser field averaged over all $\phi's$. Inset the temporal intensity envelope.

electrons [34], we will consider in the following only symmetric energy sharing of $\epsilon < 0.14$. The delay times for the most symmetric energy sharing correspond roughly to the time of minimum approach of the two electrons, i.e. to the “collision” time. In what follows, we consider the symmetric sharing with respect to the streaked or the “modified” electron energy, as defined below. The analysis of different energy sharings as described in the previous section can be applied to the following analysis without any restrictions. In Fig. 3.14 we plot, a FROG-like trace for two-electron ejection, the observable total electron energy in the presence of the XUV plus IR laser field, E^{str} (streaked energy), as a function of ϕ for excess energies ranging from 4 eV to 60 eV in steps of 2 eV. Fig. 3.14 is plotted for symmetric streaked energy sharing. In what follows, we describe how we extract from Fig. 3.14 the delay times of the intra-atomic two-electron collisions for different triggering excess energies.

We first study the effect of the large energy bandwidth of the XUV-pulse on streaking the two-electron collision dynamics. In Fig. 3.15(a) we plot the correlation map of the excess energy of the XUV-photon and the observable sum energy E^{str} of both electrons.

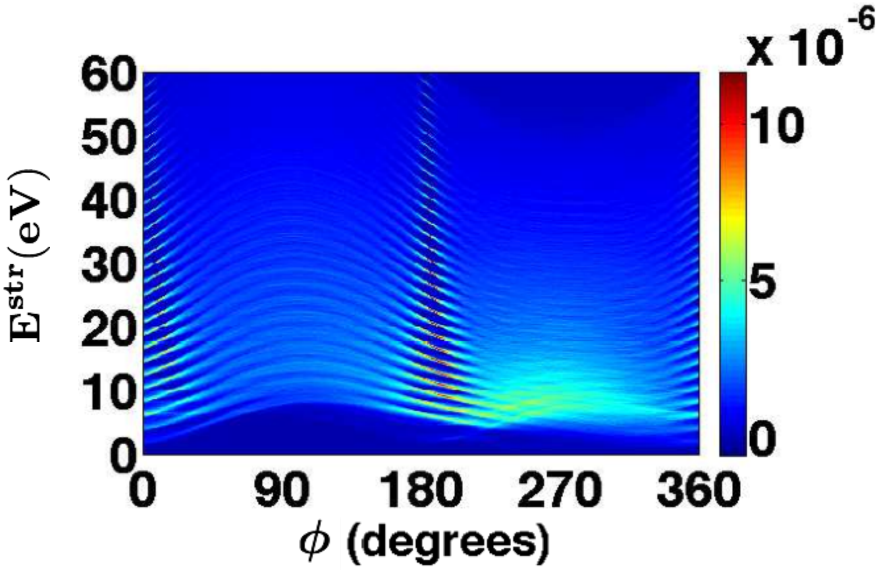

FIGURE 3.14: Observable E^{str} total electron energy, for the most symmetric energy sharing, as a function of ϕ considering excess energies from 4 eV to 60 eV in steps of 2 eV and double ionisation events corresponding to launching of the photo-electron (1s) in the $\pm\hat{z}$ direction for ϕ ranging from 0° to 180°. To illustrate the difference between launching of the photo-electron in the $+\hat{z}$ versus the $-\hat{z}$ direction we plot the E^{str} corresponding to $+\hat{z}$ for ϕ ranging from 0° to 180° and the E^{str} corresponding to $-\hat{z}$ for ϕ ranging from 180° to 360°.

We see that a large range of excess energies maps to the same streaked total electron energy. Hence, the final electronic state does not correspond unambiguously to the triggering excess energy. For instance, the 20 eV streaked energy maps to excess energies ranging from 12 eV to 26 eV. The reason for the weak correlation between the streaked and the excess energy becomes clear in Fig. 3.15(c) for 10 eV excess energy: the streaked energy changes significantly with ϕ.

To retrieve the excess energy from the final electronic state with improved accuracy, we introduce a "modified" total electron energy, where the effect of the streaking IR laser field is reduced. Therefore, we define a "modified" electron momentum p_i^{mod} by subtracting the momentum change $\Delta\bar{p}_{IR}$ due to the streaking IR laser field, i.e.

$$\bar{p}_i^{\,\text{mod}} = \bar{p}_i^{\,\text{str}} - \Delta\bar{p}_{IR}(t_{delay}, \phi), \tag{3.11}$$

where the index $i = 1, 2$ labels the two electrons. The change in momentum due to the streaking laser field (neglecting the Coulomb potential) is given in Eq. (3.6). Since we want to retrieve t_{delay} we set $\Delta\phi = 0$ when computing the "modified" electron momentum p_i^{mod}. Hence, $\Delta\bar{p}_{IR} \approx \frac{F_0^{IR}}{\omega_{IR}} \sin\phi\, \hat{z}$. Thus, the "modified" energy E^{mod} corresponding

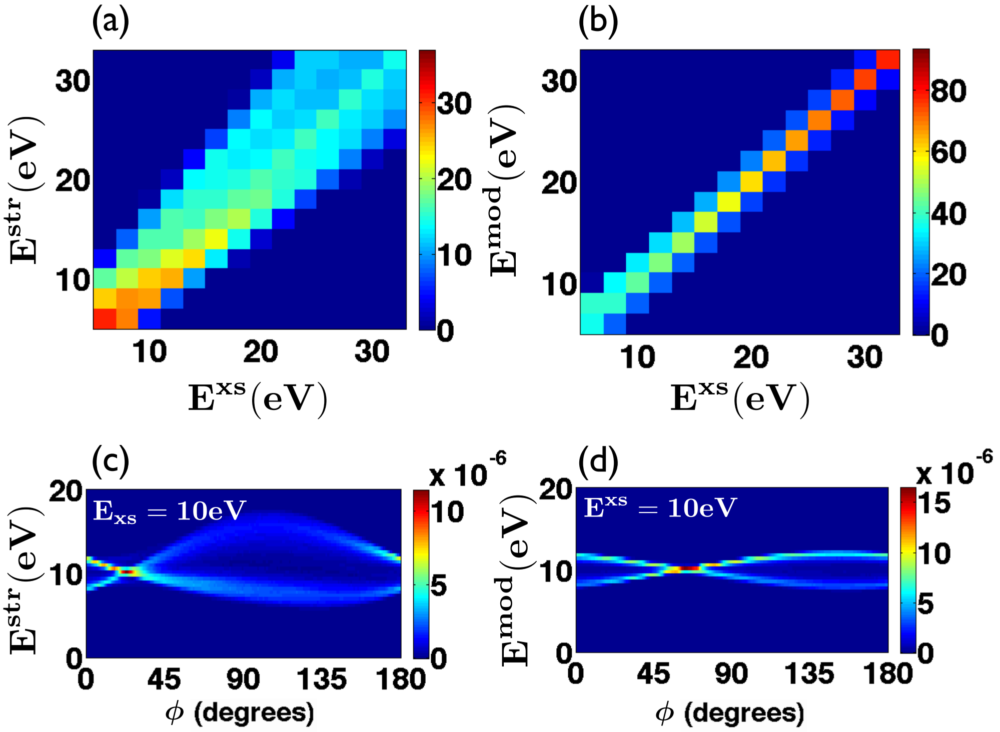

FIGURE 3.15: Correlation map of the excess energy E^{xs} (a) with the observable electron energy E^{str} and (b) with the "modified" electron energy E^{mod}. The color scale in (a) and (b) is such that the sum of E^{xs} contributing to a certain E^{str} is normalized to 100. (c) Streaked electron energy and (d) "modified" electron energy as a function of ϕ for $E^{xs} = 10$ eV excess energy. Fig. 3.15(a) and (c) are plotted for symmetric streaked energy sharing while (b) and (d) for symmetric "modified" energy sharing.

to a certain triggering photon excess energy is given by

$$\sum_{i=1,2} \frac{((p^{str}_{x,i})^2 + (p^{str}_{y,i})^2)}{2} + \sum_{i=1,2} \frac{(p^{mod}_{z,i})^2}{2} = E^{mod}. \tag{3.12}$$

Fig. 3.15(d) shows that the "modified" electron energy varies significantly less with ϕ compared to the unmodified, observable energy E^{str} (Fig. 3.15(c)). Consequently, E^{mod} is strongly correlated with the excess energy, see Fig. 3.15(b). The improved correlation at higher excess energies is likely due to the faster collision, i.e. the approximation $\Delta\phi \approx 0$ is better at higher excess energies.

We next explain why at $\phi = 0°/180°$ the streaked electron energy and as a consequence the "modified" electron energy is smaller/larger than the corresponding excess energy for photo-electrons ejected in the $+\hat{z}$ direction (it is the other way around for photo-electrons ejected in the $-\hat{z}$ direction). At $\phi = 0°$ each electron experiences a force from the IR laser field in the direction opposite to the electron's direction of escape. As

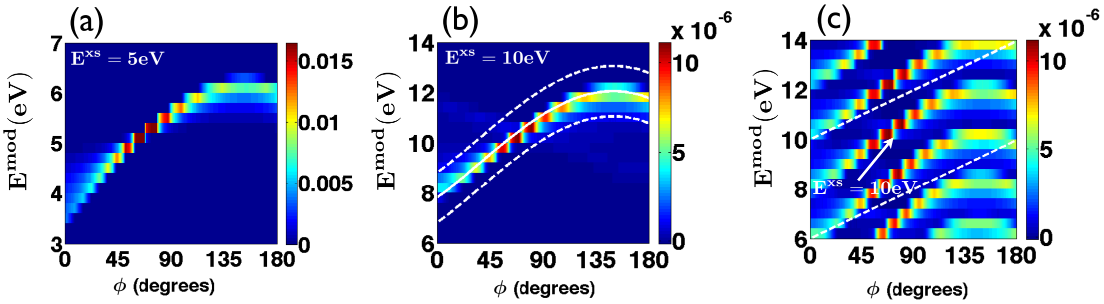

FIGURE 3.16: (a) E^{mod} for one-electron as a function of ϕ for 5 eV excess energy. (b) E^{mod} for two electrons as a function of ϕ for 10 eV excess energy; white solid line shows the average of the distribution E^{mod} in (a) times two. (c) E^{mod} for two electrons as a function of ϕ for excess energies between 4 and 14 eV. The white dashed lines enclose the doubly ionising events with $\mathcal{E}^{mod} = 10$ eV. Fig. 3.16(b) and (c) are plotted for symmetric "modified" energy sharing.

a result, each electron slows down and escapes with a streaked energy, E^{str}, smaller than the electron's final energy in the absence of the IR laser field. In contrast, at $\phi = 180°$ each electron experiences a force from the IR laser field in the same direction as the electron's direction of escape. As a result, each electron escapes with a streaked energy larger than the electron's final energy in the absence of the IR laser field. To verify that the overall change of the "modified" total electron energy with ϕ is a one-electron effect, we run our simulation in the presence of the XUV plus IR laser field only for the photo-electron (the 2s electron is absent). Since for the two-electron case we only consider symmetric energy sharing, we compare the two-electron case for a certain excess energy with the one-electron case for half that excess energy. Indeed, multiplying by two the distribution of the one-electron "modified" energy as a function of ϕ for an excess energy of, for example, 5 eV (Fig. 3.16(a)) and taking the average we find that there is excellent agreement with the two-electron "modified" energy at 10 eV excess energy as a function of ϕ, see Fig. 3.16(b). Note that in Fig. 3.16 and in what follows (Fig. 3.17(b) and (d) and Fig. 3.18) we focus on double ionisation events where the photo-electron is ejected in the $+\hat{z}$ direction.

3.4.3 Isolating individual photon excess energies

For a certain excess energy, we have shown that the "modified" electron energy increases with ϕ, see Fig. 3.16(b). This forms the basis for the simple algorithm we develop to determine, for the case when many excess energies are considered (XUV attosecond

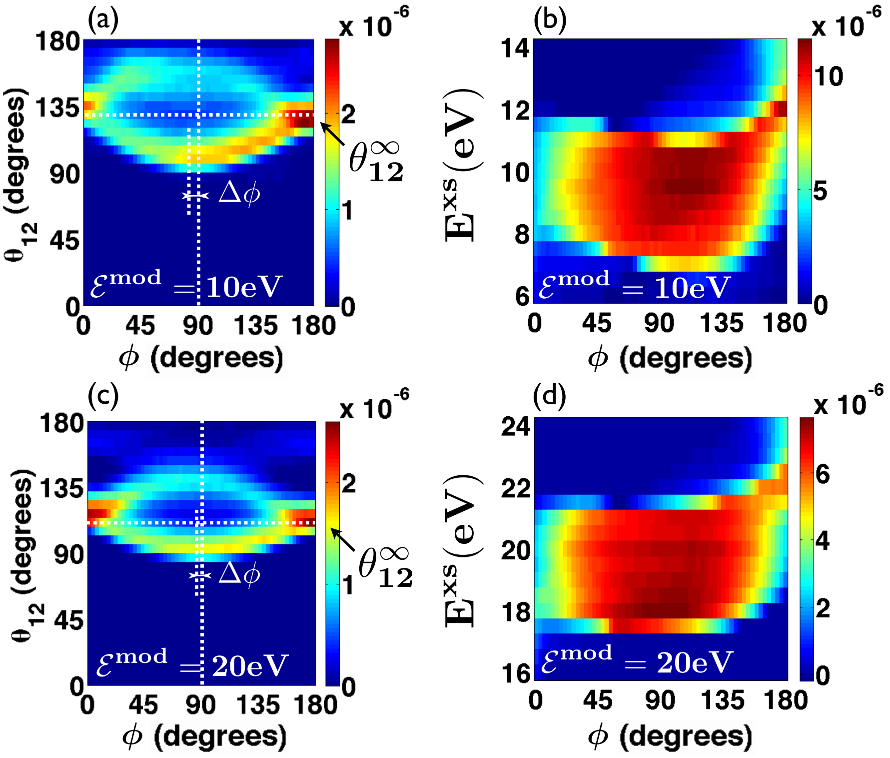

FIGURE 3.17: θ_{12} as a function of ϕ for "modified" energies around 10 eV (a) and 20 eV (c) in the presence of the XUV and IR laser field. $\Delta\phi$ is the shift of the maximum of the vector potential of the IR laser field, corresponding to a maximum of the split of θ_{12} as a function of ϕ. (b) Excess energies as a function of ϕ that contribute to the "modified" energy around 10 eV enclosed by the white dashed lines in Fig. 3.16(c) and similarly (not shown) for the "modified" energy centred around 20 eV. Fig. 3.17 is plotted for symmetric "modified" energy sharing

pulse), the range of "modified" electron energies that pertain to a certain excess energy $\mathrm{E^{xs}}$. Our goal is to select that range of "modified" electron energies that includes all double ionising events that are triggered by a narrow set of excess energies centred around $\mathrm{E^{xs}}$. The reason is that it is the double ionisation events triggered by a single $\mathrm{E^{xs}}$ whose collision time we aim to streak. We label the set of double ionisation events thus selected by $\mathcal{E}^{\mathrm{mod}}$.

If our algorithm is dictated mainly by experimentally accessible observables, we compute the collision time corresponding to $\mathrm{E^{xs}}$ by selecting the doubly ionising events whose "modified" electron energy changes from $[\mathrm{E^{xs}} - \Delta\mathrm{E}/2, \mathrm{E^{xs}}]$ eV for $\phi = 0°$ to $[\mathrm{E^{xs}}, \mathrm{E^{xs}} + \Delta\mathrm{E}/2]$ for $\phi = 180°$. We choose $\Delta\mathrm{E}$ to be roughly 8 eV for all excess energies (method 1). With this selection criterion, the double ionisation events with $\mathcal{E}^{\mathrm{mod}} = 10$ eV, enclosed by the white dashed lines in Fig. 3.16(c), are the events triggered by excess energies ranging from 7 eV to 13 eV, see Fig. 3.17(b); these excess energies are indeed roughly centred around $E^{xs} = 10$ eV for all ϕ's. Similarly, the double ionisation events we label by $\mathcal{E}^{mod} = 20$ eV are triggered by excess energies ranging from 17 eV to 23 eV, see Fig. 3.17(d); these excess energies are roughly centred around $E^{xs} = 20$ eV for all ϕ's.

To then determine the collision time corresponding to a certain excess energy, for instance, E^{xs} =10 eV/20 eV the best we can do, according to method 1, is to compute the two-electron collision time of the double ionisation events corresponding to $\mathcal{E}^{mod}$ =10 eV/20 eV. We do so and determine the collision time for $\mathcal{E}^{mod}$ =10 eV/20 eV in Fig. 3.17(a) and (c) by extracting $\Delta\phi$ from the lower branch of the inter-electronic angle of escape $\theta_{12}(\phi)$; the exact procedure for doing so is described in the previous section. We find that $\Delta\phi$ is 4.1°/1.9° corresponding to a collision time of 2.5 a.u./1.2 a.u. for $\mathcal{E}^{mod}$ =10 eV/20 eV, respectively.

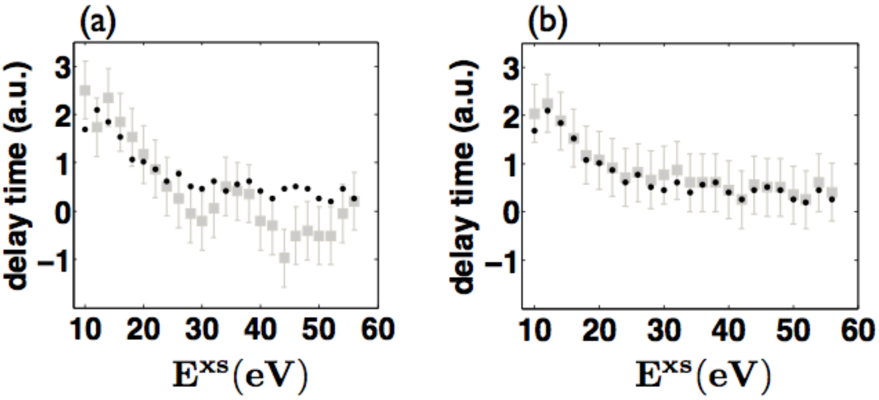

FIGURE 3.18: ☐ the collision times for "modified" electron energies $\mathcal{E}^{mod}$ from 10 eV to 56 eV; ● the collision times for pure excess energies E^{xs} ranging from 10 eV to 56 eV. Collision time was retrieved by (a) method 1 and (b) method 2. The error bars show the uncertainty in the delay times of 0.6 a.u. since we change ϕ every one degree.

In Fig. 3.17(a) and (c) we have shown how to obtain the collision time for $\mathcal{E}^{mod}$ equal to 10 eV and 20 eV respectively. Repeating the process, we obtain the collision time for $\mathcal{E}^{mod}$ ranging from 10 eV to 56 eV energies in Fig. 3.18(a). We compute the delay time using a bin size for ϕ of 1 °. Therefore, we introduce an uncertainty in the delay times of ±0.6 a.u; this is larger than the standard deviation of the XUV pulse in Eq. (3.9), which is 0.4 a.u.. We find that the collision time decreases with increasing excess energy, that is, increasing $\mathcal{E}^{mod}$. Since in our computation (but not experimentally) we can identify the double ionisation events in the presence of the XUV and IR laser field which are triggered by only a single excess energy, E^{xs}, we also compute the collision time corresponding to this excess energy, see Fig. 3.18(a). Fig. 3.18(a) shows that the retrieval algorithm for the collision time based on $\mathcal{E}^{\mathrm{mod}}$ works better at lower excess energies. The reason is that we compute the delay times corresponding to a certain $\mathcal{E}^{\mathrm{mod}}$ using $\Delta\mathrm{E} \approx 8$ eV independent of the excess energy. This choice of ΔE describes best the rate of increase of the "modified" electron energy with ϕ for smaller excess energies. However, ΔE decreases with increasing excess energy. As a result, the agreement is worse for higher excess energies.

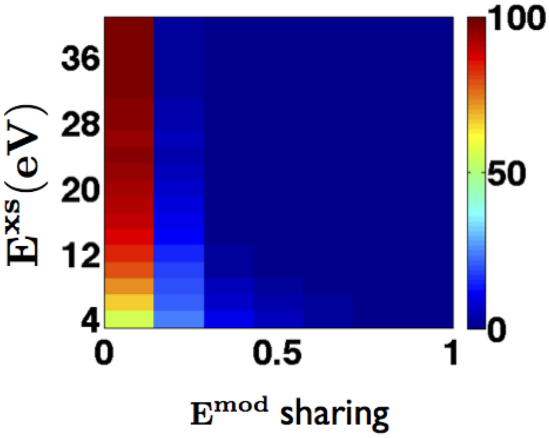

Figure 3.19: Correlation map of the excess energy with the "modified" energy sharing for the doubly ionising events with equal energy sharing in the absence of the IR laser field. The color scale is such that the sum of "modified" energy sharings contributing to the equal energy sharing double ionisation events for a certain E^{xs} is normalized to 100.

To account for the fact that ΔE changes with excess energy, we introduce a different method (method 2) that labels as $\mathcal{E}^{\mathrm{mod}}$ the doubly ionising trajectories with $\mathrm{E}^{\mathrm{mod}}$ within ± 1 eV of twice the average $\mathrm{E}^{\mathrm{mod}}$ for the one-electron problem, see Fig. 3.16(a) and (b). Therefore, in this algorithm we use the calculated $\mathrm{E}^{\mathrm{mod}}$ as input for each excess energy whereas the previously described algorithm uses only experimentally accessible data. We find that we obtain a much better agreement between the two sets of collision time using method 2, see Fig. 3.18(b). In both algorithms the collision times are computed for symmetric "modified" energy sharing. The reason we choose the symmetric energy sharing in terms of the "modified" energy is that the symmetric "modified" energy sharing is strongly correlated to the symmetric energy sharing in the absence of the IR laser field (Fig. 3.19); it is the "collision" time corresponding to this latter energy sharing that we aim to streak.

3.4.4 Charge dependence

Finally, we note that the algorithms described above for obtaining the collision time, including Eq. (3.6) and Eq. (3.12), are applicable to atoms with higher nuclear charge as well. The only difference is that the change of the "modified" electron energy with ϕ gets larger with increasing charge. This is illustrated in Fig. 3.20 for the one-electron case. For higher charges, in method 2 one would follow the exact same steps as for the case of charge equal to two described above. However, for method 1 one would need to consider a larger interval ΔE to correctly account for $\mathrm{E^{mod}}$ being steeper as a function of ϕ for larger nuclear charges.

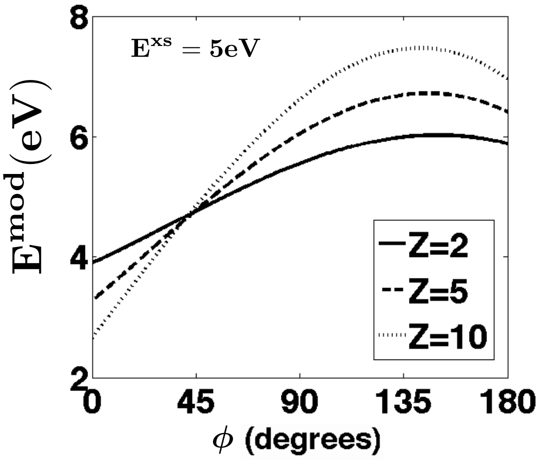

FIGURE 3.20: Average of $\mathrm{E^{mod}}$ as a function of ϕ for the one-electron case for $\mathrm{E^{xs}} = 5$ eV for charges $\mathrm{Z} = 2, 5, 10$.

3.5 Summary

We have shown that the two-electron streak camera for symmetric energy sharing "probes" roughly the "collision" time in the two-electron ionisation dynamics; for asymmetric energy sharing it "probes" the motion of the slowest electron in the presence of the ion's Coulomb potential. We have shown that the two-electron streak camera is capable of resolving the dynamics of momentum transferring attosecond collisions. Moreover, we have demonstrated that the two-electron streak camera can be realised for realistic XUV attosecond pulses.

Chapter 4

Formation of highly excited neutral atoms in strongly driven diatomics

While in the previous part of this thesis we considered single-photon ionisation processes in atoms, in what follows we study attosecond phenomena in diatomic molecules driven by intense infrared laser fields (strongly driven). Some of the phenomena that have been addressed during the breakup of strongly driven diatomics are non-sequential double ionisation (NSDI) [36] and enhanced ionisation [37]. Another very interesting process, which has only very recently being observed, is the formation of highly excited neutral atoms [38]. This process is mediated by "frustrated" ionisation, first discussed in the context of the He atom [86]: an electron tunnel ionises in the presence of the strong laser field, however, when the laser field is switched off the electron does not have enough energy to ionise and remains bound in an exited state (Rydberg state). In strongly driven H_2 the "frustrated" ionisation [38] pathway leads to the production of an excited H atom, along with a proton and a free electron.

As we discuss in what follows, "frustrated" ionisation in strongly driven H_2 accounts for about 10% of all breakup events. Thus, it is necessary to accurately describe "frustrated" ionisation, if one is to fully understand the breakup of strongly driven H_2. The theoretical modelling of "frustrated" ionisation is a highly complex task due to the large number of degrees of freedom involved. In this work, we account for both electronic and nuclear motion on the same footing, i.e. we do not use the Born-Oppenheimer approximation. Nuclear motion was not accounted for in previous semiclassical 3-d models of molecules in strong fields; these models used "fixed" centres instead to elucidate NSDI in strongly driven diatomic molecules [87–89]. The first theoretical treatment of "frustrated" ionisation in H_2 was performed in [39]. In the following we discuss how we have significantly expanded this latter work to also account for the effect of elliptically polarised laser fields on "frustrated" ionisation in H_2.

4.1 Theory and model

First, we set up the initial electronic phase space distribution. We consider the molecular axis to be along the z axis. We model the strong laser field as an electric field of the form

$$\bar{F}^L(t) = F_0^L f(t) \left[\cos(\omega_L t)\hat{z} + \varepsilon \sin(\omega_L t)\hat{x}\right], \tag{4.1}$$

where F_0^L is the electric field strength, ω_L is the angular frequency of the laser field and ε is the ellipticity of the laser pulse which can take values from 0 to 1. The function $f(t)$ is given by

$$f(t) = \begin{cases} 10T > t > 0 & 1 \\ 12T > t > 10T & \cos^2((t-2T)\omega_L/8)), \\ t > 12T & 0 \end{cases} \tag{4.2}$$

where T is the period of the laser pulse. For our simulation $\omega_L = 0.057$ a.u. (800 nm) and $F_0^L = 0.065$ a.u. (1.5×10^{14} Watts/cm^2). We start the time propagation at $\omega_L t_0 = \phi_L$, where the initial phase of the laser field ϕ_L is chosen randomly, see [89–92]. For field strengths, F_0^L, smaller than the threshold field strength for over-the-barrier ionisation, we assume that one electron (electron 1) tunnel ionises through the field-lowered Coulomb potential to the continuum, see Section 4.1.1 for details; the initially bound electron (electron 2) is described by a one-electron microcanonical distribution, see Section 4.1.3 for details. The initial conditions of the two nuclei are described by the Wigner distribution using the Morse potential [93], see Section 4.1.4 for details. We weight each trajectory using the tunnelling rate provided by the semiclassical formula

[94] with field strength equal to that at time t_0, see 4.1.5. We use 0.57 a.u. (1.28 a.u.) as the first (second) ionisation potentials.

In previous work [39], the Coulomb singularity was accounted for analytically using a global regularisation scheme formulated for gravitational systems in [95]. In the current work, we have developed a new technique that accounts for the Coulomb singularity numerically: we first transform into relative coordinates using the global regularisation scheme in [95], and then propagate numerically using a time-transformed leapfrog method [96, 97] in conjunction with the Bulirsch-Stoer method [98]. This is a much more stable technique for large mass ratio systems—electron versus nucleus in our case. More details on the propagation technique can be found in Section 4.1.7.

4.1.1 Exit point of the tunnel ionising electron

Our model starts with one electron (electron 1) tunnel-ionising through the field-lowered Coulomb barrier. We assume that the electron tunnels in a direction opposite to the field. In what follows, we determine the position of the electron at the time it exits from the field-lowered Coulomb barrier; this is also the initial position of electron 1 in the propagation. The potential electron 1 feels while it tunnel ionises is given by [88]

$$V_{exit}(r) = -\frac{Z_{n_1}}{|\bar{r}_1 - \bar{R}_{n_1}|} - \frac{Z_{n_2}}{|\bar{r}_1 - \bar{R}_{n_2}|} + k\int d^3r_2 \frac{|\psi_2(\bar{r}_2)|^2}{|\bar{r}_1 - \bar{r}_2|} + \bar{r}_1 \cdot \bar{F}^L(t_0), \tag{4.3}$$

where Z_{n_1} and Z_{n_2} are the charges of the two nuclei, while $\bar{r}_1$, $\bar{r}_2$, $\bar{R}_{n_1}$ and $\bar{R}_{n_2}$ are the position vectors of electron 1, of electron 2 and of the two nuclei, respectively. Since, we assume that the electron 1 tunnels in a direction opposite to the field it's position vector is given by $\bar{r}_1 = -r\hat{F}^L(t_0)$. $\psi_2(\bar{r}_2)$ is the wave function of the initially bound electron 2 after the removal of electron 1, i.e. the wave function of the electron in H_2^+ at the inter-nuclear equilibrium distance of H_2. Therefore, the potential term

$$k\int d^3r_2 \frac{|\psi_2(\bar{r}_2)|^2}{|\bar{r}_1 - \bar{r}_2|} \tag{4.4}$$

represents the average Coulomb repulsion between electrons 1 and 2. To find the position where electron 1 exits the barrier, we solve the following equation for r

$$V_{exit}(r) = -I_1, \tag{4.5}$$

where I_1 is the first ionisation potential. We solve Eq. (4.5) numerically to obtain r for different strengths of the field at initial times t_0, i.e. $\bar{F}^L(t_0)$.

4.1.2 Perpendicular momentum of the tunnel ionising electron at the exit point

After having determined the initial position of electron 1 we now determine its initial momentum. We assume that electron 1 tunnels with zero momentum along the direction of the field [99]. The probability distribution for the perpendicular component of the momentum [88, 100], $p_\perp$, of electron 1 is given by

$$W(p_\perp)dp_\perp = \frac{p_\perp}{F^L(t_0)} \exp\left(-\frac{p_\perp^2\sqrt{2|I_1|}}{F^L(t_0)}\right) dp_\perp. \tag{4.6}$$

The maximum value of the probability distribution is:

$$W_{max} = \frac{\exp(-1/2)}{2\sqrt{2|I_1|}F^L(t_0)}. \tag{4.7}$$

We now sample the perpendicular momentum as follows: we select a random number, $p_\perp^{test}$, uniformly distributed in the interval [0, p_{max}] where p_{max} is the value beyond which $W(p_\perp)$ is essentially zero. We, also, select a random number, W_{test}, uniformly distributed in the interval [0, W_{max}]. If $W(p_\perp^{test}) > W_{test}$, then, $p_\perp^{test}$ is accepted and assigned as the value of the perpendicular momentum, otherwise we repeat the process. Finally, the momentum of electron 1 is given by

$$\begin{aligned} p_x &= p_\perp \cos\phi_{p_\perp} \cos\theta_L \\ p_y &= p_\perp \sin\phi_{p_\perp} \\ p_z &= -p_\perp \cos\phi_{p_\perp} \sin\theta_L \end{aligned} \quad , \tag{4.8}$$

where $\phi_{p_\perp}$ is a uniform random number selected in the interval [0, 2π] and θ_L is the angle between the electric field and the molecular axis.

4.1.3 One-electron microcanonical distribution for a two centre molecule

We now focus on creating the initial conditions of electron 2, which is bound, for our formulation of the initial state. The one-electron microcanonical distribution for a two-centre molecule [101] is

$$M(\bar{r}_2,\bar{p}_2) = k\delta\left(-I_2 - p_2^2/2 - V_n(r_A,r_B)\right), \tag{4.9}$$

where

$$V_n(r_A,r_B) = -\frac{Z_{n_1}}{r_A} - \frac{Z_{n_2}}{r_B}, \tag{4.10}$$

with $r_A = |\bar{r}_2 - \bar{R}_{n_1}|$, $r_B = |\bar{r}_2 - \bar{R}_{n_2}|$, while I_2 is the second ionisation potential and $\bar{p}_2$ is the momentum of electron 2; k is a normalisation constant. We make the coordinate transformations:

$$\begin{array}{lll} \xi = \frac{1}{R_0}(r_A + r_B) & \eta = \frac{1}{R_0}(r_A - r_B) & \phi_r = \arctan(y_2/x_2) \\ \nu_p = \frac{p_{2z}}{p_2} & \phi_p = \arctan(p_{2y}/p_{2x}) & E = \frac{p_2^2}{2} - \frac{Z_{n_1}}{r_A} - \frac{Z_{n_2}}{r_B} \end{array}, \tag{4.11}$$

where ξ, η and ϕ_r denote the elliptical coordinates and $\cos\theta_p = \nu_p$, with θ_p and ϕ_p the polar and azimuthal angles in spherical coordinates. The new variables are defined in the intervals

$$\begin{array}{lll} E \in [-\infty, 0], & \xi \in [1,\infty], & \eta \in [-1,1] \\ \nu_p \in [-1,1], & \phi_p \in [0,2\pi], & \phi_r \in [0,2\pi] \end{array} \tag{4.12}$$

with the constraint that

$$\frac{p^2}{2} = -I_2 - V_n(\xi,\eta) > 0, \tag{4.13}$$

where

$$V_n(\xi,\eta) = -\frac{2Z_{n_1}}{R_0(\xi+\eta)} - \frac{2Z_{n_2}}{R_0(\xi-\eta)} \tag{4.14}$$

The Jacobian of this transformation is [101]

$$J = \left(\frac{R_0}{2}\right)^3 (\xi^2 - \eta^2)(2(E - V_n(\xi,\eta)))^{1/2}. \tag{4.15}$$

Therefore the probability density in terms of the new coordinates takes the form

$$M(E,\xi,\eta,\phi_r,\nu_p,\phi_p) = k\delta(E + I_2)\left(\frac{R_0}{2}\right)^3 (\xi^2 - \eta^2)(2(E - V_n(\xi,\eta)))^{1/2}. \tag{4.16}$$

The above probability distribution does not depend on the variables ϕ_r, ν_p and ϕ_p, and thus we assign to these variables values obtained from uniform random numbers in the intervals defined above. To determine the variables ξ and η we follow a different process. Integrating Eq. (4.16) over E, ϕ_r, ν_p and ϕ_p, we find that the probability density for these variables is given by

$$\rho(\xi,\eta) = \begin{cases} k'(\xi^2-\eta^2)\{2[-I_2 - V_n(\xi,\eta)]\}^{1/2} & \text{if} \quad -I_2 > V_n(\xi,\eta) \\ 0 & \text{if} \quad -I_2 \leq V_n(\xi,\eta) \end{cases} \tag{4.17}$$

We next discuss how we sample ξ and η [53, 101]. Let ξ_{max} be the maximum value of ξ for all η that satisfies the constraint in Eq. (4.13), while ρ_{max} is the upper bound of $\rho(\xi,\eta)$. Then, we select three random numbers ξ_{test}, η_{test} and χ_{test} uniformly distributed in the intervals [0, ξ_{max}], [-1, 1] and [0, ρ_{max}], respectively. If $\rho(\xi_{test},\eta_{test}) > \chi_{test}$ then the selected values of ξ_{test} and η_{test} are accepted. If not, three numbers are randomly selected again and the process is repeated.

4.1.4 Initial phase space distribution of the nuclei

We take the initial vibrational state of the nuclei to be the ground state of the Morse potential

$$V_M(R) = D(1-e^{-\beta(R-R_0)})^2, \tag{4.18}$$

with R the internuclear distance, $D = 0.174$ a.u., $\beta = 1.029$ a.u., and $R_0 = 1.4$ a.u. (equilibrium distance of H_2) [93]. The relative momentum of the nuclei satisfies:

$$\frac{p_{rel}^2}{2\mu} + V_M(R) = E_0, \tag{4.19}$$

where $E_0 \approx 0.01$ a.u is the vibrational ground state of the nuclei and

$$\mu = \frac{m_{n_1} m_{n_2}}{m_{n_1} + m_{n_2}}, \tag{4.20}$$

where m_{n_1} and m_{n_2} are the masses of the nuclei. We choose the Wigner distribution of the ground state of the Morse potential [93] to describe the initial phase space of the nuclei. The intensity we consider is high enough to justify restricting the initial distance of the nuclei to R_0 [102]. Concerning the relative momentum of the nuclei ,

p_{rel}, we assign to it a random number uniformly distributed in the interval [0, 10]; for values greater than 10 the Wigner distribution is essentially zero. After determining the relative momentum, we determine the momenta of the two nuclei. Following [103] the relative momentum vector is given by

$$\bar{p}_{rel} = \mu \dot{\bar{R}} \tag{4.21}$$

and the positions of the nuclei from the centre of mass are

$$\bar{R}_{n_1} = -\frac{m_{n_2}}{m_{n_1} + m_{n_2}} \bar{R} \tag{4.22}$$

and

$$\bar{R}_{n_2} = \frac{m_{n_1}}{m_{n_1} + m_{n_2}} \bar{R}. \tag{4.23}$$

Therefore the magnitude of the initial momenta of the two nuclei is given by the magnitude of the relative momentum.

Instead of the Wigner distribution we can use the classical value of the relative momentum which is given in Eq. (4.19). We find that both the Wigner and classical distributions yield the same results for the processes under consideration in this chapter.

4.1.5 Ionisation rate

For the tunnelling rate we use a semiclassical formula that was derived in [94]

$$\Gamma = 2\pi\kappa^2 C_\kappa^2 \left(\frac{2\kappa^3}{|F^L(t_0)|} \right)^{2Q/\kappa - 1} \exp\left(-\frac{2\kappa^3}{3|F^L(t_0)|} \right) R(\theta_L), \tag{4.24}$$

where $|F^L(t_0)|$ is the instantaneous field strength, $\kappa = \sqrt{2I_1}$, and Q is the asymptotic charge. For H_2 the asymptotic charge is one. The coefficient C_κ is obtained by fitting the Dyson orbital to the following asymptotic form of the wave function

$$\Psi(\bar{r}_1) \approx C_\kappa \kappa^{3/2} (r_1 \kappa)^{Q/\kappa - 1} e^{-\kappa r_1} T(\cos\theta, \sin\theta\cos\phi). \tag{4.25}$$

The Dyson orbital [104] is the overlap integral of the two-electron wave function of the molecule with the one-electron wave function of the molecular ion; for the current work the overlap integral is that of the ground state of H_2 with the 1σ state of H_2^+ calculated at the internuclear distance of H_2. We obtain both wave functions with the Hartree-Fock method [105], using MOLPRO—a standard quantum chemistry package [106].

The function $T(\cos\theta, \sin\theta\cos\phi)$ depends on the molecular orbital that the electron occupies before tunnelling. In what follows, we derive the expression for $T(\cos\theta, \sin\theta\cos\phi)$ for the H_2 molecule, where the electron occupies a $1\sigma_g$ orbital [105], which we can approximately express as a LCAO (linear combination of atomic orbitals) of two 1s orbitals

$$\Phi_{1\sigma_g}(\bar{r}_1) \propto e^{-\kappa|\bar{r}_1-\bar{R}_{n_1}|} + e^{-\kappa|\bar{r}_1-\bar{R}_{n_2}|}. \tag{4.26}$$

Taking the asymptotic expansion for $r_1 \gg R_0$, we derive an expression for $T(\cos\theta, \sin\theta\cos\phi)$

$$T(\cos\theta) = \cosh\left(\frac{\kappa R_0}{2}\cos\theta\right), \tag{4.27}$$

with R_0 the equilibrium distance between the nuclei. By fitting the wave function in the interval $3 \leq r_1 \leq 6$ a.u., we find $C_\kappa = 0.51$ for H_2. The interval was chosen so that for $r_1 > 3$ a.u., the Coulomb potential from the H_2^+ molecular ion has the form of a single-centre Coulomb potential, i.e. $-Q/r_1$, whereas the upper limit is chosen so that for $r_1 > 6$ a.u. the Dyson orbital is zero.

As discussed in [94] (shown also here for completeness), the function $R(\theta_L)$ is expressed as follows

$$\begin{aligned} R(\theta_L) &= \left[T_0(\theta_L) - \frac{4|F^L(t_0)|}{3\kappa^3}T_2(\theta_L) + \frac{2|F^L(t_0)|}{3\kappa^3}T_3(\theta_L)\right]^2 \\ &\quad + \frac{2|F^L(t_0)|}{9\kappa^3}T_1^2(\theta_L), \end{aligned} \tag{4.28}$$

where

$$
\begin{aligned}
T_0(\theta_L) &= T(\cos\theta_L, \sin\theta_L), \\
T_1(\theta_L) &= T_v \cos\theta_L - T_u \sin\theta_L, \\
T_2(\theta_L) &= T_u \cos\theta_L + T_v \sin\theta_L, \\
T_3(\theta_L) &= T_{vv} \cos^2\theta_L + T_{uu} \sin^2\theta_L - T_{uv} \sin_2\theta_L,
\end{aligned}
\tag{4.29}
$$

with T_u, T_v, T_{uu}, T_{vv}, and T_{uv} being the first and second order partial derivatives of $T(u, v)$ with respect to u and v, calculated at $u = \cos\theta_L$ and $v = \sin\theta_L$.

4.1.6 Tunnelling during time-propagation

During time-propagation, we allow the electrons to tunnel at the classical turning points along the field axis using the WKB approximation - for details see [107]. Once a classical turning point is encountered we compute at the time, t_{tp}, of the encounter:

$$
V_{tun}(r) = -\frac{Z_{n_1}}{|\bar{r}_{tun}(r) - \bar{R}_{n_1}|} - \frac{Z_{n_2}}{|\bar{r}_{tun}(r) - \bar{R}_{n_2}|} + \bar{r}_{tun} \cdot \bar{F}^L(t_{tp}) - E_{tp}, \tag{4.30}
$$

where E_{tp} is the potential energy of the electron at the turning point (ignoring the electron-electron interaction) and

$$
\bar{r}_{tun}(r) = \bar{r}_{tp} - r\hat{F}^L(t_{tp}), \tag{4.31}
$$

where $\bar{r}_{tp}$ is the position vector of the electron at the classical turning point and $\hat{F}^L(t_t)$ is the unit vector of the laser field. We next identify the roots of $V_{tun}(r)$; by definition one root is at $r = 0$, which is the turning point, while the other root r_{ex} identifies the position of the electron when it exits the potential barrier. We next compute the transmission coefficient, using the WKB formula [108]:

$$
T_{tun} = e^{-2W_{int}}, \tag{4.32}
$$

where

$$W_{int} = \int_0^{r_{ex}} \sqrt{2V_{tun}(r)}dr. \tag{4.33}$$

If T_{tun} is greater than T_{tun}^{test}, a random number uniformly distributed in [0, 1], then we consider that the electron has tunnelled; the next step of the propagation starts at $\bar{r}_{tun}(r_{ex})$ with zero momentum in the direction of tunnelling.

4.1.7 Propagation technique

Next, we describe the technique we follow to propagate the full four-body Hamiltonian in time, i.e. including both electronic and nuclear motion, in the context of N Coulomb interacting particles. Previously, in [39, 89], the equations of motion were formulated using the global regularisation scheme described in [95]. In this latter work, the resulting equations of motion were propagated using the 5th order Runge-Kutta method [98]. In the current work, we use a time-transformed leapfrog propagation technique [96] in conjunction with the Bulirsch-Stoer method [98, 109]. Combining these two techniques has been used successfully to describe gravitational few-body systems where large mass ratios are involved [96, 97, 110].

Transforming to a new coordinate system

The Hamiltonian for N Coulomb interacting particles in the presence of a laser field is given by

$$H = \sum_{i=1}^{N} \frac{p_i^2}{2m_i} + \sum_{i=1}^{N-1} \sum_{j=i+1}^{N} \frac{Q_i Q_j}{|\bar{r}_i - \bar{r}_j|} - \sum_{i=1}^{N} Q_i \bar{r}_i \cdot \bar{F}(t), \tag{4.34}$$

where Q_i is the charge, m_i is the mass, $\bar{p}_i$ is the momentum vector and $\bar{r}_i$ is the position vector of particle i and $\bar{F}(t) = (F_1(t), F_2(t), F_3(t))$ is the laser field vector. Next, we transform to a new coordinate system that involves the relative coordinate vectors $\bar{q}$ and the corresponding conjugate momenta $\bar{\rho}$, which are given by [95]

$$\bar{q}_{ij} = \bar{r}_i - \bar{r}_j, \tag{4.35}$$

$$\bar{\rho}_{ij} = \frac{1}{N}\left(\bar{p}_i - \bar{p}_j - \frac{m_i - m_j}{M} < \bar{\rho} >\right), \tag{4.36}$$

where $\langle\bar{\rho}\rangle = \sum_{i=1}^{N}\bar{p}_i$ and $M = \sum_{i=1}^{N} m_i$. Expressing $\bar{r}$ and $\bar{p}$ in terms of $\bar{q}$ and $\bar{\rho}$ we obtain

$$\bar{r}_i = \frac{1}{M}\sum_{j=i+1}^{N} m_j\bar{q}_{ij} - \frac{1}{M}\sum_{j=1}^{i-1} m_j\bar{q}_{ji} + \langle\bar{q}\rangle\,, \tag{4.37}$$

and

$$\bar{p}_i = \sum_{j=i+1}^{N}\bar{\rho}_{ij} - \sum_{j=1}^{i-1}\bar{\rho}_{ji} + \frac{m_i}{M}\langle\bar{\rho}\rangle \tag{4.38}$$

where $\langle\bar{q}\rangle = \frac{1}{M}\sum_{i=1}^{N} m_i\bar{r}_i$. Next, we define a fictitious particle for each ij pair replacing the ij with the k index as follows

$$k(i,j) = (i-1)N - i(i+1)/2 + j, \tag{4.39}$$

with $i < j$ for a total of $K = \frac{N(N-1)}{2}$ fictitious particles. Using this notation Eq. (4.38) takes the form

$$\bar{p}_i = \left[\sum_{k=1}^{K} a_{ik}\bar{\rho}_k\right] + \frac{m_i}{M} < \bar{\rho} >, \tag{4.40}$$

where $a_{ik} = 1$ and $a_{jk} = -1$ when $k = k(i,j)$, else $a_{ij} = 0$.

Expressing the Hamiltonian in Eq. (4.34) in terms of the relative coordinates and conjugate momenta we obtain

$$\begin{aligned} H &= \sum_{k,k'=1}^{K} T_{kk'}\bar{\rho}_k\bar{\rho}_{k'} + \frac{1}{2M}\langle\bar{\rho}\rangle^2 + \sum_{k=1}^{K}\frac{U_k}{q_k} \\ &- \left(\sum_{k=1}^{K} L_k\bar{q}_k + \sum_{i=1}^{N} Q_i\langle\bar{q}\rangle\right)\cdot\bar{F}(t) \end{aligned} \tag{4.41}$$

with

$$T_{kk'} = \sum_{i=1}^{N}\frac{a_{ik}a_{ik'}}{2m_i}, \quad U_k = Q_iQ_j, \quad L_k = \frac{Q_im_j - Q_jm_i}{M} \tag{4.42}$$

The equations of motion are, then, given by

$$\frac{d\bar{q}_k}{dt} = 2\sum_{k'=1}^{K} T_{kk'}\bar{\rho}_{k'} \qquad \frac{d\langle\bar{q}\rangle}{dt} = \frac{1}{M}\langle\bar{\rho}\rangle \tag{4.43}$$

$$\tag{4.44}$$

$$\frac{d\bar{\rho}_k}{dt} = \frac{U_k\bar{q}_k}{q_k^3} + LL_k\bar{F}(t) \qquad \frac{d\langle\bar{\rho}\rangle}{dt} = \sum_{i=1}^{N} Q_i\bar{F}(t) \tag{4.45}$$

Time-transformed leapfrog

For close encounters between two particles the Hamiltonian in Eq. (4.41) is singular. Previously, in [39, 89], this issue was addressed by transforming to regularised coordinates [95]. In the current work, to address the singularity, we use the time-transformed leapfrog method that is described in [96]; we can do so, since in Eq. (4.45) the derivative expressions are independent of the quantities themselves. In the leapfrog method two sets of first order differential equations are identified. In our case, these two sets correspond to the relative coordinates $\bar{q}$ and the corresponding conjugate momenta $\bar{\rho}$. In addition, we consider the time transform $ds = \Omega(\bar{q})dt$ [96]; $\Omega(\bar{q})$ is an arbitrary positive function of the relative position vectors. Introducing a new auxiliary variable $W = \Omega$ the equations of motion take the form $\bar{q}' = \dot{\bar{q}}(\bar{\rho})/W$, $t' = 1/W$ and $\bar{\rho}' = \dot{\bar{\rho}}(\bar{q})/\Omega$; prime denotes the derivate with respect to the new time variable s. To obtain W as a function of time we solve the differential equation [96]

$$\frac{dW}{dt} = \dot{\bar{q}}(\bar{\rho}) \cdot \frac{\partial \Omega(\bar{q})}{\partial \bar{q}}. \tag{4.46}$$

Applying the leapfrog method we now propagate $\bar{q}$, t, $\bar{\rho}$ and W over a time-step h as follows: (i) we propagate $\bar{q}$ and t over half a time-step, $h/2$; (ii) we propagate $\bar{\rho}$ and W over a time-step h using the values of $\bar{q}$ and t at half the time step $h/2$. For each pair of relative coordinate $\bar{q}$ and corresponding conjugate momentum $\bar{\rho}$ the time-transformed leapfrog set of equations take the form:

$$\begin{aligned}
&\bar{q}_{1/2} = \bar{q}_0 + \tfrac{h}{2}\tfrac{\dot{\bar{q}}(\bar{\rho}_0)}{W_0} \\
&t_{1/2} = t_0 + \tfrac{h}{2}\tfrac{1}{W_0} \\[2ex]
&\bar{\rho}_1 = \bar{\rho}_0 + h\tfrac{\dot{\bar{\rho}}(\bar{q}_{1/2})}{\Omega(\bar{q}_{1/2})} \\
&W_1 = W_0 + h\tfrac{\dot{\bar{q}}(\bar{\rho}_0)+\dot{\bar{q}}(\bar{\rho}_1)}{2\Omega(\bar{q}_{1/2})} \cdot \tfrac{\partial\Omega(\bar{q})}{\partial\bar{q}}\Big|_{\bar{q}=\bar{q}_{1/2}} \\[2ex]
&\bar{q}_1 = \bar{q}_0 + + \tfrac{h}{2}\tfrac{\dot{\bar{q}}(\bar{\rho}_1)}{W_1} \\
&t_1 = t_0 + \tfrac{h}{2}\tfrac{1}{W_1}
\end{aligned} \tag{4.47}$$

where the subscripts 0, 1/2, 1 denote the values of the variables at the initial time, at half a time-step and at the end of a time-step. Note that we have K such sets of equations, as many as the number of the fictitious particles. The form of Ω is chosen so that if any of the relative coordinates becomes small (two-body close encounter) then the time-step reduces accordingly:

$$\Omega = \sum_{k=1}^{K} \frac{1}{|\bar{q}_k|}. \tag{4.48}$$

Bulirsch-Stoer method

The final step in the integration of the equations of motion, involves incorporating the leapfrog method into the Bulirsch-Stoer method [98, 109]. In this latter method, the propagation over a time-step H takes place by splitting it into n time-step substeps of size $h = H/n$. For the propagation over each one of these substeps, we use the time-transformed leapfrog technique. The algorithm we follow to propagate is given by [97, 110]

$$\begin{aligned}
&\bar{q}_{1/2} = \bar{q}_0 + \tfrac{h}{2}\dot{\bar{q}}(\bar{\rho}_0)\\
&t_{1/2} = t_0 + \tfrac{h}{2}\tfrac{1}{W_0}\\
&\\
&\bar{\rho}_1 = \bar{\rho}_0 + h\tfrac{\dot{\bar{\rho}}(\bar{q}_{1/2})}{\Omega(\bar{q}_{1/2})}\\
&W_1 = W_0 + h\tfrac{\dot{\bar{q}}(\bar{\rho}_0)+\dot{\bar{q}}(\bar{\rho}_1)}{2\Omega(\bar{q}_{1/2})} \cdot \tfrac{\partial\Omega(\bar{q})}{\partial\bar{q}}\Big|_{\bar{q}=\bar{q}_{1/2}}\\
&\\
&\bar{q}_{m-1/2} = \bar{q}_{m-3/2} + h\dot{\bar{q}}(\bar{\rho}_{m-1})\\
&t_{m-1/2} = t_{m-3/2} + \tfrac{h}{2}\tfrac{1}{W_{m-1}}\\
&\vdots\\
&\bar{\rho}_m = \bar{\rho}_{m-1} + h\dot{\bar{\rho}}(\bar{q}_{m-1/2})\\
&W_m = W_{m-1} + h\tfrac{\dot{\bar{q}}(\bar{\rho}_{m-1})+\dot{\bar{q}}(\bar{\rho}_m)}{2\Omega(\bar{q}_{m-1/2})} \cdot \tfrac{\partial\Omega(\bar{q})}{\partial\bar{q}}\Big|_{\bar{q}=\bar{q}_{m-1/2}}\\
&\vdots\\
&\bar{q}_n = \bar{q}_{n-\frac{1}{2}} + \tfrac{h}{2}\dot{\bar{q}}(\bar{\rho}_n)\\
&t_n = t_{n-1/2} + \tfrac{h}{2}\tfrac{1}{W_n}
\end{aligned} \tag{4.49}$$

where $m = 2, ..., n$. This process of integrating from $\bar{q}_0$, $\bar{\rho}_0$ to $\bar{q}_n$ and $\bar{\rho}_n$ is repeated with increasing values of n until extrapolation to zero time-step, i.e. $\bar{q}_n$ and $\bar{\rho}_n$ for $n \to \infty$, is achieved with satisfactory error. Using the techniques described above we obtain results similar to those in [39] for H_2 strongly driven by linearly polarised laser fields. The current technique is numerically more robust than the one used in [39] and we, thus, adopt it in what follows.

4.1.8 Identifying Rydberg states in neutral atoms

In what follows, we adopt a CTMC method that involves all the techniques discussed in this section. We use this CTMC method to describe the formation of highly excited neutral atoms, through Coulomb explosion, in strongly driven H_2. After propagating the trajectories to the asymptotic limit we select trajectories that produce, H^+, a free electron and H^* (where $*$ denotes that the electron is in a $n > 1$ quantum state). To identify the trajectories when the electron is captured in an excited state, we first find the classical principal number $n_c = 1/\sqrt{2|\epsilon|}$, where ϵ is the total energy of the trapped electron. Next, we assign a quantum number n so that the following criterion, which is derived in [111], is satisfied:

$$[(n-1)(n-1/2)n]^{1/3} \leq n_c \leq [n(n+1/2)(n+1)]^{1/3}. \tag{4.50}$$

4.2 Results

We first describe H^* formation in strongly driven H_2 in a linearly polarised laser field along the molecular axis. In Fig. 4.1(a) we show the distribution for the quantum number n in H^* formation. The peak of the distribution is at $n = 8$, similar to results obtained for atoms [86]. In Fig. 4.1(b) we show the distribution for the energy of the H^+ and H^* fragments; the peak at around 3.5 eV is in good agreement with experimental results [38].

In Fig. 4.2, we also show the distribution for the internuclear distance when electron 2 tunnel ionises for the last time. We find that this distribution peaks at about 4 a.u. Assuming that this energy is available to just the two nuclei, in the form of potential energy, we can estimate the final kinetic energy of the nuclei due to Coulomb explosion; we find that this energy is 3.4 eV—in very good agreement with the peak value of the energy distribution in Fig. 4.1(b).

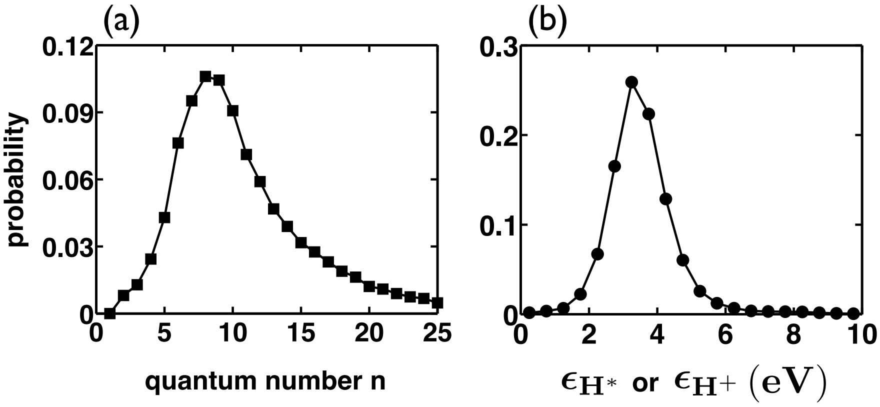

FIGURE 4.1: (a) The final energy distribution of the H^+ or H^* (b) The quantum number n of the electron in H^*.

4.2.1 Pathways for “frustrated” ionisation

We find that two distinct pathways contribute to the formation of H^*. In pathway A, the electron that initially tunnel ionises (electron 1) escapes very quickly. Later in time, the initially bound electron (electron 2) tunnel ionises and quivers in the laser field. However, when the laser field is turned off electron 2 does not have enough energy to escape. Instead, it gets trapped by one of the protons and occupies a Rydberg state of the H atom. An illustration of pathway A can be seen in Fig. 4.3(a). In pathway B, electron 1, after tunnel ionising, returns to the H_2^+ ion. After a few periods of the laser field, electron 2 tunnel ionises and escapes to the continuum. However, when the laser field is turned off electron 1 remains trapped in a Rydberg state, as illustrated in Fig. 4.3(b). For a laser field polarised along the direction of the molecule and a laser

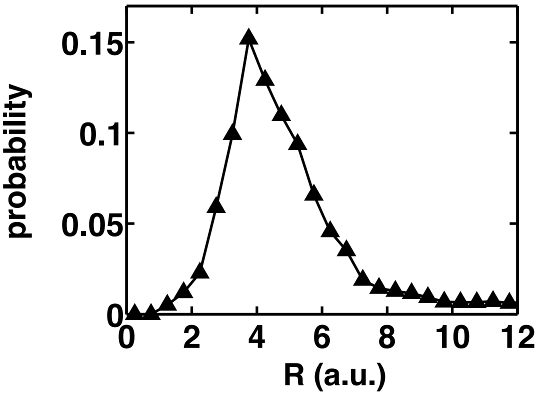

FIGURE 4.2: The internuclear distance, R, at the time the initially bound electron tunnel ionises.

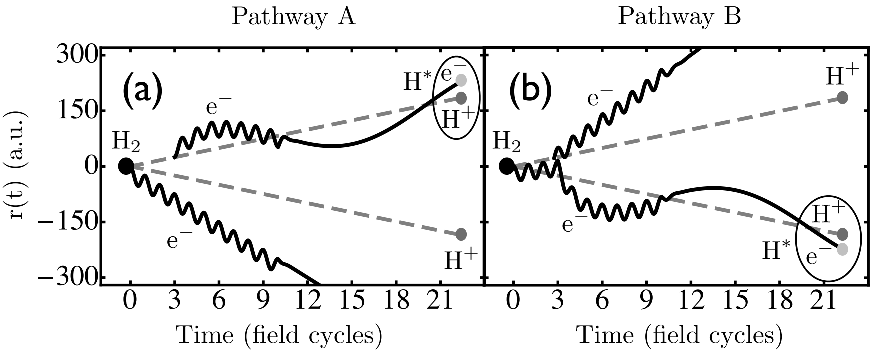

FIGURE 4.3: Illustration of the two routes in “frustrated” ionisation : (a) pathway A, (b) pathway B. Shown is the time-dependent position along the laser field for electrons (black solid lines) and nuclei (grey dashed lines)[39].

field intensity of 1.5×10^{14} Watts/cm^2, we find that the probability for pathway A and B is 3.3% and 5.4%, respectively.

The two pathways have very different momentum distributions. Fig. 4.4(a) shows the momentum distribution for pathway A, which is very confined along the z axis. On the other hand, the momentum distribution for pathway B, shown in Fig. 4.4(b), has a large spread. The reason for this difference is that in pathway B the escaping electron is the initially bound electron which interacts strongly with the nucleus before it escapes. In contrast, in pathway A the escaping electron is the initially tunnel ionising electron which escapes without returning to the molecular ion—no strong interaction with the nucleus. The momentum distribution in pathway B is therefore more spread out.

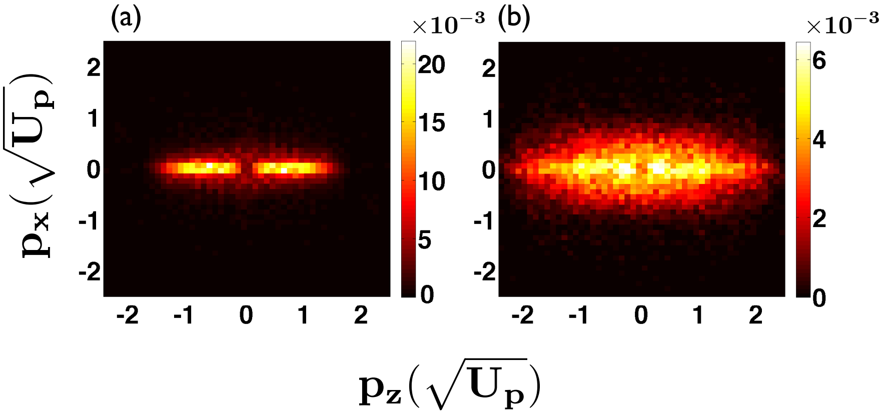

FIGURE 4.4: A 2-d (x-z plane) momentum distribution for the escaping electron (a) pathway A and (b) pathway B. The momentum is expressed in units of $\sqrt{\mathrm{U_p}}$. $\mathrm{U_p} = (F_0^L/2\omega_L)^2$.

4.3 "Frustrated" ionisation in an elliptically polarised laser field

We now study the effect of elliptically polarised laser fields on the formation of highly excited neutral fragments in strongly driven H_2. In Fig. 4.5, we show that as the ellipticity, ε, increases the probability of H^* formation decreases. Interestingly, pathway B decreases at a much faster rate than pathway A. In particular, for linear polarisation, pathway B is roughly 1.6 times more probable than pathway A. However, for ε=0.45, the probability of pathway B is 6 times smaller than that of pathway A. Thus, by increasing the ellipticity, we are affectively switching off the contribution of pathway B in "frustrated" ionisation. For ε >0.4, effectively, the only contribution to "frustrated" ionisation is from pathway A.

The natural question that follows is: why does pathway A respond so differently to increasing ellipticity compared to pathway B? First, we note that the different response, of the two pathways, to increasing ellipticity is similar to the difference observed between double ionisation due to re-collisions and enhanced ionisation of diatomic molecules. It is known that double ionisation events where re-collions prevail are sensitive to ellipticity [112]. The reason is that the ellipticity of the laser field offsets the electron from the ion by $5\varepsilon F_0^L/\omega_L^2$ [113]. We find that the dependence on ε of double ionisation events, see [112], strongly resembles the dependence on ε of our "frustrated" double ionisation

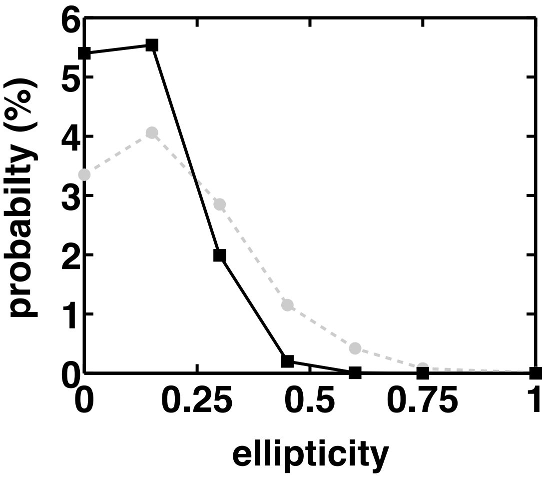

FIGURE 4.5: The probability (given in percentage) of pathway A (grey dashed circles) and pathway B (black solid squares) out of all events that occur in strongly driven H_2 as a function of the ellipticity.

events shown in Fig. 4.5. Namely, we find that double ionisation events where re-collisions/enhanced ionisation prevail change with ε in a similar way as the probability for pathway B/A does, respectively. This strongly suggests that two-electron effects in the form of re-collisions underly pathway B and not pathway A.

In what follows, we briefly explain why pathway A also decreases with increasing ellipticity of the laser field. The change in momentum, due to the laser field, of electron 2 from the time it tunnels until the end of the pulse is given by

$$\Delta\bar{p}_{tun} \approx \frac{F_0^L}{\omega_L}\left(\hat{z}\sin\phi_{tun} - \varepsilon\hat{x}\cos\phi_{tun}\right), \tag{4.51}$$

where ϕ_{tun} is the phase of the laser field when electron 2 tunnels. An electron mostly tunnels at a peak of the laser field, that is, $\phi_{tun} \approx 0^\circ$ or 180°. As a result we obtain

$$\Delta p_{tun} \approx \frac{\varepsilon F_0^L}{\omega_L}, \tag{4.52}$$

which implies that the change in momentum of electron 2 increases with increasing ellipticity. That is, electron 2 is less likely to be captured leading to increased double ionisation and decreased "frustrated" ionisation.

Evidence was provided in [39] that one-electron effects prevail in pathway A, while two-electron effects prevail in pathway B. That is, it was shown that in pathway A electron 2 transitions from the ground state of the H_2 molecule to a high Rydberg state of the H-atom by gaining energy through a strong interaction with the laser field. This gain of energy resembles enhanced ionisation in H_2^+ [114]. Evidence was also provided that in pathway B electron 2 gains energy to ionise mainly through two-electron effects resembling Delayed NSDI (non-sequential double ionisation) which is a major pathway of double electron escape (also referred to as re-collision-induced excitation with subsequent field ionisation, RESI [115, 116]). In Delayed NSDI (weak re-collision) the re-colliding electron returns to the core close to a zero of the field, transfers energy to the second electron and one electron escapes with a delay after re-collision. For pathway B the electron-electron correlation is in the form of "frustrated" delayed NSDI since one electron eventually does not escape. From the above, it follows that the dependence of the probability of pathways A and B on ε (Fig. 4.5) provides strong support that re-collisions underly pathway B.

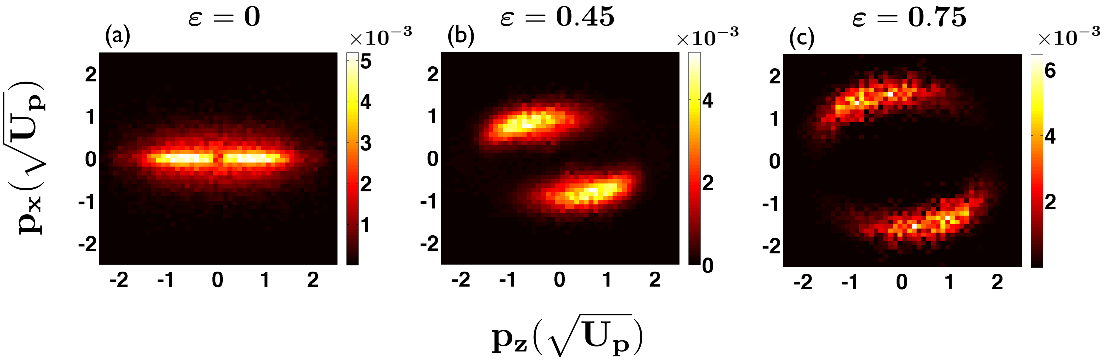

FIGURE 4.6: The total 2-d momentum distributions for different ellipticities (a) $\varepsilon = 0$, (b) $\varepsilon = 0.45$, (c) $\varepsilon = 0.75$. The distribution is the momentum of the electron in the x direction against the momentum in the z direction. The momentum is expressed in units of $\sqrt{U_p}$.

4.3.1 Momentum distribution of escaping electron

Fig. 4.5 shows that two-electron effects are essentially "switched-off" in H* formation for ε >0.4 with pathway A prevailing. This prevalence of one-electron effects with increasing ε is also evident in the observable momentum space of the escaping electron. In Fig. 4.6 we plot the total x-z momentum distribution of the escaping electron for ellipticities 0, 0.45 and 0.75, with x-z the plane of the laser field. The total 2-d distributions account for both pathways and all initial tunnelling directions of electron 1. For $\varepsilon = 0$ (Fig. 4.6(a)) the traces of both pathways A and B (Fig. 4.5) are present in the 2-d momentum distribution. The trace of pathway B is the large spread in momentum. However, for larger values of ε this large spread disappears, see Fig. 4.6(b) and (c); this is a clear signature of the prevalence of pathway A. In addition, for larger values of ε, see Fig. 4.6(b) and (c), we obtain an asymmetric two-lobe momentum distribution. This asymmetry, first observed in [117], has sparked a lot of studies in single ionisation of atoms in elliptical fields. It has been, mainly, attributed to the effect of the Coulomb potential [118]. Since our 3-d semiclassical model fully accounts for the Coulomb potential the asymmetry in the momentum distribution is also evident in our results in Fig. 4.6(b) and (c). However, besides the current study, studies of this asymmetry for molecular systems are few; they include a theoretical one of strongly driven H_2^+ [119] and an experimental one on double ionisation of H_2 [120]. Our results for H* formation in Fig. 4.6(b) and (c) show that with increasing ε the two-lobe structure tends to align closer to the minor axis of the field (x-axis in our case) [119, 120]. With one-electron effects (pathway A) prevailing for

$\varepsilon = 0.75$, the observed asymmetry is due to the Coulomb potential of the molecular ion.

4.4 Summary

In summary, we have found that with increasing ellipticity we “switch-off” two-electron effects for H^* formation and the observable momentum space of the escaping electron clearly bears the imprints of one-electron effects.

Chapter 5

Conclusions

In what follows we give a summery of how the work in this thesis has contributed towards increasing our understanding of correlated electron dynamics triggered in complex systems using novel 3-d quasiclassical techniques.

We have first addressed the correlated electron dynamics in single photon multi-electron ionization of beryllium. The breakup pattern of the escaping electrons strongly depends on correlated electron dynamics. The general expectation from Wannier's law [27] is that for excess photon energies close to the ionisation threshold the electrons escape in the most symmetric fashion. That is, for four-electron ionisation in Be, the expected breakup pattern is a regular tetrahedron. However, we have shown that, for four-electron escape from the ground state of Be ($1s^2$ $2s^2$) a triangular pyramid is the prevailing breakup pattern for excess energies as low as 3 eV above threshold; this is the case even though we accurately reproduce the Wannier exponent. In particular, roughly 65% of all quadruply ionising trajectories, give rise to a triangular pyramid pattern. Future quantum mechanical and experimental studies can verify the validity of our surprising finding. Such studies have already been performed for three-electron atoms, see for example[30, 121–123]).

We have shown that this surprising triangular pyramid is in accord with a classification scheme of a sequence of momentum transferring attosecond collisions. Each of these momentum transferring collisions takes place between the nucleus and two electrons and explains how energy is transferred from the photon electron to the other three electrons leading to quadruple ionization. We find that the two ionisation pathways that contribute the most are the ones giving rise to the triangular pyramid breakup pattern. In one of these pathways the photo-electron (1s) transfers energy to all remaining bound electrons; in the other prevailing pathway, after the 1s photo-electron transfers energy to the other 1s electron, this latter electron becomes the new impacting electron that transfers energy to the remaining two electrons. In addition, we have found that another pathway, which contributes roughly 10% to quadruple ionization, concerns the two 2s electrons each gaining energy by a different 1s electron; in this pathway the two 2s electrons are spatially apart. This ionisation route gives rise to the square planar breakup geometry predicted in [43]. Finally, one more ionisation route, which contributes roughly 10% to quadruple ionization, concerns four distinct collisions, with the two 2s electrons being spatially close. This latter ionisation route gives rise to the regular tetrahedron breakup geometry predicted in [43] and expected to prevail from Wannier's law. From previous results on triple ionisation [29] and our current work on quadruple ionisation we conjecture that four-electron breakup patterns are initial state dependent. As for three-electron escape, we have found that for four-electron escape the final breakup geometry is determined by the spatial distribution of the escaping electrons at the time when sufficient energy to ionise has been transferred through collisions to all four electrons. To better understand why the less symmetric triangular pyramid prevails over the higher symmetry regular tetrahedron, we have also analysed the non-linear properties of the fixed points of the five-body Coulomb problem. These fixed points correspond to the regular tetrahedron and square planar geometries. We have shown that the excursion from the fixed points of the hyperangles that determine the breakup patterns are expressed in terms of unstable modes. As a result, the initial values of the hyperangles are not preserved, i.e. the highest symmetry breakup geometry of the fixed point is not preserved at all times possibly resulting to final breakup geometries different than the highest symmetry ones. This was previously shown [29] to be the case, also, for three-electron ionisation in an atom.

Previous studies on Li and the work in this thesis on Be show that as the number of electrons increases the highest-symmetry breakup patterns are also present even though it is the non-highest symmetry breakup pattern that prevails. That is, for three-electron ionisation from the ground state of Li the T-shape contributes roughly 85% to triple ionisation [28]. In this work, we have shown that for quadruple ionisation from the ground state of Be the triangular pyramid contributes 65%, however, the regular tetrahedron and the triangular pyramid, which are the highest symmetry breakup patterns, contribute roughly 20%. This suggests the possibility that as the number of electrons increases the prevailing breakup patterns are more consistent with those predicted by Wannier [27]. A future study could investigate whether this is the case or not.

A current challenge in Attosecond Science is time-resolving correlated electron dynamics. In this thesis we have developed a scheme for probing the electron-electron correlation in the momentum transferring attosecond collisions that we have shown to underlie the redistribution of energy from the photo-electron to the remaining electrons in single photon multi-electron ionisation of atoms. In particular, the two-electron streak camera [33] time-resolves correlated electron dynamics during single-photon double ionisation. It does so using the asymptotic inter-electronic angle as a function of the phase delay, ϕ, between the triggering attosecond XUV-pulse (single photon) and the streaking infrared laser field.

In this thesis, we have expanded the concept of the two-electron streak-camera to time-resolve the different ionisation dynamics associated with different electron energy sharings during single-photon double ionisation in a He (1s2s) model system. Specifically, we have focused on the two extreme energy sharings, i.e. the most symmetric and the most asymmetric ones, which lead to different ionisation dynamics. The most symmetric energy sharing involves both electrons ionising soon after the collision takes place. In the case of the most asymmetric energy sharing, one electron escapes quickly after the collision, while the other electron moves under the strong influence of the nucleus before it escapes as well. This leads to this latter electron ionising with a large spread in time and a large spread in inter-electronic angles. We have shown how this different ionisation dynamics is successfully time-resolved by the two-electron streak camera. In particular, we have shown that the two-electron streak camera for symmetric energy sharing “probes” roughly the “collision” time in the two-electron ionisation dynamics, i.e. the time of minimum approach of the two electrons. Moreover, the two-electron streak camera for asymmetric energy sharing “probes” the motion of the slowest electron in the presence of the ion’s Coulomb potential. These time delays between photo-absorption and ionisation of both electrons are manifested as a shift between the maximum of the vector potential (90° for the IR laser field considered in our study) and the streaking phase corresponding to the minimum in the inter-electronic angle of escape as a function of ϕ.

Moreover, we have demonstrated that the two-electron streak camera can be experimentally realised. Instead of considering just a single-photon absorption, we have modelled a realistic attosecond pulse with a broad spread in photon energies and fully accounted for the effect of this large energy spread on time-resolving correlated electron dynamics. The problem is that while in the absence of the IR laser field the triggering photon excess energy is equal with the sum of the asymptotic energies of the escaping electrons this is no longer the case in the presence of the IR laser field. That is, in the presence of the IR laser field the sum of the asymptotic energies of the electrons corresponds to many different excess energies. We have succeed in finding a correspondence, to a good approximation, between the final energies and the triggering excess energy of the attosecond pulse by introducing the "modified" electron energy. The "modified" electron energy partially removes the effect of the IR laser field on the final energy of the electrons. We have shown that we can successfully isolate an individual photon excess energy by selecting trajectories with the corresponding "modified" energy and computing the delay time. The algorithm we have formulated to do so can be applied to atoms with different nuclear charges.

While the two-electron attosecond streak camera has been formulated for two-electron escape in atoms, it paves the way for future time-resolved studies in more complex systems. For instance, a future study could involve Li and how to time-resolve a sequence of two collisions; in this thesis we have time-resolved one collision in the context of a He (1s2s) model system. Time-resolving a sequence of two collisions is a much more challenging problem and remains to be seen what would be an appropriate asymptotic quantity that would naturally capture the correlated dynamics of the three electrons; we have shown in this work that the inter-electronic angle is an appropriate asymptotic quantity for streaking the correlated dynamics of two electrons.

Transitioning from correlated electron dynamics triggered by single-photon in atoms, in the last part of this thesis, we have addressed correlated electron dynamics in diatomic molecules driven by infrared and intense laser fields (strongly driven). This is yet another challenging problem in Attosecond Science since it involves many degrees of freedom and the coupled motion of electrons and nuclei. We have developed a novel 3-d semiclassical technique that tackles strongly-driven molecules treating the electron and nuclear dynamics at the same time while fully addressing the Coulomb singularity. This technique allowed us to offer a physical picture of the formation of highly excited neutral atoms and in particular of H^* formation during the breakup of strongly driven H_2 by elliptically polarised laser fields. We have shown that the ellipticity of the IR laser field affects the main two pathways of H^* formation in different ways. Specifically, the pathway where two-electron effects prevail decreases much faster with increasing ellipticity compared to the pathway where one-electron effects prevail. We have shown that the observable momentum space of the escaping electron clearly bears the imprints of one-electron effects with increasing ellipticity. In addition, we have identified an asymmetric lobe structure in the momentum distribution which has been attributed, in previous one electron studies in atoms, to the Coulomb potential.

The computational technique we have developed to address the Coulomb singularity and to account for both electron and nuclear motion for strongly driven diatomic molecules is a powerful one. That is, it can be used as a stepping stone for future studies of strongly driven multi-centre molecules. These studies will address the interplay of enhanced and non-sequential double ionisation during the breakup of strongly driven triatomic molecules. They will also address the interplay of different mechanisms in forming highly excited neutral atoms. Future studies could also address the effect of the intensity and of the degree of ellipticity of the laser field on the above processes.

Appendix A

Wigner distribution

The Wigner distribution [68] is defined as

$$f(\bar{r},\bar{p}) = \frac{1}{\pi^3}\int_{-\infty}^{\infty} \psi^*(|\bar{r}-\bar{z}|)\psi(|\bar{r}+\bar{z}|)\exp(2i\bar{p}\cdot\bar{z})\mathrm{d}\bar{z}, \tag{A.1}$$

where $\psi(\bar{r})$ is the quantum wave function and $\bar{r}$, $\bar{p}$ are the position and momentum vectors. The Wigner distribution has the following properties [124]:

$$\int_{-\infty}^{\infty} f(\bar{r},\bar{p})\mathrm{d}^3p = |\langle\bar{r}|\psi\rangle| \tag{A.2}$$

$$\int_{-\infty}^{\infty} f(\bar{r},\bar{p})\mathrm{d}^3r = |\langle\bar{p}|\psi\rangle|\,. \tag{A.3}$$

The Wigner distribution is computed numerically for the 1s hydrogen wave function in [125]. However, it is possible to obtain an analytical expression for the Wigner distribution by approximating the wave function as a sum of Gaussians [126, 127]. In what follows, we describe one way for expressing the hydrogenic wave function in terms of Gaussians. First, we express the wave function in terms of Slater orbitals [128, 129], which are given by

$$\Phi_{n_s,l,m}(\bar{r}) = Y_{lm}(\theta,\phi)[(2n_s)!]^{-1/2}(2\zeta)^{n_s+1/2}r^{n_s-1}\exp(-\zeta r). \tag{A.4}$$

$Y_{lm}(\theta, \phi)$ are spherical harmonics, n_s is the principal quantum number of the Slater orbital and $\zeta = Z_{eff}/n$. Z_{eff} is the effective charge and n is the principal quantum number of the hydrogenic wave function. Using Eq. (A.4), we can express the 1s and 2s wave functions in terms of Slater orbitals as follows

$$\psi_{1s}(\bar{r}) = \Phi_{100}(\bar{r}), \tag{A.5}$$

and

$$\psi_{2s}(\bar{r}) = \Phi_{100}(\bar{r}) - \sqrt{3}\Phi_{200}(\bar{r}). \tag{A.6}$$

Note that ζ is different for the Slater orbitals $\Phi_{100}(\bar{r})$ in $\psi_{1s}(\bar{r})$ and $\psi_{2s}(\bar{r})$. Next, we express the Slater orbitals as a sum of Gaussians [129]

$$\Phi_{n_s,l,m}(\bar{r}) = \sum_{j=1}^{m} c_j \chi_j(r), \tag{A.7}$$

where

$$\chi_j(\bar{r}) = Y_{lm}(\theta, \phi) \left[\frac{2^{2n_g + \frac{3}{2}}}{(2n_g - 1)!!\sqrt{\pi}} \right]^{1/2} (\alpha_j \zeta^2)^{n_g + 1/2} r^{n_g - 1} \exp(-\alpha_j \zeta^2 r^2), \tag{A.8}$$

and n_g is the number of the Gaussian, while c_j and α_j are parameters chosen to best fit the Slater orbital. It is sufficient to express $\Phi_{100}(\bar{r})$ and $\Phi_{200}(\bar{r})$ in terms of Gaussians with $n_g = 1$:

$$\chi_j(r) = \left(\frac{2\alpha_j \zeta^2}{\pi} \right)^{3/4} \exp\left(-\alpha_j \zeta^2 r^2 \right), \tag{A.9}$$

The coefficients c_i and α_i used in this work are given in Tables A.1 and A.2. Once we express the wave functions in terms of Gaussians, we substitute them into Eq. (A.1) and integrate to analytically obtain the Wigner distribution:

$$\begin{aligned} f(r,p,\eta) = & \left[\tfrac{1}{\pi^3} \textstyle\sum_{j=1}^{m} c_j^2 \exp\left(-2\alpha_j \zeta^2 r^2\right) \exp\left(-\tfrac{p^2}{2\alpha_j \zeta^2}\right) \right] + \\ & \left[\tfrac{2}{\pi^3} \textstyle\sum_{j>k=1}^{m} c_j c_k \left(\tfrac{\gamma_{jk}}{\alpha_j + \alpha_k} \right)^{3/4} \exp\left(-\gamma_{jk} \zeta^2 r^2\right) \right. \\ & \left. \times \exp\left(-\tfrac{p^2}{(\alpha_j + \alpha_k)\zeta^2} \right) \cos\left(2\tau_{jk} \cos\eta\right) \right], \end{aligned} \tag{A.10}$$

where η is the angle between the position and momentum vectors and

$$\gamma_{jk} = \frac{4\alpha_j\alpha_k}{\alpha_j + \alpha_k} \qquad \tau_{ij} = \frac{\alpha_j - \alpha_k}{\alpha_j + \alpha_k}. \tag{A.11}$$

i	c_i	α_i
1	0.107330	0.062157
2	0.339658	0.138046
3	0.352349	0.304802
4	0.213239	0.710716
5	0.090342	1.794924
6	0.030540	4.915078
7	0.008863	15.018344
8	0.002094	54.698039
9	0.000372	254.017712
10	0.000044	1776.775559

Table A.1: A list of the coefficients c_i and α_i that correspond to the orbital $\Phi_{100}(\bar{r})$, which is used to express ψ_{1s}.

i	c_i	α_i
1	0.1303340841	0.06510953954
2	0.4164915298	0.1580884151
3	0.3705627997	0.4070988982
4	01685383049	1.185056519
5	0.04936149294	4.235915534
6	0.009163596280	23.10303149
7	0.1712994697	0.04416183978
8	0.5621061301	0.09260298399
9	0.3346271174	0.2040335729
10	-0.05150303337	1.426786050
11	-0.02067024148	5.077140627
12	-0.004151277819	27.68496241

Table A.2: A list of the coefficients c_i and α_i for i varying from 1 to 6 that correspond to $\Phi_{100}(\bar{r})$, which is used to express ψ_{2s}; c_i and α_i for i varying from 7 to 12 correspond to $\Phi_{200}(\bar{r})$, which is used to express ψ_{2s}.

Appendix B

Non-linear analysis of normal modes

In what follows we show how to obtain the normal modes and eigenvalues for four electrons interacting with a nucleus. We start with the Hamiltonian of the five-body problem in 3-dimensions in cartesian coordinates:

$$h = \frac{1}{2}\sum_{i=1}^{4} P_i^2 - \sum_{i=1}^{4}\frac{Z}{r_i} + \sum_{i>j=1}^{i=4}\frac{1}{|\bar{r}_i - \bar{r}_j|} \tag{B.1}$$

where $\bar{P}_i$ and $\bar{r}_i$ are the momentum and position vectors, respectively, of the ith electron, Z is the nuclear charge and the nucleus is fixed at the origin. We wish to write the Hamiltonian in terms of hyperspherical coordinates, polar angles ξ_i and the relative azimuthal angles χ_i. The hyperspherical coordinates are given by

$$\begin{array}{ll} R = \sqrt{r_1^2 + r_2^2 + r_3^2 + r_4^2} & \alpha_1 = Arctan(\frac{r_1}{r_3}) \\ \alpha_2 = Arctan(\frac{\sqrt{r_1^2+r_3^2}}{r_4}) & \alpha_3 = Arctan(\frac{\sqrt{r_1^2+r_3^2+r_4^2}}{r_2}) \end{array}, \tag{B.2}$$

where r_i is the radial coordinate of the ith electron. The relative azimuthal angles are given by

$$\begin{array}{ll} \chi_1 = \phi_3 - \phi_1 & \chi_2 = \phi_4 - \phi_1 \\ \chi_3 = \phi_2 - \phi_1 & \chi_4 = \phi_1 + \phi_2 + \phi_3 + \phi_4 \end{array}, \tag{B.3}$$

where ϕ_i is the azimuthal angle of the ith electron. To find the conjugate momenta for the hyperspherical coordinates, the polar angles and the relative azimuthal angles we write the Lagrangian for the five-body Coulomb problem in spherical coordinates:

$$L = \frac{1}{2}\left(\sum_{i=1}^{4}\dot{r_i}^2 + \sum_{i=1}^{4} r_i^2\dot{\xi_i}^2 + \sum_{i=1}^{4} + r_i^2 \sin^2\xi_i \dot{\phi_i}^2\right) + \sum_{i=1}^{4}\frac{Z}{r_i} - \sum_{i>j=1}^{i=4}\frac{1}{|\bar{r}_i - \bar{r}_j|}, \tag{B.4}$$

where $\dot{r}_i$, $\dot{\xi}_i$ and $\dot{\phi}_i$ are the radial, polar and azimuthal velocities of the ith electron. The inter-electronic distance is given by

$$|\bar{r}_i - \bar{r}_j| = \sqrt{r_i^2 + r_j^2 - 2r_i r_j(\sin\xi_i \sin\xi_j \cos(\phi_j - \phi_i) + \cos\xi_i \cos\xi_j)}. \tag{B.5}$$

The radial coordinates expressed in terms of hyperspherical coordinates are given as

$$\begin{array}{ll} r_1 = R\sin\alpha_3 \sin\alpha_2 \sin\alpha_1 & r_3 = R\sin\alpha_3 \sin\alpha_2 \cos\alpha_1 \\ r_4 = R\sin\alpha_3 \cos\alpha_2 & r_2 = R\cos\alpha_3 \end{array}. \tag{B.6}$$

By differentiating the r_i's with respect to time in Eq. (B.6) we can obtain

$$\dot{r_1}^2 + \dot{r_2}^2 + \dot{r_3}^2 + \dot{r_4}^2 = \dot{R}^2 + R^2\dot{\alpha}_3^2 + R^2\sin^2\alpha_3\dot{\alpha}_2^2 + R^2\sin^2\alpha_3\sin^2\alpha_2\dot{\alpha}_1^2. \tag{B.7}$$

Re-arranging Eq. (B.3) we obtain the ϕ_i's in terms of χ_i's:

$$\begin{array}{ll} \phi_1 = \frac{1}{4}(\chi_4 - \chi_1 - \chi_2 - \chi_3) & \phi_2 = \frac{1}{4}(\chi_4 - \chi_1 - \chi_2 + 3\chi_3) \\ \phi_3 = \frac{1}{4}(\chi_4 + 3\chi_1 - \chi_2 - \chi_3) & \phi_4 = \frac{1}{4}(\chi_4 - \chi_1 + 3\chi_2 - \chi_3) \end{array} \tag{B.8}$$

and

$$\begin{array}{ll} \dot{\phi}_1 = \frac{1}{4}(\dot{\chi}_4 - \dot{\chi}_1 - \dot{\chi}_2 - \dot{\chi}_3) & \dot{\phi}_2 = \frac{1}{4}(\dot{\chi}_4 - \dot{\chi}_1 - \dot{\chi}_2 + 3\dot{\chi}_3) \\ \dot{\phi}_3 = \frac{1}{4}(\dot{\chi}_4 + 3\dot{\chi}_1 - \dot{\chi}_2 - \dot{\chi}_3) & \dot{\phi}_4 = \frac{1}{4}(\dot{\chi}_4 - \dot{\chi}_1 + 3\dot{\chi}_2 - \dot{\chi}_3) \end{array}. \tag{B.9}$$

Substituting Eq. (B.6), Eq. (B.7), Eq. (B.8) and Eq. (B.9) into Eq. (B.4) we obtain the Lagrangian in terms of hyperspherical coordinates, polar angles and the relative azimuthal angles:

$$
\begin{aligned}
&L = \tfrac{1}{2}\Big[\dot{R}^2 + R^2\dot{\alpha}_3^2 + R^2\sin^2\alpha_3\dot{\alpha}_2^2 + R^2\sin^2\alpha_3\sin^2\alpha_2\dot{\alpha}_1^2 \\
&+R^2\sin^2\alpha_3\sin^2\alpha_2\sin^2\alpha_1\dot{\xi}_1^2 + R^2\cos^2\alpha_3\dot{\xi}_2^2 + R^2\sin^2\alpha_3\sin^2\alpha_2\cos^2\alpha_1\dot{\xi}_3^2 + R^2\sin^2\alpha_3\cos^2\alpha_2\dot{\xi}_4^2 \\
&+R^2\sin^2\alpha_3\sin^2\alpha_2\sin^2\alpha_1\sin^2\xi_1(\dot{\chi}_4 - \dot{\chi}_1 - \dot{\chi}_2 - \dot{\chi}_3)^2/16 \\
&+R^2\cos^2\alpha_3\sin^2\xi_2(\dot{\chi}_4 - \dot{\chi}_1 - \dot{\chi}_2 + 3\dot{\chi}_3)^2/16 \\
&+R^2\sin^2\alpha_3\sin^2\alpha_2\cos^2\alpha_1\sin^2\xi_3(\dot{\chi}_4 + 3\dot{\chi}_1 - \dot{\chi}_2 - \dot{\chi}_3)^2/16 \\
&+R^2\sin^2\alpha 3\cos^2\alpha_2\sin^2\xi_4(\dot{\chi}_4 - \dot{\chi}_1 + 3\dot{\chi}_2 - \dot{\chi}_3)^2/16\Big] \\
&+Z/R\sin\alpha_3\sin\alpha_2\sin\alpha_1 + Z/R\cos\alpha_3 + Z/R\sin\alpha_3\sin\alpha_2\cos\alpha_1 + Z/R\sin\alpha_3\cos\alpha_2 \\
&-\frac{1}{R\sqrt{\sin^2\alpha_3\sin^2\alpha_2\sin^2\alpha_1+\cos^2\alpha_3-\sin 2\alpha_3\sin\alpha_2\sin\alpha_1(\sin\xi_1\sin\xi_2\cos(\chi_3)+\cos\xi_1\cos\xi_2)}} \\
&-\frac{1}{R\sin\alpha_3\sin\alpha_2\sqrt{1-\sin 2\alpha_1(\sin\xi_1\sin\xi_3\cos(\chi_1)+\cos\xi_1\cos\xi_3)}} \\
&-\frac{1}{R\sin\alpha_3\sqrt{\sin^2\alpha_2\sin^2\alpha_1+\cos^2\alpha_2-\sin 2\alpha_2\sin\alpha_1(\sin\xi_1\sin\xi_4\cos(\chi_2)+\cos\xi_1\cos\xi_4)}} \\
&-\frac{1}{R\sqrt{\cos^2\alpha_3+\sin^2\alpha_3\sin^2\alpha_2\cos^2\alpha_1-\sin 2\alpha_3\sin\alpha_2\cos\alpha_1(\sin\xi_2\sin\xi_3\cos(\chi_3-\chi_1)+\cos\xi_2\cos\xi_3)}} \\
&-\frac{1}{R\sqrt{\cos^2\alpha_3+\sin^2\alpha_3\cos^2\alpha_2-\sin 2\alpha_3\cos\alpha_2(\sin\xi_2\sin\xi_4\cos(\chi_3-\chi_2)+\cos\xi_2\cos\xi_4)}} \\
&-\frac{1}{R\sin\alpha_3\sqrt{\sin^2\alpha_2\cos^2\alpha_1+\cos^2\alpha_2-\sin 2\alpha_2\cos\alpha_1(\sin\xi_3\sin\xi_4\cos(\chi_2-\chi_1)+\cos\xi_3\cos\xi_4)}}
\end{aligned}
\quad . \tag{B.10}
$$

Using the Lagrangian given in Eq. (B.10) we obtain the conjugate momenta to the hyperspherical coordinates, the polar and the relative azimuthal angles from

$$P_{X_j} = \frac{\partial L}{\partial \dot{X}_j}, \tag{B.11}$$

where X_j is the jth competent of $\mathbf{X} = (R, \alpha_1, \alpha_2, \alpha_3, \xi_1, \xi_2, \xi_3, \xi_4, \chi_1, \chi_2, \chi_3, \chi_4)$. We can now write the Hamiltonian in terms of hyperspherical coordinates, polar angles, relative azimuthal angles and their conjugate momenta:

$$\begin{aligned}
h = {} & \tfrac{1}{2}\Big(P_R^2 + \frac{P_{\alpha_3}^2}{R^2} + \frac{P_{\alpha_2}^2}{R^2\sin^2\alpha_3} + \frac{P_{\alpha_1}^2}{R^2\sin^2\alpha_3\sin^2\alpha_2} \\
& + \frac{P_{\xi_1}^2}{R^2\sin^2\alpha_3\sin^2\alpha_2\sin^2\alpha_1} + \frac{P_{\xi_2}^2}{R^2\cos^2\alpha_3} + \frac{P_{\xi_3}^2}{R^2\sin^2\alpha_3\sin^2\alpha_2\cos^2\alpha_1} + \frac{P_{\xi_4}^2}{R^2\sin^2\alpha_3\cos^2\alpha_2} \\
& + \frac{(P_{\chi_4}-P_{\chi_1}-P_{\chi_2}-P_{\chi_3})^2}{R^2\sin^2\alpha_3\sin^2\alpha_2\sin^2\alpha_1\sin^2\xi_1} + \frac{(P_{\chi_4}+P_{\chi_3})^2}{R^2\cos^2\alpha_3\sin^2\xi_2} + \frac{(P_{\chi_4}+P_{\chi_1})^2}{R^2\sin^2\alpha_3\sin^2\alpha_2\cos^2\alpha_1\sin^2\xi_3} + \frac{(P_{\chi_4}+P_{\chi_2})^2}{R^2\sin^2\alpha3\cos^2\alpha_2\sin^2\xi_4}\Big) \\
& - \frac{Z}{R\sin\alpha_3\sin\alpha_2\sin\alpha_1} - \frac{Z}{R\cos\alpha_3} - \frac{Z}{R\sin\alpha_3\sin\alpha_2\cos\alpha_1} - \frac{Z}{R\sin\alpha_3\cos\alpha_2} \\
& + \frac{1}{R\sqrt{\sin^2\alpha_3\sin^2\alpha_2\sin^2\alpha_1+\cos^2\alpha_3-\sin 2\alpha_3\sin\alpha_2\sin\alpha_1(\sin\xi_1\sin\xi_2\cos(\chi_3)+\cos\xi_1\cos\xi_2)}} \\
& + \frac{1}{R\sin\alpha_3\sin\alpha_2\sqrt{1-\sin 2\alpha_1(\sin\xi_1\sin\xi_3\cos(\chi_1)+\cos\xi_1\cos\xi_3)}} \\
& + \frac{1}{R\sin\alpha_3\sqrt{\sin^2\alpha_2\sin^2\alpha_1+\cos^2\alpha_2-\sin 2\alpha_2\sin\alpha_1(\sin\xi_1\sin\xi_4\cos(\chi_2)+\cos\xi_1\cos\xi_4)}} \\
& + \frac{1}{R\sqrt{\cos^2\alpha_3+\sin^2\alpha_3\sin^2\alpha_2\cos^2\alpha_1-\sin 2\alpha_3\sin\alpha_2\cos\alpha_1(\sin\xi_2\sin\xi_3\cos(\chi_3-\chi_1)+\cos\xi_2\cos\xi_3)}} \\
& + \frac{1}{R\sqrt{\cos^2\alpha_3+\sin^2\alpha_3\cos^2\alpha_2-\sin 2\alpha_3\cos\alpha_2(\sin\xi_2\sin\xi_4\cos(\chi_3-\chi_2)+\cos\xi_2\cos\xi_4)}} \\
& + \frac{1}{R\sin\alpha_3\sqrt{\sin^2\alpha_2\cos^2\alpha_1+\cos^2\alpha_2-\sin 2\alpha_2\cos\alpha_1(\sin\xi_3\sin\xi_4\cos(\chi_2-\chi_1)+\cos\xi_3\cos\xi_4)}} \quad .
\end{aligned} \tag{B.12}$$

The Hamiltonian is still singular. As a first step in removing this singularity, we make the substitution of $R = w^2$ and of it's conjugate momentum $P_R = \frac{P_w}{2w}$. The resulting Hamiltonian is

$$h = \frac{P_w^2}{8w^2} + \frac{\mathbf{\Lambda^2}}{2w^4} + \frac{C(\mathbf{\Omega})}{w^2}, \tag{B.13}$$

where $\mathbf{\Lambda^2}$ and $C(\mathbf{\Omega})$ are given in Eq. (B.15) and Eq. (B.16) respectively. As a second step in removing the singularity, we introduce a new hamiltonian $H = f(h - E) = 0$, where $f = w^2$ and E is the energy of the system. The corresponding time transform is $dt = w^2 dt_w$ and the Hamiltonian takes the form

$$H = \frac{P_w^2}{8} + \frac{\mathbf{\Lambda^2}}{2w^2} + C(\mathbf{\Omega}) - w^2 E, \tag{B.14}$$

where $\mathbf{\Omega} = (\alpha_1, \alpha_2, \alpha_3, \xi_1, \xi_2, \xi_3, \xi_4, \chi_1, \chi_2, \chi_3, \chi_4)^\dagger$, which contains all the angular variables, while

$$\begin{aligned}
\mathbf{\Lambda^2} = {} & P_{\alpha_3}^2 + \frac{P_{\alpha_2}^2}{\sin^2\alpha_3} + \frac{P_{\alpha_1}^2}{\sin^2\alpha_3\sin^2\alpha_2} + \frac{P_{\xi_1}^2}{\sin^2\alpha_3\sin^2\alpha_2\sin^2\alpha_1} \\
& + \frac{P_{\xi_2}^2}{\cos^2\alpha_3} + \frac{P_{\xi_3}^2}{\sin^2\alpha_3\sin^2\alpha_2\cos^2\alpha_1} + \frac{P_{\xi_4}^2}{\sin^2\alpha_3\cos^2\alpha_2} + \frac{(P_{\chi_4}-P_{\chi_1}-P_{\chi_2}-P_{\chi_3})^2}{\sin^2\alpha_3\sin^2\alpha_2\sin^2\alpha_1\sin^2\xi_1} \\
& + \frac{(P_{\chi_4}+P_{\chi_3})^2}{\cos^2\alpha_3\sin^2\xi_2} + \frac{(P_{\chi_4}+P_{\chi_1})^2}{\sin^2\alpha_3\sin^2\alpha_2\cos^2\alpha_1\sin^2\xi_3} + \frac{(P_{\chi_4}+P_{\chi_2})^2}{\sin^2\alpha3\cos^2\alpha_2\sin^2\xi_4}
\end{aligned} \tag{B.15}$$

and

$$
\begin{aligned}
C(\mathbf{\Omega}) = &-\frac{Z}{\sin\alpha_3\sin\alpha_2\sin\alpha_1}-\frac{Z}{\cos\alpha_3}-\frac{Z}{\sin\alpha_3\sin\alpha_2\cos\alpha_1}-\frac{Z}{\sin\alpha_3\cos\alpha_2}\\
&+\frac{1}{\sqrt{\sin^2\alpha_3\sin^2\alpha_2\sin^2\alpha_1+\cos^2\alpha_3-\sin 2\alpha_3\sin\alpha_2\sin\alpha_1(\sin\xi_1\sin\xi_2\cos(\chi_3)+\cos\xi_1\cos\xi_2)}}\\
&+\frac{1}{\sin\alpha_3\sin\alpha_2\sqrt{1-\sin 2\alpha_1(\sin\xi_1\sin\xi_3\cos(\chi_1)+\cos\xi_1\cos\xi_3)}}\\
&+\frac{1}{\sin\alpha_3\sqrt{\sin^2\alpha_2\sin^2\alpha_1+\cos^2\alpha_2-\sin 2\alpha_2\sin\alpha_1(\sin\xi_1\sin\xi_4\cos(\chi_2)+\cos\xi_1\cos\xi_4)}}\\
&+\frac{1}{\sqrt{\cos^2\alpha_3+\sin^2\alpha_3\sin^2\alpha_2\cos^2\alpha_1-\sin 2\alpha_3\sin\alpha_2\cos\alpha_1(\sin\xi_2\sin\xi_3\cos(\chi_3-\chi_1)+\cos\xi_2\cos\xi_3)}}\\
&+\frac{1}{\sqrt{\cos^2\alpha_3+\sin^2\alpha_3\cos^2\alpha_2-\sin 2\alpha_3\cos\alpha_2(\sin\xi_2\sin\xi_4\cos(\chi_3-\chi_2)+\cos\xi_2\cos\xi_4)}}\\
&+\frac{1}{\sin\alpha_3\sqrt{\sin^2\alpha_2\cos^2\alpha_1+\cos^2\alpha_2-\sin 2\alpha_2\cos\alpha_1(\sin\xi_3\sin\xi_4\cos(\chi_2-\chi_1)+\cos\xi_3\cos\xi_4)}}
\end{aligned}
\tag{B.16}
$$

The equations of motion for the above Hamiltonian are given as follows:

$$
\begin{aligned}
\frac{dw}{dt_w} &= \frac{\partial H}{\partial P_w} = \frac{P_w}{4}\\
\frac{dP_w}{dt_w} &= -\frac{\partial H}{\partial w} = \frac{1}{w^3}\mathbf{\Lambda^2} + 2wE\\
\frac{d\alpha_1}{dt_w} &= \frac{\partial H}{\partial P_{\alpha_1}} = \frac{1}{w^2}\frac{P_{\alpha_1}}{\sin^2\alpha_3\sin^2\alpha_2}\\
\frac{dP_{\alpha_1}}{dt_w} &= -\frac{\partial H}{\partial \alpha_1} = -\frac{1}{2w^2}\frac{\partial\mathbf{\Lambda^2}}{\partial\alpha_1} - \frac{\partial C}{\partial\alpha_1}\\
\frac{d\alpha_2}{dt_w} &= \frac{\partial H}{\partial P_{\alpha_2}} = \frac{1}{w^2}\frac{P_{\alpha_2}}{\sin^2\alpha_3}\\
\frac{dP_{\alpha_2}}{dt_w} &= -\frac{\partial H}{\partial \alpha_2} = -\frac{1}{2w^2}\frac{\partial\mathbf{\Lambda^2}}{\partial\alpha_2} - \frac{\partial C}{\partial\alpha_2}\\
\frac{d\alpha_3}{dt_w} &= \frac{\partial H}{\partial P_{\alpha_3}} = \frac{1}{w^2}P_{\alpha_3}\\
\frac{dP_{\alpha_3}}{dt_w} &= -\frac{\partial H}{\partial \alpha_3} = -\frac{1}{2w^2}\frac{\partial\mathbf{\Lambda^2}}{\partial\alpha_3} - \frac{\partial C}{\partial\alpha_3}\\
\frac{d\xi_1}{dt_w} &= \frac{\partial H}{\partial P_{\xi_1}} = \frac{1}{w^2}\frac{P_{\xi_1}}{\sin^2\alpha_3\sin^2\alpha_2\sin^2\alpha_1}\\
\frac{dP_{\xi_1}}{dt_w} &= -\frac{\partial H}{\partial \xi_1} = -\frac{1}{2w^2}\frac{\partial\mathbf{\Lambda^2}}{\partial\xi_1} - \frac{\partial C}{\partial\xi_1}\\
\frac{d\xi_2}{dt_w} &= \frac{\partial H}{\partial P_{\xi_2}} = \frac{1}{w^2}\frac{P_{\xi_2}}{\cos^2\alpha_3}\\
\frac{dP_{\xi_2}}{dt_w} &= -\frac{\partial H}{\partial \xi_2} = -\frac{1}{2w^2}\frac{\partial\mathbf{\Lambda^2}}{\partial\xi_2} - \frac{\partial C}{\partial\xi_2}\\
\frac{d\xi_3}{dt_w} &= \frac{\partial H}{\partial P_{\xi_3}} = \frac{1}{w^2}\frac{P_{\xi_3}}{\sin^2\alpha_3\sin^2\alpha_2\cos^2\alpha_1}\\
\frac{dP_{\xi_3}}{dt_w} &= -\frac{\partial H}{\partial \xi_3} = -\frac{1}{2w^2}\frac{\partial\mathbf{\Lambda^2}}{\partial\xi_3} - \frac{\partial C}{\partial\xi_3}
\end{aligned}
\tag{B.17}
$$

$$
\begin{aligned}
&\frac{d\xi_4}{dt_w} = \frac{\partial H}{\partial P_{\xi_4}} = \frac{1}{w^2}\frac{P_{\xi_4}}{\sin^2\alpha_3\cos^2\alpha_2}\\
&\frac{dP_{\xi_4}}{dt_w} = -\frac{\partial H}{\partial \xi_4} = -\frac{1}{2w^2}\frac{\partial \mathbf{\Lambda^2}}{\partial \xi_4} - \frac{\partial C}{\partial \xi_4}\\
&\frac{d\chi_1}{dt_w} = \frac{1}{w^2}\Big(\frac{-(P_{\chi_4}-P_{\chi_1}-P_{\chi_2}-P_{\chi_3})}{\sin^2\alpha_3\sin^2\alpha_2\sin^2\alpha_1\sin^2\xi_1} + \frac{(P_{\chi_4}+P_{\chi_1})}{\sin^2\alpha_3\sin^2\alpha_2\cos^2\alpha_1\sin^2\xi_3}\Big)\\
&\frac{dP_{\chi_1}}{dt_w} = -\frac{\partial C}{\partial \chi_1}\\
&\frac{d\chi_2}{dt_w} = \frac{1}{w^2}\Big(\frac{-(P_{\chi_4}-P_{\chi_1}-P_{\chi_2}-P_{\chi_3})}{\sin^2\alpha_3\sin^2\alpha_2\sin^2\alpha_1\sin^2\xi_1} + \frac{(P_{\chi_4}+P_{\chi_2})}{\sin^2\alpha 3\cos^2\alpha_2\sin^2\xi_4}\Big)\\
&\frac{dP_{\chi_2}}{dt_w} = -\frac{\partial C}{\partial \chi_2} \qquad\qquad (B.18)\\
&\frac{d\chi_3}{dt_w} = \frac{1}{w^2}\Big(\frac{-(P_{\chi_4}-P_{\chi_1}-P_{\chi_2}-P_{\chi_3})}{\sin^2\alpha_3\sin^2\alpha_2\sin^2\alpha_1\sin^2\xi_1} + \frac{(P_{\chi_4}+P_{\chi_3})}{\cos^2\alpha_3\sin^2\xi_2}\Big)\\
&\frac{dP_{\chi_3}}{dt_w} = -\frac{\partial C}{\partial \chi_3}\\
&\frac{d\chi_4}{dt_w} = \frac{1}{w^2}\Big(\frac{(P_{\chi_4}-P_{\chi_1}-P_{\chi_2}-P_{\chi_3})}{\sin^2\alpha_3\sin^2\alpha_2\sin^2\alpha_1\sin^2\xi_1} + \frac{(P_{\chi_4}+P_{\chi_3})}{\cos^2\alpha_3\sin^2\xi_2} +\\
&\frac{(P_{\chi_4}+P_{\chi_1})}{\sin^2\alpha_3\sin^2\alpha_2\cos^2\alpha_1\sin^2\xi_3} + \frac{(P_{\chi_4}+P_{\chi_2})}{\sin^2\alpha 3\cos^2\alpha_2\sin^2\xi_4}\Big)\\
&\frac{dP_{\chi_4}}{dt_w} = 0
\end{aligned}
$$

However, the equations of motion are still singular at the fixed point $w^* = 0$. As a third step to remove the singularity, we make a new transformation of the momentum variables $\mathbf{P_\Omega}$ which are conjugate to $\mathbf{\Omega}$:

$$p_{\Omega_j} = P_{\Omega_j}/w \qquad (B.19)$$

where Ω_j represents the jth component of the $\mathbf{\Omega}$ vector. As a result

$$\mathbf{\Lambda^2}(\mathbf{P_\Omega}) = w^2\mathbf{\Lambda^{2\prime}}(\mathbf{p_\Omega}) \qquad (B.20)$$

Therefore the new Hamiltonian is given by

$$\tilde{H} = \frac{P_w^2}{8} + \frac{\mathbf{\Lambda^{2\prime}}}{2} + C(\mathbf{\Omega}) - w^2E. \qquad (B.21)$$

As a fourth step in removing the singularity, we make the time transform $dt = w^2dt_w = w^3d\tau$ resulting in $\frac{d}{d\tau} = w\frac{d}{dt_w}$. In order to write the equations of motion in terms of the new time τ we simply multiple the equations of motion for the position coordinates by

w. To find the equations of motion of the new non-canonical momenta we use

$$\frac{d}{dt_w}(P_{w_j}) = \frac{d}{dt_w}(\frac{wP_{w_j}}{w}) = w\frac{d}{dt_w}(\frac{P_{w_j}}{w}) + \frac{P_{w_j}}{w}\frac{d}{dt_w}(w) = \frac{d}{d\tau}(p_{w_j}) + \frac{P_w p_{w_j}}{4}, \tag{B.22}$$

i.e.

$$\frac{d}{d\tau}(p_{w_j}) = \frac{dP_{w_j}}{dt_w} - \frac{P_w p_{w_j}}{4}. \tag{B.23}$$

Our new equations of motion are given by

$$\begin{aligned}
\frac{dw}{d\tau} &= \frac{wP_w}{4} \\
\frac{dP_w}{d\tau} &= \mathbf{\Lambda^{2\prime}} + 2w^2 E \\
\frac{d\alpha_1}{d\tau} &= \frac{p_{\alpha_1}}{\sin^2\alpha_3 \sin^2\alpha_2} \\
\frac{dp_{\alpha_1}}{d\tau} &= -\frac{1}{2}\frac{\partial \mathbf{\Lambda^{2\prime}}}{\partial \alpha_1} - \frac{\partial C}{\partial \alpha_1} - \frac{P_w p_{\alpha_1}}{4} \\
\frac{d\alpha_2}{d\tau} &= \frac{p_{\alpha_2}}{\sin^2\alpha_3} \\
\frac{dp_{\alpha_2}}{d\tau} &= -\frac{1}{2}\frac{\partial \mathbf{\Lambda^{2\prime}}}{\partial \alpha_2} - \frac{\partial C}{\partial \alpha_2} - \frac{P_w p_{\alpha_2}}{4} \\
\frac{d\alpha_3}{d\tau} &= p_{\alpha_3} \\
\frac{dp_{\alpha_3}}{d\tau} &= -\frac{1}{2}\frac{\partial \mathbf{\Lambda^{2\prime}}}{\partial \alpha_3} - \frac{\partial C}{\partial \alpha_3} - \frac{P_w p_{\alpha_3}}{4} \\
\frac{d\xi_1}{d\tau} &= \frac{p_{\xi_1}}{\sin^2\alpha_3 \sin^2\alpha_2 \sin^2\alpha_1} \\
\frac{dp_{\xi_1}}{d\tau} &= -\frac{1}{2}\frac{\partial \mathbf{\Lambda^{2\prime}}}{\partial \xi_1} - \frac{\partial C}{\partial \xi_1} - \frac{P_w p_{\xi_1}}{4} \\
\frac{d\xi_2}{d\tau} &= \frac{p_{\xi_2}}{\cos^2\alpha_3} \\
\frac{dp_{\xi_2}}{d\tau} &= -\frac{1}{2}\frac{\partial \mathbf{\Lambda^{2\prime}}}{\partial \xi_2} - \frac{\partial C}{\partial \xi_2} - \frac{P_w p_{\xi_2}}{4} \\
\frac{d\xi_3}{d\tau} &= \frac{p_{\xi_3}}{\sin^2\alpha_3 \sin^2\alpha_2 \cos^2\alpha_1} \\
\frac{dp_{\xi_3}}{d\tau} &= -\frac{1}{2}\frac{\partial \mathbf{\Lambda^{2\prime}}}{\partial \xi_3} - \frac{\partial C}{\partial \xi_3} - \frac{P_w p_{\xi_3}}{4} \\
\frac{d\xi_4}{d\tau} &= \frac{p_{\xi_4}}{\sin^2\alpha_3 \cos^2\alpha_2} \\
\frac{dp_{\xi_4}}{d\tau} &= -\frac{1}{2}\frac{\partial \mathbf{\Lambda^{2\prime}}}{\partial \xi_4} - \frac{\partial C}{\partial \xi_4} - \frac{P_w p_{\xi_4}}{4}
\end{aligned} \tag{B.24}$$

$$
\begin{aligned}
\frac{d\chi_1}{d\tau} &= \frac{-(p_{\chi_4}-p_{\chi_1}-p_{\chi_2}-p_{\chi_3})}{\sin^2\alpha_3\sin^2\alpha_2\sin^2\alpha_1\sin^2\xi_1} + \frac{(p_{\chi_4}+p_{\chi_1})}{\sin^2\alpha_3\sin^2\alpha_2\cos^2\alpha_1\sin^2\xi_3} \\
\frac{dp_{\chi_1}}{d\tau} &= -\frac{\partial C}{\partial\chi_1} - \frac{P_w p_{\chi_1}}{4} \\
\frac{d\chi_2}{d\tau} &= \frac{-(p_{\chi_4}-p_{\chi_1}-p_{\chi_2}-p_{\chi_3})}{\sin^2\alpha_3\sin^2\alpha_2\sin^2\alpha_1\sin^2\xi_1} + \frac{(p_{\chi_4}+p_{\chi_2})}{\sin^2\alpha_3\cos^2\alpha_2\sin^2\xi_4} \\
\frac{dp_{\chi_2}}{d\tau} &= -\frac{\partial C}{\partial\chi_2} - \frac{P_w p_{\chi_2}}{4} \\
\frac{d\chi_3}{d\tau} &= \frac{-(p_{\chi_4}-p_{\chi_1}-p_{\chi_2}-p_{\chi_3})}{\sin^2\alpha_3\sin^2\alpha_2\sin^2\alpha_1\sin^2\xi_1} + \frac{(p_{\chi_4}+p_{\chi_3})}{\cos^2\alpha_3\sin^2\xi_2} \\
\frac{dp_{\chi_3}}{d\tau} &= -\frac{\partial C}{\partial\chi_3} - \frac{P_w p_{\chi_3}}{4} \\
\frac{d\chi_4}{d\tau} &= \frac{(p_{\chi_4}-p_{\chi_1}-p_{\chi_2}-p_{\chi_3})}{\sin^2\alpha_3\sin^2\alpha_2\sin^2\alpha_1\sin^2\xi_1} + \frac{(p_{\chi_4}+p_{\chi_3})}{\cos^2\alpha_3\sin^2\xi_2} + \\
&\frac{(p_{\chi_4}+p_{\chi_1})}{\sin^2\alpha_3\sin^2\alpha_2\cos^2\alpha_1\sin^2\xi_3} + \frac{(p_{\chi_4}+p_{\chi_2})}{\sin^2\alpha 3\cos^2\alpha_2\sin^2\xi_4} \\
\frac{dp_{\chi_4}}{d\tau} &= -\frac{P_w p_{\chi_4}}{4}
\end{aligned}
\tag{B.25}
$$

The fixed points of the five-body system correspond to the values of the coordinates and momenta that result in the right hand side of the equations of motion in Eq. (B.24) and Eq. (B.25) being zero, i.e., the system does not evolve in time. By inspection of Eq. (B.24) and Eq. (B.25) we find that $w^* = p^*_{\Omega_j} = 0$ at the fixed points. The values of the angular coordinates at the fixed points are obtained by

$$\nabla_{\mathbf{\Omega}} C(\mathbf{\Omega})|_{\mathbf{\Omega}=\mathbf{\Omega}^*} = \mathbf{0}. \tag{B.26}$$

Since $\mathbf{\Lambda}^{\mathbf{2}'}$ and w are zero at the fixed point and $\tilde{H} = \frac{P_w^2}{8} + \frac{\mathbf{\Lambda}^{\mathbf{2}'}}{2} + C(\mathbf{\Omega}) - w^2 E = 0$ it follows that $P_w^* = \sqrt{-8C(\mathbf{\Omega}^*)}$. We next linearise the equations of motion around the fixed points. We denote the displacement of the $\boldsymbol{\gamma}$ vector, where $\boldsymbol{\gamma} = (P_w, \mathbf{p}_{\mathbf{\Omega}}, w, \mathbf{\Omega})^\dagger$, from the fixed point $\boldsymbol{\gamma}^*$ by

$$\delta\boldsymbol{\gamma} = \boldsymbol{\gamma} - \boldsymbol{\gamma}^*. \tag{B.27}$$

Then the linearised equations of motion take the form

$$\frac{d\delta\boldsymbol{\gamma}}{d\tau} = M \cdot \delta\boldsymbol{\gamma} \tag{B.28}$$

where

$$M = \begin{pmatrix} \frac{\partial}{\partial\gamma_1}\cdot\frac{d\gamma_1}{d\tau} & \frac{\partial}{\partial\gamma_2}\cdot\frac{d\gamma_1}{d\tau} & \cdots & \frac{\partial}{\partial\gamma_n}\cdot\frac{d\gamma_1}{d\tau} \\ \frac{\partial}{\partial\gamma_1}\cdot\frac{d\gamma_2}{d\tau} & \frac{\partial}{\partial\gamma_2}\cdot\frac{d\gamma_2}{d\tau} & \cdots & \frac{\partial}{\partial\gamma_n}\cdot\frac{d\gamma_2}{d\tau} \\ \vdots & \vdots & \ddots & \vdots \\ \frac{\partial}{\partial\gamma_1}\cdot\frac{d\gamma_n}{d\tau} & \frac{\partial}{\partial\gamma_2}\cdot\frac{d\gamma_n}{d\tau} & \cdots & \frac{\partial}{\partial\gamma_n}\cdot\frac{d\gamma_n}{d\tau} \end{pmatrix} \tag{B.29}$$

and all elements of matrix M are evaluated at $\boldsymbol{\gamma} = \boldsymbol{\gamma}^*$; γ_j denotes the jth component of $\boldsymbol{\gamma}$. The eigenvalues and eigenvectors of M are the Liapunov exponents and the normal modes of the five-body Coulomb problem.

Appendix C

Transition probability by photo-absorption from an attosecond XUV-pulse

We model the attosecond XUV-pulse as a cosine electric field with a Gaussian envelope given by

$$\bar{F}(t) = \hat{\epsilon} F_0 \exp(-t^2/4\sigma^2) \cos(\omega_0 t), \tag{C.1}$$

where σ is the standard deviation of the temporal-intensity envelope of the pulse, while F_0 and ω_0 are the strength and the angular frequency of the electric field, respectively; $\hat{\epsilon}$ is the polarisation vector. Note that, instead of the notation F_0^{XUV} and ω_0^{XUV}, used in Section 3.4.1, in what follows, for convenience, we adopt the notation F_0 and ω_0. The spectral distribution of the electric field is given by the Fourier transform of the temporal distribution of the electric field [82]:

$$\tilde{F}(\omega) = \int_{-\infty}^{\infty} F(t) \exp(-i\omega t) dt. \tag{C.2}$$

We find that $\tilde{F}(\omega)$, for frequencies greater than zero, is given by

$$\tilde{F}^{+}(\omega) = F_0 \sigma \sqrt{\pi} \exp(-(\omega - \omega_0)^2 \sigma^2). \tag{C.3}$$

The spectral intensity is given by [82]

$$\tilde{I}(\omega) = \frac{1}{4\pi^2} c \left| \tilde{F}^{+}(\omega) \right|^2, \tag{C.4}$$

and by combining Eq. (C.3) and Eq. (C.4) we obtain

$$\tilde{I}(\omega) = \frac{1}{4\pi} c F_0^2 \sigma^2 \exp(-2(\omega - \omega_0)^2 \sigma^2). \tag{C.5}$$

The probability to transition from an initial state i to a final state f, due to the absorption of a single photon, can be expressed as $W_{i\to f} = W_{i\to f}^{abs} P^{++}(\omega)$. $P^{++}(\omega)$, which we computed by using CTMC, is the double ionisation probability following the absorption of a single photon ω. In what follows we describe how to obtain $W_{i\to f}^{abs}$.

We assume that the electric field of the pulse is weak compared to the Coulomb forces, since the electron absorbs the photon at the nucleus. Therefore, using first order perturbation theory [84], we obtain

$$W_{i\to f}^{abs} = \left| \int_{-\infty}^{t} \langle f \left| V(t') \right| i \rangle \exp(i\omega t') dt' \right|^2, \tag{C.6}$$

where

$$V(t') = \hat{\epsilon} \cdot \bar{r} F_0 \exp(-t^2/4\sigma^2) \cos(\omega_0 t'). \tag{C.7}$$

Substituting Eq. (C.7) in Eq. (C.6) we obtain

$$W_{i\to f}^{abs} = \frac{F_0^2}{4} \left| \langle f \left| \hat{\epsilon} \cdot \bar{r} \right| i \rangle \right|^2 \exp(-2(\omega - \omega_0)^2 \sigma^2)) \left| \int_{-\infty}^{t} \exp(-[t' - 2i(\omega - \omega_0)\sigma^2]^2/4\sigma^2 dt' \right|^2. \tag{C.8}$$

Using the definition of the “error function” [130] ($erf(x)$):

$$\int_{-\infty}^{t} \exp(-[t' - 2i(\omega - \omega_0)\sigma^2]^2/4\sigma^2 dt' = \sigma\sqrt{\pi} \left[1 + erf\left(\frac{t}{2\sigma} - i(\omega - \omega_0)\sigma \right) \right], \tag{C.9}$$

we obtain

$$W_{i\to f}^{abs} = \frac{F_0^2 \sigma^2 \pi}{4} \left| \langle f \left| \hat{\epsilon} \cdot \bar{r} \right| i \rangle \right|^2 \exp(-2(\omega - \omega_0)^2 \sigma^2)) \left| 1 + erf\left(\frac{t}{2\sigma} - i(\omega - \omega_0)\sigma \right) \right|^2. \tag{C.10}$$

Substituting the spectral intensity given by Eq. (C.5) in Eq. (C.10) and using that the fine structure constant $\alpha = \frac{1}{c}$ in atomic units we obtain

$$W_{i\to f}^{abs} = \pi^2\alpha \left|\langle f \left|\hat{\epsilon}\cdot\bar{r}\right| i\rangle\right|^2 \tilde{I}(\omega) \left|1 + erf\left(\frac{t}{2\sigma} - i(\omega-\omega_0)\sigma\right)\right|^2. \tag{C.11}$$

For small values of σ, $erf\left(\frac{t}{2\sigma} - i(\omega_{fi}-\omega_0)\sigma\right) \to 1$; we substitute into Eq. (C.11) to obtain

$$W_{i\to f}^{abs} = 4\pi^2\alpha \left|\langle f \left|\hat{\epsilon}\cdot\vec{r}\right| i\rangle\right|^2 \tilde{I}(\omega). \tag{C.12}$$

Using that the photo-absorption cross section is given by [131]

$$\sigma_{abs}(\omega) = 4\pi^2\alpha\omega \left|\langle f \left|\hat{\epsilon}\cdot\vec{r}\right| i\rangle\right|^2, \tag{C.13}$$

we finally obtain

$$W_{i\to f}^{abs} = \frac{1}{\omega}\sigma_{abs}(\omega)\tilde{I}(\omega). \tag{C.14}$$

Note, that the photo-absorption cross section for a single electron, $\sigma_{abs}(\omega)$, in an initial state given by the 1s hydrogenic wave function [85] is

$$\sigma_{abs}(\omega) = \frac{32\pi^2\alpha}{3}\frac{Z^6}{\omega^4}\frac{\exp(-4n' arccot(n'))}{1-\exp(-2\pi n')}, \tag{C.15}$$

with

$$n' = \frac{Z}{\sqrt{2\omega - Z^2}}, \tag{C.16}$$

where Z the nulear charge.

Bibliography

[1] M. Nisoli and G. Sansone. New frontiers in attosecond science. *Progress in Quantum Electronics*, 33(1):17–59, 2009.

[2] H. A. Haus. Mode-locking of lasers. *Ieee Journal of Selected Topics in Quantum Electronics*, 6(6):1173–1185, 2000.

[3] W. T. Silfvast. *Laser Fundamentals.* Cambridge University Press, 2004.

[4] A. McPherson, G. Gibson, H. Jara, U. Johann, T. S. Luk, I. A. McIntyre, K. Boyer, and C. K. Rhodes. Studies of multiphoton production of vacuum ultraviolet-radiation in the rare-gases. *Journal of the Optical Society of America B-Optical Physics*, 4(4):595–601, 1987.

[5] M. Ferray, A. Lhuillier, X. F. Li, L. A. Lompre, G. Mainfray, and C. Manus. Multiple-harmonic conversion of 1064-nm radiation in rare-gases. *Journal of Physics B-Atomic Molecular and Optical Physics*, 21(3):L31–L35, 1988.

[6] K. Midorikawa. High-Order Harmonic Generation and Attosecond Science. *Japanese Journal of Applied Physics*, 50(9):090001, 2011.

[7] M. F. Kling and M. J. J. Vrakking. Attosecond electron dynamics. *Annual Review of Physical Chemistry*, 59:463–492, 2008.

[8] F. Krausz and M. Ivanov. Attosecond physics. *Reviews of Modern Physics*, 81(1): 163–234, 2009.

[9] P. B. Corkum and F. Krausz. Attosecond science. *Nature Physics*, 3(6):381, 2007.

[10] M. Hentschel, R. Kienberger, C. Spielmann, G. A. Reider, N. Milosevic, T. Brabec, P. Corkum, U. Heinzmann, M. Drescher, and F. Krausz. Attosecond metrology. *Nature*, 414(6863):509–513, 2001.

[11] P. M. Paul, E. S. Toma, P. Breger, G. Mullot, F. Auge, P. Balcou, H. G. Muller, and P. Agostini. Observation of a train of attosecond pulses from high harmonic generation. *Science*, 292(5522):1689–1692, 2001.

[12] P. B. Corkum. Plasma perspective on strong-field multiphoton ionization. *Nature Physics*, 71(13):1994–1997, 1993.

[13] K. Zhao, Q. Zhang, M. Chini, Y. Wu, X. W. Wang, and Z. H. Chang. Tailoring a 67 attosecond pulse through advantageous phase-mismatch. *Optics Letters*, 37 (18):3891–3893, 2012.

[14] G. Sansone, E. Benedetti, F. Calegari, C. Vozzi, L. Avaldi, R. Flammini, L. Poletto, P. Villoresi, C. Altucci, R. Velotta, S. Stagira, S. De Silvestri, and M. Nisoli. Isolated single-cycle attosecond pulses. *Science*, 314(5798):443–446, 2006.

[15] E. Goulielmakis, M. Schultze, M. Hofstetter, V. S. Yakovlev, J. Gagnon, M. Uiberacker, A. L. Aquila, E. M. Gullikson, D. T. Attwood, R. Kienberger, F. Krausz, and U. Kleineberg. Single-cycle nonlinear optics. *Science*, 320(5883):1614–1617, 2008.

[16] T. Popmintchev, M. C. Chen, P. Arpin, M. M. Murnane, and H. C. Kapteyn. The attosecond nonlinear optics of bright coherent X-ray generation. *Nature Photonics*, 4(12):822–832, 2010.

[17] J. Itatani, F. Quere, G. L. Yudin, M. Y. Ivanov, F. Krausz, and P. B. Corkum. Attosecond streak camera. *Physical Review Letters*, 88(17):173903, 2002.

[18] M. Drescher, M. Hentschel, R. Kienberger, G. Tempea, C. Spielmann, G. A. Reider, P. B. Corkum, and F. Krausz. X-ray pulses approaching the attosecond frontier. *Science*, 291(5510):1923–1927, 2001.

[19] M. Drescher, M. Hentschel, R. Kienberger, M. Uiberacker, V. Yakovlev, A. Scrinzi, T. Westerwalbesloh, U. Kleineberg, U. Heinzmann, and F. Krausz. Time-resolved atomic inner-shell spectroscopy. *Nature*, 419(6909):803–807, 2002.

[20] A. L. Cavalieri, N. Muller, T. Uphues, V. S. Yakovlev, A. Baltuska, B. Horvath, B. Schmidt, L. Blumel, R. Holzwarth, S. Hendel, M. Drescher, U. Kleineberg, P. M. Echenique, R. Kienberger, F. Krausz, and U. Heinzmann. Attosecond spectroscopy in condensed matter. *Nature*, 449(7165):1029–1032, 2007.

[21] M. Schultze, M. Fiess, N. Karpowicz, J. Gagnon, M. Korbman, M. Hofstetter, S. Neppl, A. L. Cavalieri, Y. Komninos, T. Mercouris, C. A. Nicolaides, R. Pazourek, S. Nagele, J. Feist, J. Burgdorfer, A. M. Azzeer, R. Ernstorfer, R. Kienberger, U. Kleineberg, E. Goulielmakis, F. Krausz, and V. S. Yakovlev. Delay in Photoemission. *Science*, 328(5986):1658–1662, 2010.

[22] M. Uiberacker, T. Uphues, M. Schultze, A. J. Verhoef, V. Yakovlev, M. F. Kling, J. Rauschenberger, N. M. Kabachnik, H. Schroder, M. Lezius, K. L. Kompa, H. G. Muller, M. J. J. Vrakking, S. Hendel, U. Kleineberg, U. Heinzmann, M. Drescher, and F. Krausz. Attosecond real-time observation of electron tunnelling in atoms. *Nature*, 446(7136):627–632, 2007.

[23] E. Goulielmakis, M. Uiberacker, R. Kienberger, A. Baltuska, V. Yakovlev, A. Scrinzi, T. Westerwalbesloh, U. Kleineberg, U. Heinzmann, M. Drescher, and F. Krausz. Direct measurement of light waves. *Science*, 305(5688):1267–1269, 2004.

[24] E. Goulielmakis, Z. H. Loh, A. Wirth, R. Santra, N. Rohringer, V. S. Yakovlev, S. Zherebtsov, T. Pfeifer, A. M. Azzeer, M. F. Kling, S. R. Leone, and F. Krausz. Real-time observation of valence electron motion. *Nature*, 466(7307):739–744, 2010.

[25] Y. Mairesse and F. Quere. Frequency-resolved optical gating for complete reconstruction of attosecond bursts. *Physical Review A*, 71(1):011401, 2005.

[26] C. Lemell, B. Solleder, K. Tokesi, and J. Burgdorfer. Simulation of attosecond streaking of electrons emitted from a tungsten surface. *Physical Review A*, 79(6): 062901, 2009.

[27] G. H. Wannier. The threshold law for single ionization of atoms or ions by electrons. *Physical Review*, 90(5):817–825, 1953.

[28] A. Emmanouilidou and J. M. Rost. The coulomb four-body problem in a classical framework: triple photoionization of lithium. *Journal of Physics B-Atomic Molecular and Optical Physics*, 39(20):4037–4048, 2006.

[29] A. Emmanouilidou, P. J. Wang, and J. M. Rost. Initial state dependence in multielectron threshold ionization of atoms. *Physical Review Letters*, 100(6):063002, 2008.

[30] J. Colgan, A. Emmanouilidou, and M. S. Pindzola. Evidence for a T-Shape Break-Up Pattern in the Triple Photoionization of Li. *Physical Review Letters*, 110(6): 063001, 2013.

[31] A. Emmanouilidou and H. Price. Electron-electron collision dynamics of the four-electron escape in Be close to threshold. *Physical Review A*, 87(4):043428, 2013.

[32] H. Price and A. Emmanouilidou. Four-electron break-up geometries in beryllium. *Chaos, Solitons and Fractals*, 66:96–102, 2014.

[33] A. Emmanouilidou, A. Staudte, and P. B. Corkum. The two-electron attosecond streak camera for time-resolving intra-atomic collisions. *New Journal of Physics*, 12(10):103024, 2010.

[34] H. Price, A. Staudte, and A. Emmanouilidou. Energy sharing in the two-electron attosecond streak camera. *New Journal of Physics*, 13(9):093006, 2011.

[35] H. Price, A. Staudte, P. B. Corkum, and A. Emmanouilidou. Frequency-resolved optical gating for time-resolving knockout in double ionization with attosecond pulses. *Physical Review A*, 86(5):053411, 2012.

[36] A. Staudte, C. L. Cocke, A. H. Prior, A. Belkacem, C. Ray, H. W. Chong, T. E. Glover, R. W. Schoenlein, and U. Saalmann. Observation of a nearly isotropic, high-energy coulomb explosion group in the fragmentation of D_2 by short laser pulses. *Physical Review A*, 65(020703), 2002.

[37] H. Niikura, F. Legare, R. Hasbani, A. D. Bandrauk, M. Y. Ivanov, D. M. Villeneuve, and P. B. Corkum. Sub-laser-cycle electron pulses for probing molecular dynamics. *Nature*, 417(6892):917–922, 2002.

[38] B. Manschwetus, T. Nubbemeyer, K. Gorling, G. Steinmeyer, U. Eichmann, H. Rottke, and W. Sandner. Strong Laser Field Fragmentation of H_2: Coulomb Explosion without Double Ionization. *Physical Review Letters*, 102(11):011402, 2009.

[39] A. Emmanouilidou, C. Lazarou, A. Staudte, and U. Eichmann. Routes to formation of highly excited neutral atoms in the breakup of strongly driven H_2. *Physical Review A*, 85(1):011402, 2012.

[40] H. R. Sadeghpour, J. L. Bohn, M. J. Cavagnero, B. D. Esry, II Fabrikant, J. H. Macek, and A. R. P. Rau. Collisions near threshold in atomic and molecular physics. *Journal of Physics B-Atomic Molecular and Optical Physics*, 33(5):R93–R140, 2000.

[41] G. H. Wannier. Threshold law for multiple ionization. *Physical Review*, 100(4): 1180–1180, 1955.

[42] P. Grujic. The fourfold escape threshold law. *Physics Letters A*, 96(5):233–235, 1983.

[43] M. Y. Kuchiev and V. N. Ostrovsky. Threshold laws for the breakup of atomic particles into several charged fragments. *Physical Review A*, 58(1):321–335, 1998.

[44] R. Abrines and I. C. Percival. Classical theory of charge transfer and ionization of hydrogen atoms by protons. *Proceedings of the Physical Society of London*, 88 (562P):861–872, 1966.

[45] D. J. W. Hardie and R. E. Olson. Charge-transfer and ionization processes involving multiply charged ions in collision with atomic-hydrogen. *Journal of Physics B-Atomic Molecular and Optical Physics*, 16(11):1983–1996, 1983.

[46] A. Knapp, A. Kheifets, I. Bray, T. Weber, A. L. Landers, S. Schossler, T. Jahnke, J. Nickles, S. Kammer, O. Jagutzki, L. P. H. Schmidt, T. Osipov, J. Rosch, M. H. Prior, H. Schmidt-Bocking, C. L. Cocke, and R. Dorner. Mechanisms of photo double ionization of helium by 530 eV photons. *Physical Review Letters*, 89(3): 033004, 2002.

[47] T. Pattard and J. Burgdorfer. Half-collision model for multiple ionization by photon impact. *Physical Review A*, 64(4):042720, 2001.

[48] T. Schneider, P. L. Chocian, and J. M. Rost. Separation and identification of dominant mechanisms in double photoionization. *Physical Review Letters*, 89(7): 073002, 2002.

[49] T. Aberg. Asymptotic double-photoexcitation cross sections of helium atom. *Physical Review A*, 2(5):1726–1979, 1970.

[50] A. Emmanouilidou, T. Schneider, and J. M. Rost. Quasiclassical double photoionization from the 2 S-1,S-3 excited states of helium including shake-off. *Journal of Physics B-Atomic Molecular and Optical Physics*, 36(13):2717–2724, 2003.

[51] J. A. Tanis, J. Y. Chesnel, F. Fremont, D. Hennecart, X. Husson, A. Cassimi, J. P. Grandin, B. Skogvall, B. Sulik, J. H. Bremer, and N. Stolterfoht. Production of hollow lithium by multielectron correlation in 95 MeV/nucleon Ar^{18+}+Li collisions. *Physical Review Letters*, 83(6):1131–1134, 1999.

[52] J. A. R. Samson. Proportionality of electron-impact ionization to double photoionization. *Physical Review Letters*, 65(23):2861–2864, 1990.

[53] J. S. Cohen. Classical phase-space distributions for atomic-hydrogen collisions. *Journal of Physics B-Atomic Molecular and Optical Physics*, 18(9):1759–1769, 1985.

[54] T. Geyer and J. M. Rost. A quasi-classical approach to fully differential ionization cross sections. *Journal of Physics B-Atomic Molecular and Optical Physics*, 34(2): L47–L53, 2001.

[55] T. Geyer and J. M. Rost. A quasiclassical approach to electron impact ionization. *Journal of Physics B-Atomic Molecular and Optical Physics*, 35(6):1479–1499, 2002.

[56] T. Geyer and J. M. Rost. Dynamical stabilization of classical multi-electron targets against autoionization. *Journal of Physics B-Atomic Molecular and Optical Physics*, 36(4):L107–L112, 2003.

[57] S. A. Blanco, C. A. Falcon, C. O. Reinhold, J. I. Casaubon, and R. D. Piacentini. Electron-capture in low-energy and intermediate-energy collisions between completely stripped light-ions and metastable H(2s) targets. *Journal of Physics B-Atomic Molecular and Optical Physics*, 20(23):6295–6304, 1987.

[58] A. Emmanouilidou and J. M. Rost. Triple photoionization of lithium near threshold. *Journal of Physics B-Atomic Molecular and Optical Physics*, 39(5):L99–L103, 2006.

[59] R. Wehlitz, M. T. Huang, B. D. DePaola, J. C. Levin, I. A. Sellin, T. Nagata, J. W. Cooper, and Y. Azuma. Triple photoionization of lithium. *Physical Review Letters*, 81(9):1813–1816, 1998.

[60] H. Klar and W. Schlecht. Threshold multiple ionization of atoms - energy-dependence for double and triple escape. *Journal of Physics B-Atomic Molecular and Optical Physics*, 9(10):1699–1711, 1976.

[61] A. Emmanouilidou. Double-energy-differential cross sections for the Coulomb four-body problem in a quasiclassical framework. *Physical Review A*, 75(4):042702, 2007.

[62] J. Colgan and M. S. Pindzola. Energy differential cross sections for the triple photoionization of lithium. *Journal of Physics B-Atomic Molecular and Optical Physics*, 39(8):1879–1887, 2006.

[63] T. Schneider and J-M. Rost. Double photoionization of two-electron atoms based on the explicit separation of the dominant ionization mechanisms. *Pyhsical Review A*, 67(6):062704, 2003.

[64] B. L. Henke, E. M. Gullikson, and J. C. Davis. X-ray interactions - photoabsorption, scattering, transmission, and reflection at E=50-30,000 eV, Z=1-92. *Atomic Data and Nuclear Data Tables*, 54(2):181–342, 1993.

[65] A. Emmanouilidou. Total quadruple photoionization cross section of beryllium. *Physical Review A*, 76(5):054701, 2007.

[66] P. K. Kabir and E. E. Salpeter. Radiative corrections to the ground-state energy of the helium atom. *Physical Review*, 108(5):1256–1263, 1957.

[67] C. O. Reinhold and C. A. Falcon. Classical ionization and charge-transfer cross-sections for H^+ + He and H^+ + Li^+ collisions with consideration of model interactions. *Physical Review A*, 33(6):3859–3866, 1986.

[68] E. Wigner. On the quantum correction for thermodynamic equilibrium. *Physical Review*, 40(5):749–759, 1932.

[69] P. Kustaanh and E. Stiefel. Perturbation theory of kepler motion based on spinor regularization. *Journal Fur Die Reine Und Angewandte Mathematik*, 218:204–218, 1965.

[70] S. J. Aarseth and K. Zare. A regularization of the three-body problem. *Celestial Mechanics*, 10(2):185–285, 1974.

[71] W. H. Press, S. A. Teukolsky, W. T. Vetterling, and B. P. Flannery. *Numerical Recipes*. Cambridge University Press, 2007.

[72] A. Emmanouilidou and J. M. Rost. Attosecond-time-scale multielectron collisions in the coulomb four-body problem: Traces in classical probability densities. *Physical Review A*, 75(2):022712, 2007.

[73] G. Sansone, T. Pfeifer, K. Simeonidis, and A. I. Kuleff. Electron Correlation in Real Time. *Chemphyschem*, 13(3):661–680, 2012.

[74] F. T. Smith. Generalized angular momentum in many-body collisions. *Physical Review*, 120(3):1058–1069, 1960.

[75] J. M. Rost. Semiclassical s-matrix theory for atomic fragmentation. *Physics Reports-Review Section of Physics Letters*, 297(6):271–344, 1998.

[76] J. M. Rost. Critical phenomena in atomic physics. *Physica E*, 9(3):467–473, 2001.

[77] P. Eckle, A. N. Pfeiffer, C. Cirelli, A. Staudte, R. Dorner, H. G. Muller, M. Buttiker, and U. Keller. Attosecond Ionization and Tunneling Delay Time Measurements in Helium. *Science*, 322(5907):1525–1529, 2008.

[78] R. C. Forrey, H. R. Sadeghpour, J. D. Baker, J. D. Morgan, and A. Dalgarno. Double photoionization of excited S-1 and S-3 states of the helium isoelectronic sequence. *Physical Review A*, 51(3):2112–2116, 1995.

[79] C. Siedschlag and T. Pattard. Single-photon double ionization of the hydrogen molecule. *Journal of Physics B-Atomic Molecular and Optical Physics*, 38(13): 2297–2310, 2005.

[80] J. S. Briggs and V. Schmidt. Differential cross sections for photo-double-ionisation of the helium atom. *Journal of Physics B-Atomic Molecular and Optical Physics*, 33(1):R1–R48, 2000.

[81] J. G. Leopold and I. C. Percival. Ionization of highly excited atoms by electric-fields iii microwave ionization and excitation. *Journal of Physics B-Atomic Molecular and Optical Physics*, 12(5):709–721, 1979.

[82] F. Träger. *Springer handbook of lasers and optics.* Springer, New York, 2007.

[83] R. Trebino, K. W. DeLong, D. N. Fittinghoff, J. N. Sweetser, M. A. Krumbugel, B. A. Richman, and D. J. Kane. Measuring ultrashort laser pulses in the time-frequency domain using frequency-resolved optical gating. *Review of Scientific Instruments*, 68(9):3277–3295, 1997.

[84] B.H. Bransden and C.J. Joachain. *Physics of Atoms and Molecules.* Pearson Education Limited, 2003.

[85] H.A. Bethe and E.E. Salpeter. *Quantum Mechanics of One- and Two-Electron Atoms.* Dover Publications Inc., 1957.

[86] T. Nubbemeyer, K. Gorling, A. Saenz, U. Eichmann, and W. Sandner. Strong-Field Tunneling without Ionization. *Physical Review Letters*, 101(23):233001, 2008.

[87] J. Liu, D. F. Ye, J. Chen, and X. Liu. Complex dynamics of correlated electrons in molecular double ionization by an ultrashort intense laser pulse. *Physical Review Letters*, 99(1):013003, 2007.

[88] D. F. Ye, J. Chen, and J. Liu. Classical trajectory perspective on double-ionization dynamics of diatomic molecules irradiated by ultrashort intense laser pulses. *Physical Review A*, 77(1):013403, 2008.

[89] A. Emmanouilidou and A. Staudte. Intensity dependence of strong-field double-ionization mechanisms: From field-assisted recollision ionization to recollision-assisted field ionization. *Physical Review A*, 80(5):053415, 2009.

[90] A. Emmanouilidou. Recoil collisions as a portal to field-assisted ionization at near-uv frequencies in the strong-field double ionization of helium. *Physical Review A*, 78(2):023411, 2008.

[91] J. Chen, J. Liu, L. B. Fu, and W. M. Zheng. Interpretation of momentum distribution of recoil ions from laser-induced nonsequential double ionization by semiclassical rescattering model. *Physical Review A*, 63(1):011404, 2001.

[92] T. Brabec, M. Y. Ivanov, and P. B. Corkum. Coulomb focusing in intense field atomic processes. *Physical Review A*, 54(4):R2551–R2554, 1996.

[93] A. Frank, A. L. Rivera, and K. B. Wolf. Wigner function of Morse potential eigenstates. *Physical Review A*, 61(5):054102, 2000.

[94] R. Murray, M. Spanner, S. Patchkovskii, and M. Y. Ivanov. Tunnel Ionization of Molecules and Orbital Imaging. *Physical Review Letters*, 106(17):173001, 2011.

[95] D. C. Heggie. A Global regularisation of the gravitational N-body problem. *Celestial Mechanics*, 10:217–241, 1974.

[96] S. Mikkola and S. Aarseth. A time-transformed leapfrog scheme - Integration of few-body systems with large mass ratios. *Celestial Mechanics and Dynamical Astronomy*, 84(4):343–354, 2002.

[97] S. Mikkola and K. Tanikawa. Algorithmic regularization of the few-body problem. *Monthly Notices of the Royal Astronomical Society*, 310(3):745–749, 1999.

[98] W. H. Press, S. A. Teukolsky, W. T. Vetterling, and B. P. Flannery. *Numerical Recipes*. Cambridge University Press, 2007.

[99] N. B. Delone and V. P. Krainov. Energy and angular electron-spectra for the tunnel ionization of atoms by strong low-frequency radiation. *Journal of the Optical Society of America B-Optical Physics*, 8(6):1207–1211, 1991.

[100] Y. Li, J. Chen, S. P. Yang, and J. Liu. Alignment effect in nonsequential double ionization of diatomic molecules in strong laser fields. *Physical Review A*, 76(2): 023401, 2007.

[101] L. Meng, C. O. Reinhold, and R. E. Olson. Electron removal from molecular-hydrogen by fully stripped ions at intermediate energies. *Physical Review A*, 40 (7):3637–3645, 1989.

[102] A. Saenz. Enhanced ionization of molecular hydrogen in very strong fields. *Physical Review A*, 61(5):051402, 2000.

[103] H. Goldstein. *Classical Mechanics*. Addison-Wesley, 1980.

[104] S. Patchkovskii, Z. X. Zhao, T. Brabec, and D. M. Villeneuve. High harmonic generation and molecular orbital tomography in multielectron systems. *Journal of Chemical Physics*, 126(11):114306, 2007.

[105] I. N. Levine. *Quantum Chemistry*. Prentice Hall, New Jersey, 2000.

[106] H. J. Werner, P. J. Knowles, G. Knizia, F. R. Manby, M. Schütz, and et al. *Molpro, version 2012.1, a package of ab initio programs (2012).* Prentice Hall, New Jersey, http://www.molpro.net.

[107] J. S. Cohen. Reexamination of over-the-barrier and tunneling ionization of the hydrogen atom in an intense field. *Physical Review A*, 64(4):043412, 2001.

[108] E. Merzbacher. *Quantum Mechanics.* Wiley, NewYork, 1998.

[109] R. Bulirsch and J. Stoer. Numerical treatment of ordinary differential equations by extrapolation methods. *Numerische Mathematik*, 8(1):1–13, 1966.

[110] S. Mikkola and K. Tanikawa. Implementation of an efficient logarithmic-Hamiltonian three-body code. *New Astronomy*, 20:38–41, 2013.

[111] R. L. Becker and A. D. Mackellar. Theoretical initial-l dependence of ion-rydberg-atom collision cross-sections. *Journal of Physics B-Atomic Molecular and Optical Physics*, 17(19):3923–3942, 1984.

[112] H. Sakai, J. J. Larsen, I. Wendt-Larsen, J. Olesen, P. B. Corkum, and H. Stapelfeldt. Nonsequential double ionization of D_2 molecules with intense 20-fs pulses. *Physical Review A*, 67(6):063404, 2003.

[113] P. Dietrich, N. H. Burnett, M. Ivanov, and P. B. Corkum. High-harmonic generation and correlated 2-electron multiphoton ionization with elliptically polarized-light. *Physical Review A*, 50(5):R3585–R3588, 1994.

[114] T. Zuo and A. D. Bandrauk. Charge-resonance-enhanced ionization of diatomic molecular-ions by intense lasers. *Physical Review A*, 52(4):R2511–R2514, 1995.

[115] R. Kopold, W. Becker, H. Rottke, and W. Sandner. Routes to nonsequential double ionization. *Physical Review Letters*, 85(18):3781–3784, 2000.

[116] B. Feuerstein, R. Moshammer, D. Fischer, A. Dorn, C. D. Schroter, J. Deipenwisch, J. R. C. Lopez-Urrutia, C. Hohr, P. Neumayer, J. Ullrich, H. Rottke, C. Trump, M. Wittmann, G. Korn, and W. Sandner. Separation of recollision mechanisms in nonsequential strong field double ionization of ar: The role of excitation tunneling. *Physical Review Letters*, 87(4):043003, 2001.

[117] M. Bashkansky, P. H. Bucksbaum, and D. W. Schumacher. Asymmetries in above-threshold ionization. *Physical Review Letters*, 60(24):2458–2461, 1988.

[118] S. P. Goreslavski, G. G. Paulus, S. V. Popruzhenko, and N. I. Shvetsov-Shilovski. Coulomb asymmetry in above-threshold ionization. *Physical Review Letters*, 93 (23):233002, 2004.

[119] K. Doblhoff-Dier, K. I. Dimitriou, A. Staudte, and S. Grafe. Classical analysis of coulomb effects in strong-field ionization of H_2^+ by intense circularly polarized laser fields. *Physical Review A*, 88(3):033411, 2013.

[120] M. Spanner, S. Grafe, S. Chelkowski, D. Pavicic, M. Meckel, D. Zeidler, A. B. Bardon, B. Ulrich, A. D. Bandrauk, D. M. Villeneuve, R. Dorner, P. B. Corkum, and A. Staudte. Coulomb asymmetry and sub-cycle electron dynamics in multiphoton multiple ionization of H_2. *Journal of Physics B-Atomic Molecular and Optical Physics*, 45(19):194011, 2012.

[121] X. G. Ren, A. Dorn, and J. Ullrich. Coulomb four-body problem: Electron-impact double ionization of helium in the threshold regime. *Physical Review Letters*, 101 (9):093201, 2008.

[122] J. Colgan, M. S. Pindzola, and F. Robicheaux. Lattice calculations of the photoionization of Li. *Physical Review Letters*, 93(5):053201, 2004.

[123] J. Colgan and M. S. Pindzola. Angular Distributions for the Complete Photofragmentation of the Li Atom. *Physical Review Letters*, 108(5):053001, 2012.

[124] E. J. Heller. Wigner phase space method - analysis for semiclassical applications. *Journal of Chemical Physics*, 65(4):1289–1298, 1976.

[125] D. Eichenauer, N. Grun, and W. Scheid. Classical trajectory calculations for H^+ -H collisions with the wigner function as initial phase-space distribution. *Journal of Physics B-Atomic Molecular and Optical Physics*, 14(20):3929–3941, 1981.

[126] S. F. Boys. Electronic wave functions .1. a general method of calculation for the stationary states of any molecular system. *Proceedings of the Royal Society of London Series a-Mathematical and Physical Sciences*, 200(1063):542–554, 1950.

[127] J. P. Dahl and M. Springborg. Wigner phase-space function and atomic-structure .1. the hydrogen-atom ground-state. *Molecular Physics*, 47(5):1001–1019, 1982.

[128] J. C. Slater. Atomic shielding constants. *Physical Review*, 36(1):57–64, 1930.

[129] S. Huzinaga. Gaussian-type functions for polyatomic systems .i. *Journal of Chemical Physics*, 42(4):1293–1302, 1965.

[130] M. Abramowitz and I. A. Stegun. *Handbook of Mathematical Functions with Formulas, Graphs and Mathematical Tables*. Dover, New York, 1972.

[131] H. Friedrich. *Theoretical Atomic Physics*. Springer, 2005.